ÉCOLE DE TECHNOLOGIE SUPÉRIEURE
UNIVERSITÉ DU QUÉBEC

ARTICLE-BASED THESIS
PRESENTED TO
ÉCOLE DE TECHNOLOGIE SUPÉRIEURE
NATIONAL UNIVERSITY OF SCIENCE AND TECHNOLOGY "MISIS"
(COTUTORSHIP)

IN PARTIAL FULFILLMENT OF THE REQUIREMENTS
FOR THE DEGREE OF DOCTOR OF PHILOSOPHY
Ph. D.

COTUTORSHIP RUSSIA-QUÉBEC

BY
Sergey DUBINSKIY

Ti-Nb-(Zr,Ta) SUPERELASTIC ALLOYS FOR MEDICAL IMPLANTS: THERMOMECHANICAL PROCESSING, STRUCTURE, PHASE TRANSFORMATIONS AND FUNCTIONAL PROPERTIES

MONTREAL, 10 DECEMBER 2013

BOARD OF EXAMINERS

THIS THESIS HAS BEEN EVALUATED

BY THE FOLLOWING BOARD OF EXAMINERS

Mr. VLADIMIR BRAILOVSKI, Professor, Thesis Supervisor
Département de Génie Mécanique at École de Technologie Supérieure

Mr. SERGEY D. PROKOSHKIN, Professor, Thesis Co-supervisor
Department of Plastic Deformation of Special Alloys at National University of Science and Technology "MISiS" (Moscow, Russia)

Mrs. NICOLA HAGEMEISTER, Professor, President of the Board of Examiners
Département de Génie de la Production Automatisée at École de Technologie Supérieure

Mr. PATRICK TERRIAULT, Professor, Member of the jury
Département de Génie Mécanique at École de Technologie Supérieure

Mr. MAMOUN MEDRAJ, Professor, Member of the jury (external)
Mechanical and Industrial Engineering Department at Concordia University

THIS THESIS WAS PRESENTED AND DEFENDED

IN THE PRESENCE OF A BOARD OF EXAMINERS AND PUBLIC

15 NOVEMBER 2013

AT ÉCOLE DE TECHNOLOGIE SUPÉRIEURE

ACKNOWLEDGEMENT

First and foremost I would like to express my gratitude to Professors Vladimir Brailovski and Sergey Prokoshkin for giving me the unique opportunity to work on this project, for general and practical supervision and, especially, for inspiring me in tough times. I am thankful to them for their excellent example of teamwork, in which I am lucky to be involved.

I would like to thank Drs. Karine Inaekyan and Andrey Korotitskiy for invaluable practical help and encouragement at all times.

I would also like to thank Michel Drouin, Serge Plamondon, Jean-Guy Gagnon, Radu Romanica and Patrick Sheridan for technical support and useful advice.

I am grateful to all my colleagues: Vadim, Jonathan, Yulia, Charles F., Thoma, Charles S., Simon, Alena, Daniel and Yan B. for the pleasure of working together. I am very appreciative of the patience with which Yann F., Pierre-Luc and Yannick were answering my hundreds of questions.

Last, but not least, I would like to express my gratitude to all my family for their great patience and support during all these years.

Ti-Nb-(Zr,Ta) SUPERELASTIC ALLOYS FOR MEDICAL IMPLANTS: THERMOMECHANICAL PROCESSING, STRUCTURE, PHASE TRANSFORMATIONS AND FUNCTIONAL PROPERTIES

Sergey DUBINSKIY

RÉSUMÉ

Le but de ce projet est de développer une nouvelle classe de matériaux d'implants orthopédiques, qui combinerait une excellente biocompatibilité du titane pur avec une compatibilité biomécanique exceptionnelle d'alliages à mémoire de forme Ti-Ni. Les candidats les plus appropriés pour un tel rôle sont les alliages à mémoire de forme Ti-Nb-Zr et Ti-Nb-Ta de type beta métastable. Cette classe de matériaux a été développée tout récemment et l'influence du traitement thermomécanique sur leur structure et leurs propriétés fonctionnelles ne faisaient pas encore objet d'aucune étude approfondie. Par conséquent, ce projet est axé sur les relations entre la composition, la microstructure et les propriétés fonctionnelles des alliages superélastiques Ti-Nb-Zr et Ti-Nb-Ta pour applications biomédicales. L'objectif principal est d'améliorer les propriétés fonctionnelles de ces alliages, plus particulièrement les propriétés superélastiques et la résistance à la fatigue, grâce à l'optimisation de la composition des alliages et de leur traitement thermomécanique.

Premièrement, cette thèse prouve que la structure et les propriétés fonctionnelles des alliages à mémoire de forme à base de Ti-Nb peuvent être efficacement contrôlées par un traitement thermomécanique, y compris par la déformation à froid suivie de traitement thermique de recuit et de vieillissement. Il est également démontré que la formation d'une structure nano-sous-granulaire mène à une amélioration significative de la superélasticité et de la résistance à la fatigue de ces alliages. L'influence du vieillissement sur la cinétique de précipitation de la phase ω et, par conséquent, sur les propriétés fonctionnelles des alliages Ti-Nb-Zr et Ti-Nb-Ta est également observée.

Basant sur les résultats obtenus, les régimes du traitement thermomécanique optimisé résultant en une meilleure combinaison des propriétés fonctionnelles sont recommandés pour chaque alliage, d'un point de vue de matériau pour implants orthopédiques.

Deuxièmement, un dispositif de traction miniature pour une étude *in situ* à basse température dans la chambre d'un diffractomètre à rayons X a été développé et utilisé. Une étude comparative sur les caractéristiques des transformations et de l'évolution du réseau cristallin dans des conditions du contrôle de déformation et de balayage en température entre -150 et +100^{o}C a été réalisée *in situ*. Les paramètres de la maille cristalline des phases β et α" ont été calculés dans une plage de température étudiée, ce que nous a permis de conclure que plus la température est élevée, plus la déformation qui accompagne la transformation des phases α"→β est faible. On a également constaté que le chargement à basse température mène à la formation additionnelle et la réorientation de la phase α", tandis que l'application de la charge lors du chauffage modifie la séquence des transformations. L'élargissement et le

rétrécissement réversible des pics de la phase β qui sont observées lors du balayage en température sont le résultat direct de l'apparition et de la disparition des micro-contraintes causées par la transformation martensitique thermoélastique réversible.

Mots-clés: alliages à mémoire de forme, alliages de titane, biomatériaux, traitement thermomécanique, laminage, traitement thermique, propriétés mécaniques, structure, nanostructures, microscopie électronique, diffraction rayons X, dispositif de traction *in situ*.

Ti-Nb-(Zr,Ta) SUPERELASTIC ALLOYS FOR MEDICAL IMPLANTS: THERMOMECHANICAL PROCESSING, STRUCTURE, PHASE TRANSFORMATIONS AND FUNCTIONAL PROPERTIES

Sergey DUBINSKIY

ABSTRACT

The aim of this project is to develop a new class of orthopaedic implant materials that combine the excellent biocompatibility of pure titanium with the outstanding biomechanical compatibility of Ti-Ni-based shape memory alloys. The most suitable candidates for such a role are Ti-Nb-Zr and Ti-Nb-Ta near-beta shape memory alloys. Since this class of materials was developed quite recently, the influence of thermomechanical treatment on their structure and functional properties has not as yet been the subject of any comprehensive study. Consequently, this project is focused on the interrelations between the composition, the microstructure and the functional properties of superelastic Ti-Nb-Zr and Ti-Nb-Ta alloys for biomedical application. The principal objective is to improve the functional properties of these alloys, more specifically their superelastic properties and fatigue resistance, through optimization of the alloys' composition and thermomechanical processing.

It is shown in this thesis that the structure and functional properties of Ti-Nb-based shape memory alloys can be effectively controlled by thermomechanical processing including cold deformation with post-deformation annealing and ageing. It is also shown that the formation of nanosubgrain substructure leads to a significant improvement of superelasticity and fatigue resistance in these alloys. The influence of ageing on the ω-phase precipitation kinetics and, consequently, on the functional properties of Ti-Nb-Zr and Ti-Nb-Ta alloys is also observed.

Based on the results obtained, optimized regimes of thermomechanical treatment resulting in a best combination of functional properties are recommended for each alloy, from the orthopaedic implant materials standpoint.

An original tensile stage for a low-temperature chamber of an X-ray diffractometer is developed and used in this project. A unique low-temperature (-150...+100^{o}C) comparative *in situ* X-ray study of the transformations' features and crystal lattice evolution is performed under strain-controlled conditions. The lattice parameters of β- and α"-phases calculated across the whole testing temperature range allow us to conclude that the higher the temperature, the lower the α"→β transformation strain. It is found also that loading at low temperatures results in α"-phase formation and reorientation, while application of the load during heating changes the transformation sequences. The observed reversible β-phase X-ray line widening and narrowing during temperature scanning are the direct result of appearance and disappearance of microstresses caused by reversible thermoelastic martensitic transformation.

Keywords: shape memory alloys, titanium alloys, biomaterials, thermomechanical treatment, rolling, heat treating, mechanical properties, structure, nanostructures, electron microscopy, X-ray diffraction analysis, *in situ* tensile stage.

TABLE OF CONTENTS

Page

INTRODUCTION 1

CHAPTER 1 GENERAL INTRODUCTION 3
1.1 Requirements of metallic implant materials 3
1.1.1 Biocompatibility 3
1.1.2 Mechanical behaviour 4
1.1.3 Other requirements 5
1.2 Types of metallic implant materials 6
1.2.1 Stainless steel 7
1.2.2 Co and Co-Cr-based alloys 7
1.2.3 Commercially pure Ta 8
1.2.4 Commercially pure Zr 8
1.2.5 Ti and Ti alloys 8
1.2.5.1 α and near-α titanium alloys 10
1.2.5.2 α+β titanium alloys 11
1.2.5.3 β titanium alloys 12
1.3 Ti-based shape memory alloys 13
1.3.1 Phase transformation in Ti-based SMA 16
1.3.1.1 Phase transformation in Ti-Ni-based SMA 16
1.3.1.2 Phase transformation in Ti-Nb-based SMA 17
1.3.1.3 Effect of the Ni and Nb contents on the functional properties of Ti-based SMA 18
1.3.2 Processing of the Ti-based SMA 22
1.3.2.1 Heat treatment 22
1.3.2.2 Thermomechanical treatment 26
1.4 Research objectives 32
1.5 Methodology 32
1.5.1 Materials 33
1.5.2 Thermomechanical treatment 33
1.5.3 Characterization 34
1.6 Thesis organization 35

CHAPTER 2 ARTICLE #1: STRUCTURE FORMATION DURING THERMOMECHANICAL PROCESSING OF Ti-Nb-(Zr, Ta) ALLOYS AND THE MANIFESTATION OF THE SHAPE-MEMORY EFFECT 39
2.1 Summary 39
2.2 Abstract 40
2.3 Introduction 41
2.4 Experimental 43
2.5 Results and discussion 46

2.6 Conclusions....63
2.7 Acknowledgments....64
2.8 References....64

CHAPTER 3 ARTICLE #2: STRUCTURE AND PROPERTIES OF Ti-19.7Nb-5.8Ta SHAPE MEMORY ALLOY SUBJECTED TO THERMOMECHANICAL PROCESSING INCLUDING AGING....71
3.1 Summary....71
3.2 Abstract....72
3.3 Introduction....73
3.4 Experimental procedure....73
3.5 Results....76
3.6 Discussion....88
3.7 Conclusions....91
3.8 Acknowledgments....92
3.9 References....92

CHAPTER 4 ARTICLE #3: *IN SITU* X-RAY DIFFRACTION STRAIN-CONTROLLED STUDY OF Ti-Nb-Zr AND Ti-Nb-Ta SHAPE MEMORY ALLOYS: CRYSTAL LATTICE AND TRANSFORMATION FEATURES....95
4.1 Summary....95
4.2 Abstract....96
4.3 Introduction....97
4.4 Experimental....99
4.5 Results....106
4.5.1 Structure transformations and crystal lattice changes....106
4.5.2 Phase transformation features....116
4.5.3 Reversible inhomogeneous distortions....118
4.6 Discussion....120
4.6.1 Structure transformations and crystal lattice changes....120
4.6.2 Phase transformation features....121
4.6.3 Reversible inhomogeneous distortions....124
4.7 Conclusions....125
4.8 Acknowledgements....126
4.9 References....126

CONCLUSIONS....133

RECOMMENDATIONS....135

ANNEX I ARTICLE: *IN-SITU* X-RAY STUDY OF PHASE TRANSFORMATIONS IN Ti-Nb-BASED SMA UNDER VARIABLE STRESS-TEMPERATURE CONDITIONS: PRELIMINARY RESULTS....137

LIST OF BIBLIOGRAPHICAL REFERENCES....149

LIST OF TABLES

Page

Table 1.1 Mechanical properties of bones [3],[5]-[12] 5

Table 1.2 Mechanical properties of metallic implant materials compared with bones 6

Table 1.3 Orthopaedic alloys and their mechanical properties [16] 10

Table 1.4 Lattice strains (η_1, η_2 and η_3) of Ti-27Nb, Ti-22Nb-6Zr and Ti-22Nb-6Ta (at.%) alloys [34] 21

Table 2.1 Chemical composition of the Ti-Nb-Ta and Ti-Nb-Zr alloys (at %)* 43

Table 2.2 Regimes of thermomechanical treatment of the Ti-Nb-Ta and Ti-Nb-Zr alloys 44

Table 3.1 Ti-Nb-Ta ingot composition 74

Table 3.2 Phase constituents and other microstructural features resulted from TMTs 80

Table 4.1 Chemical compositions of studied alloys 99

LIST OF FIGURES

Page

Figure 1.1 The relationship between the polarization resistance and biocompatibility of pure metals, Co-Cr, and stainless steels [4] 4

Figure 1.2 Comparison of mechanical properties of metallic implant materials and bone (from [1],[3],[5],[14]-[16]).....7

Figure 1.3 Pseudo-binary phase diagram of Ti-β stabilizer [16]: β_c – the minimal content of β-stabilizer for β alloy, β_s – the minimal content of β-stabilizer for stable β alloy 9

Figure 1.4 Comparison of (a) Young's modulus and (b) elongation of pure titanium and Ti-based alloys with those of bone (from [1],[3],[5],[15], [16]).....13

Figure 1.5 Typical transformation versus temperature curve for a shape memory alloy specimen under constant load (stress) as it is cooled and heated [1].....14

Figure 1.6 Comparison of the stress-strain diagrams of austenitic 316L stainless steel [5], Co-Cr-based alloy [5], pure α-Ti (grade 4) [15], Ti-Ni-based SMA [20] and trabecular bone [21].....15

Figure 1.7 Phase diagram of a Ti–Ni alloy, to which the phase equilibrium between the B2 and Ti_3Ni_4 phases is added [23].....16

Figure 1.8 Calculated Ti-Nb equilibrium phase diagram [35].....18

Figure 1.9 M_s temperature as a function of Ni content for binary Ti-Ni alloys [23] ..19

Figure 1.10 Effect of Nb content on the transformation strain (a) and martensitic transformation start temperature (b) [38].....20

Figure 1.11 Effect of Ta, Zr and O addition on Ms temperature of Ti-22at.%Nb alloy (modified [34]).....20

Figure 1.12 Influence of Ta content on (a) critical stress for slip (σ_s) and apparent yield stress and (b) maximum recovery strain of Ti-22at.%Nb alloy (modified [34]).....21

Figure 1.13 Variations of the Young's modulus and ultimate tensile strength of Ti-24Nb-4Zr-7.9Sn (wt.%) alloy as a function of time of ageing at 500^{o}C [56].....24

Figure 1.14 Stress-strain curves obtained at RT by cyclic loading-unloading tensile tests for the Ti-26at.%Nb alloy specimen annealed at 873 K for 0.6 ks (intermediate-temperature annealing, ITA) and the specimen aged at 573 K for 3.6 ks after annealing treatment (intermediate-temperature annealing + ageing, ITA+AG) [38] 25

Figure 1.15 Transmission electron microscopy of Ti-50.0at.% Ni alloy subjected to (a) cold-rolling (e=0.30) and cold rolling with post-deformation annealing at (b) 200°C, (c) 300°C, (d) 350°C and (e) 400°C [73] 28

Figure 1.16 Transmission electron microscopy of Ti-50.0at.% Ni alloy subjected to (a) cold-rolling (e=1.9) and cold rolling with post-deformation annealing at (b) 250°C, (c) 300°C and (d) 400°C [73].....29

Figure 1.17 Transformation temperatures as functions of the PDA temperature for three levels of cold work (a) e=0.30; (b) e=0.88 and (c) e=1.9 [73].....30

Figure 1.18 Maxima of recovery stress σ_r (●) and completely recoverable strain $\varepsilon_{r,1}$ (0.2% offset) (×) measured as functions of the PDA temperature after different cold works: (a) e=0.30; (b) e=0.88 and (c) e=1.9 [73] 30

Figure 1.19 Young's modulus and strength (a) and plastic elongation and reduction in area (b) of cold- (solid symbols) and warm- (open symbols) rolled sheets of Ti-24Nb-4Zr-7.9Sn (wt.%) alloy [31] 31

Figure 2.1 Structure of the Ti-18.3Nb-5.1Zr (TNZ1) alloy after (a) deformation to e = 0.75 and postdeformation annealing for 1 h at (b, c) 450, (d, e) 600, (f, g) 750, and (h, i) 900°C. Light microscopy 47

Figure 2.2 Structure of the Ti-19.5Nb-6.5Ta (TNT1) alloy after deformation to e = 0.3 and postdeformation annealing for 1 h at (a) 700°C (1 h) and (b) 900°C (30 min). Light microscopy 48

Figure 2.3 Dependence of the X-ray diffraction line width B_{hkl} of the β phase on the degree of initial deformation in the Ti-18.3Nb-5.1Zr (TNZ1) alloy ...49

Figure 2.4 Variation of the width of the X-ray diffraction lines of the β phase of the Ti-18.3Nb-5.lZr (TNZ1) alloy after deformation to (a) e = 0.28, (b) 0.75, and (c) 2; and (d) the Ti-19.5Nb-6.5Ta (TNT1) alloy after deformation to e = 0.26 and postdeformation annealing. Horizontal lines indicate the levels of B_{hkl} for the quenched state (e = 0) (×) 211β, (+) 200β, and (●) 110β 50

Figure 2.5 The lattice parameter of the β phase in the Ti-21.2Nb-5.6Zr (TNZ2) alloy after different treatments: (×) e = 0 (quenching at 900°C); (●) e = 0.28; (+) e = 0.75; and (○) e = 2) 51

Figure 2.6 Lattice parameters of the α" martensite and the maximum strain of the lattice upon the martensitic transformation of the Ti-19.5Nb-6.5Ta (TNT1) alloy after rolling to *e* = 0.28, annealing at different temperatures, and deformation to failure at room temperature.....53

Figure 2.7 Structure of the Ti-21.2Nb-5.6Zr (TNZ2) alloy subjected to moderate cold deformation (e = 0.28) and postdeformation annealing (1 h) at the temperatures (a) 450, (b) 500, (c) 550, and (d) 600°C. Diffraction electron microscopy: (BF) bright-field images, (DF) dark-field images, and diffraction patterns 55

Figure 2.8 The structure of the Ti-21.2Nb-5.6Zr (TNZ2) alloy subjected to severe cold plastic deformation (e = 2) and postdeformation annealing at the temperatures (a) 450, (b) 500, (c) 550, and (d) 600°C. Diffraction electron microscopy: (BF) bright-field images, (DF) dark-field images of the β phase, and diffraction patterns.....56

Figure 2.9 Hardness dependence on the PDA temperature of the alloys: (a) Ti-18.3Nb-5.1Zr (TNZ1); and (b) Ti-20.9Nb-5.7Zr (TNZ3) 59

Figure 2.10 Loading-unloading deformation diagrams of the Ti-20.9Nb-5.7Zr (TNZ3) alloy annealed in the range from 450 to 900°C after moderate plastic deformation (e = 0.37). The inset shows the deformation diagrams of loading-unloading tests at various temperatures after *e* = 0.37 and PDA at 600°C.....60

Figure 2.11 Deformation diagrams of loading-unloading of the Ti-19.5Nb-6.5Ta (TNT1) alloy annealed in the range from 450 to 900°C after moderate plastic deformation (e = 0.26).....61

Figure 2.12 Variation of the microhardness and Young's modulus of the Ti-20.9Nb-5.7Zr (TNZ3) alloy depending on the PDA temperature. The initial strain *e* is 0.37.....62

Figure 3.1 X-ray diffractograms of Ti-Nb-Ta alloy subjected to CR e=0.37 (a), e=0.37+PDA (T=500°C, 1h) (b), and e=0.37+PDA (T=750°C, 1h) (c); ↑ - expected locations of ω-phase X-ray lines 77

Figure 3.2 Structure of Ti-Nb-Ta alloy subjected to CR (e=0.37)+PDA (T=500 (a) and 600°C (b); 1h); a – bright field image, b – dark field image in a β-phase matrix reflection and SAED pattern (<110>$_\beta$ zone axis with two high-angle misorientations) 78

Figure 3.3 Dark-field image in ω-phase reflections of Ti-Nb-Ta alloy after CR (e=0.37)+PDA (T=500°C,1h)+AG(T=300°C, 1h (a) and 3h (c)), and

corresponding SAED pattern, <110>$_\beta$ zone axis (b, d). Doubled arrow indicates an elongated row of ω particles 79

Figure 3.4 Microhardness Vickers measurements and stress-strain diagrams of Ti-Nb-Ta alloy subjected to CR (e=0.37)+PDA (1h) at different temperatures 81

Figure 3.5 Microhardness Vickers measurements and stress-strain diagrams of Ti-Nb-Ta alloy subjected to CR (e=0.37) + PDA (T=500°C, 1h) + AG at 300°C with different aging times (t) 82

Figure 3.6 Transformation yield stress (σ_{tr}) and Young's modulus of Ti-Nb-Ta alloy subjected to (a) e=0.37+PDA (1h) at different temperatures, and (b) e=0.37+PDA (T=500°C, 1h) + AG (300°C, 10 min…3h). Insert: schematic presentation of the transformation yield stress and Young's modulus measurements 82

Figure 3.7 Stress-strain cycling diagrams of Ti-Nb-Ta alloys after e=0.37+PDA: (a) as-deformed, e=0.37; deformed and annealed at 400 (b); 450 (c); 500 (d); 550 (e); 600 (f) and 700°C (g) (all 1h). Aged at 300°C after e=0.37+500°C (1h): 10 min (h); 30 min (i); 1h (j) and 3h (k) 84

Figure 3.8 Cycling stress-strain diagrams of Ti-Nb-Ta alloys after e=0.37+600°C at (a) 25°C and (b) 40°C 85

Figure 3.9 Constant-strain temperature scanning diagrams for 2.5% strain for Ti-Nb-Ta subjected to e=0.37+PDA (T=450, 500, 600 and 700°C) (a) and e=0.37+500°C (1h) + aging at 300°C (1 and 3 h) (b) 86

Figure 3.10 Variation of the reverse martensitic transformation temperatures and characteristic stresses for Ti-Nb-Ta subjected to e=0.37+PDA (a) and e=0.37+500°C (1h) + aging at 300°C (1 and 3 h) (b) 87

Figure 3.11 Recovery strain dependence on induced strain in bending SM testing at -196°C and subsequent heating above A_f of Ti-Nb-Ta alloy subjected to CR+PDA (1h) (a) and CR+PDA+AG (300°C, 1h and 3h) (b). To facilitate observation, not all the experimental points are presented 88

Figure 3.12 Maximum completely recoverable strain of shape memory effect (ε_r^{max}) and number of cycles to failure N_{max} after e=0.37+PDA (a) and e=0.37+500°C (1h)+300°C (t=var) (b) 91

Figure 4.1 Stress-temperature curves obtained during constant-strain heating of the thermomechanically-treated Ti-Nb-Ta (a) and Ti-Nb-Zr (b) samples

(adapted from [28, 29]). Shadowed areas indicate the onset temperatures of the reverse α”→β phase transformation under stress.....98

Figure 4.2 Tensile module for the *PANalytical X'Pert Pro* diffractometer: a) schematics of the working principle; b) schedules of the in situ X-ray diffraction temperature scanning experiments: SF – strain-free; SCP – strain-controlled with loading at RT; and SCM – strain-controlled with loading at -150°C [31].....101

Figure 4.3 Tensile strains measured on heating during SCP and SCM experiments for TNT (a) and TNZ (b) alloys, and tensile loading curves at various recording temperatures for TNT (c) and TNZ (d) alloys. Stress-strain curves (c,d) are obtained in tensile tests similar to [28] 104

Figure 4.4 Beta-phase lattice parameter temperature dependence for SF (a,b), SCM and SCP (c,d) experiments for TNT (a,c) and TNZ (b,d) alloys. – – – are the least-squares regressions taken from a) to c) and from b) to d) to facilitate comparison 105

Figure 4.5 Selected X-ray diffractograms of TNT from SF (a) and SCM (b) experiments. The experimental positions 1-3 from the SF and 1-4 from the SCM experiments in Figure 4.2b are indicated.....107

Figure 4.6 TNT alloy: X-ray line angular coordinates versus diffractogram recording temperature from SF (a) and SCM (b) experiments: ● – β-phase, ○ – α”-phase.....108

Figure 4.7 TNT alloy: temperature dependence of the α”-phase LPs and ε_{max} in SF (a) and in SCM, SCP (b) experiments. The solid lines for a_β, b_β, c_β and ω_β are brought here from Figure 4.3 110

Figure 4.8 Selected X-ray diffractograms of TNZ alloy from (a) SF and (b) SCM experiments. The numbers of the experimental positions 1-3 from the SF and 1-4 from the SCM experiments in Figure 4.2b are indicated 111

Figure 4.9 TNZ alloy: X-ray line angular coordinates versus diffractogram recording temperature from SF (a) and SCM (b) experiments: ● – β-phase, ○ – α”-phase, × – ω-phase.....112

Figure 4.10 TNZ alloy: temperature dependence of the α”-phase LPs and ε_{max} from SF, SCM and SCP experiments: a) calculated using the least squares method and b) calculated directly from the $020_{\alpha”}$, $002_{\alpha”}$ and $200_{\alpha”}$ line $2\theta_{hkl}$ coordinates 115

Figure 4.11 TNT: Selected X-ray diffraction lines integral intensities versus recording temperature from SF (a) and SCM (b) experiments. The

shadowed areas indicate the starting temperatures of the reverse α”→β transformation 116

Figure 4.12 TNZ: X-ray diffraction line integral intensities versus recording temperature from SF (a) and SCM (b) experiments. The shadowed areas indicate starting temperatures of the reverse α”→β and ω→β transformations 117

Figure 4.13 Beta-phase X-ray line width versus recording temperature in SF, SCP and SCM experiments for a) TNT and b) TNZ alloys....118

Figure 4.14 Sequential changes of the 211_{β} peak profile with temperature and stress in TNZ alloy during SCM (a) and SCP (b) experiments 120

Figure 4.15 Schematic representation of the critical temperatures of thermoelastic martensitic transformations under stress. σ_{tr} – transformation yield stress, σ_{cr}^{M} – critical stress for martensite reorientation, σ_{y} – dislocation yield stress. 1 – loading, 2 – heating under load....122

Figure 4.16 Integral intensity of the selected X-ray diffraction lines versus testing temperature from SCM experiment. For comparison, stress as a function of temperature from constant-strain temperature scanning experiment under ε_i=1 % induced strain [11] is shown. Shadowed areas indicate the onset temperatures of the reverse α”→β transformations under stress 123

LIST OF ABREVIATIONS

UTS	Ultimate tensile strength
at.%	Atomic percent
wt.%	Weight percent
bcc	Body-centred cubic lattice
hcp	Hexagonal close-packed lattice
ELI	Extra-low interstitial alloy(s)
SMA	Shape memory alloy(s)
SME	Shape memory effect
M_s	Start temperature of the direct martensitic transformation
M_f	Finish temperature of the direct martensitic transformation
A_s	Start temperature of the reverse martensitic transformation
A_f	Finish temperature of the reverse martensitic transformation
TRMT	Temperature range of martensitic transformation
SE	Superelasticity effect
B19'	Monoclinic lattice
B2	CsCl-type lattice
TMT	Thermomechanical treatment
HTMT	High-temperature thermomechanical treatment
LTMT	Low-temperature thermomechanical treatment
CR	Cold rolling
PDA	Post-deformation annealing
AG	Ageing

EDM	Electrical discharge machining
TEM	Transmission electron microscopy
NSS	Nanosubgrained substructure
NCS	Nanocrystalline structure
SPD	Severe plastic deformation
BF	Bright field image
DF	Dark field image
SAED	Selected area electron diffraction
RT	Room temperature
HV	Vickers hardness

LIST OF SYMBOLS

E	Young's modulus
S_y	Yield stress
δ	Elongation
K_I	Toughness
ΔK_{th}	Fatigue threshold
S_e	Endurance limit
q	Notch sensitivity
e	Logarithmic deformation degree
β_c	Critical minimum level of β-stabilizer content in metastable β Ti-based alloys
β_s	Minimum level of β-stabilizer content in stable β Ti-based alloys
η	Transformation lattice strain among one of lattice parameters
$\sigma_r(\sigma_r^{max})$	Recovery stress (maximum recovery stress)
$\varepsilon_r(\varepsilon_r^{max})$	Recovery strain (maximum recovery strain)
$\varepsilon_{r,1}$	Completely recoverable strain
θ	Theta angle in X-ray diffractometry
ε_{max}	Crystallographic resource of recoverable strain
σ_{tr}	Transformation yield stress
B_{hkl}	X-ray peak mid-high width
I_{hkl}	X-ray peak intensity

INTRODUCTION

Nowadays conventional metallic materials for orthopaedic implants have some limitations: pure Ti and conventional Ti-alloys demonstrate limited biomechanical compatibility (elastic behaviour with rather high Young's modulus), while Ti-Ni-based superelastic alloys are handicapped by their questionable biochemical compatibility related to the presence of toxic nickel in their composition. Thus the search for a new generation of metallic implant materials which would combine biochemical and biomechanical compatibility is still of interest. The most suitable candidates for the role of these new-generation metallic biomaterials are Ti-Nb-based shape memory alloys, especially Ti-Nb-Zr and Ti-Nb-Ta alloys. These alloys contain only biocompatible elements and they manifest superelastic (pseudoelastic) behaviour mimicking that of bone tissue.

In the literature review (Chapter 1), it can be seen from the example of the well-studied Ti-Ni shape memory alloys, that the functional properties of Ti-based shape memory alloys are structure-sensitive, and that their structure and properties can effectively be controlled by thermomechanical treatment. It is also shown that information related to the thermomechanical treatment of Ti-Nb-based shape memory alloys is definitely lacking. Therefore the main objective of this project is to study the interrelations between the composition, the microstructure and the functional properties of superelastic Ti-Nb-Zr(Ta) alloys; and to maximize their functional properties, more specifically the reversible (superelastic) strain and fatigue resistance, through optimization of the alloys' composition and thermomechanical processing.

The influence of the thermomechanical treatment conditions (including cold rolling, post-deformation annealing and ageing) on the structure of Ti-Nb-based shape memory alloys and, consequently, on their functional properties is investigated in-depth (the first and second articles: Chapters 2, 3). An original tensile stage developed for this project (working principle is described in detail in the Annex) makes it possible to carry out low-temperature *in situ* X-ray study under strain and temperature-controlled conditions. Such a study brings us

an improved understanding of the phase transformation features of this new family of metallic biomaterials (the third article: Chapter 4). Results obtained are summarized in the Conclusions, and Recommendations are given at the end.

CHAPTER 1

GENERAL INTRODUCTION

1.1 Requirements of metallic implant materials

Metals are widely used as orthopaedic implant materials (parts of hip, knee, ankle, etc. implants), dental fillings, for craniofacial restoration, and in cardiovascular applications. However, not all metals and metallic alloys can be used in medicine because of the special requirements of medical device materials, such as biocompatibility [1],[2]. Generally, metallic implant materials must:

- Be inert in the human body environment (non-toxic, chemically stable and corrosion-resistant) or, in other words, be biocompatible;

- Have mechanical behaviour similar to that of human body tissues and be stable (in some range) during cycling (for example: hip implant should sustain more than 10^8 of loading/unloading cycles during a lifetime [3]);

- Be straightforward to manufacture;

- Be suitably sterilizable.

1.1.1 Biocompatibility

As mentioned above, biocompatibility implies multiple criteria, the main significance of which can be described by the imperative "do not harm the human body". This means that the implant should be biocompatible at the interface with the human body tissues. This can be realized in three major ways: (1) creation of protective coatings on the implant surfaces (often polymeric), (2) creation of oxide films with a higher biocompatibility than that of the

bulk material, and (3) creation of implants from an originally biocompatible compound. The last way is the simplest and the most suitable, since even in the case of surface film damage or when the surface area of the implant is large (the case of porous implants), the implant material will not harm the human body. Figure 1.1 compares the biocompatibility of some metals and metallic alloys. As seen, some alloys have higher biocompatibility than their individual components, which can be attributed to the protective properties of oxide films (stainless steel, for example).

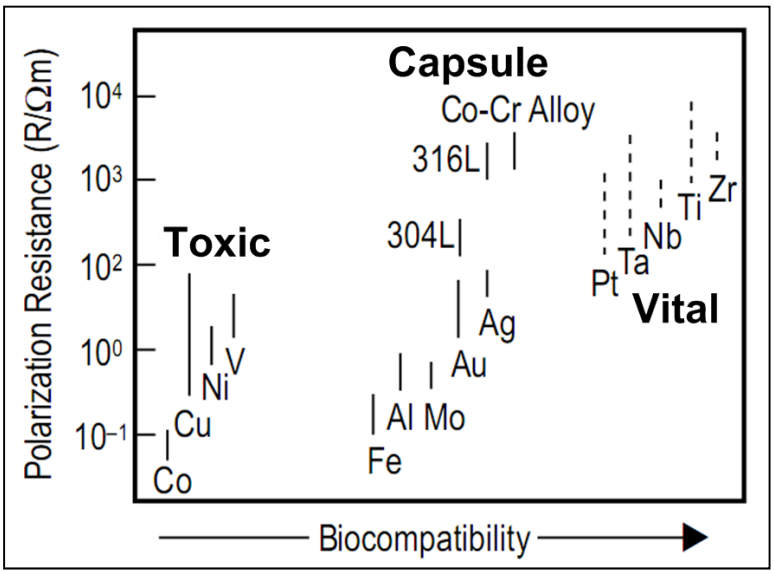

Figure 1.1 The relationship between the polarization resistance and biocompatibility of pure metals, Co-Cr, and stainless steels [4]

1.1.2 Mechanical behaviour

In the case of bone replacement implants, their mechanical behaviour should be similar to that of human bones (Table 1.1). Mechanical behaviour characteristics include static and dynamic or cycling-depending (fatigue) properties. Static properties can be described by the following parameters: Young's modulus (E), yield stress (S_y), ultimate tensile strength (UTS), elongation (δ) and toughness (K_I). Fatigue properties are: fatigue threshold (ΔK_{th}), endurance limit (S_e) and notch sensitivity (q).

Table 1.1 Mechanical properties of bones [3],[5]-[12]

Property*	**Value**
E, GPa	1 – 30
S_y, MPa	15 – 70
UTS, MPa	25 – 150
δ, %	0 – 8
K_I, $MPa\sqrt{m}$	2 – 12
* Mechanical properties of bone tissues are not constant because bones consist of different tissues and have self-accommodated structure under external stress conditions.	

The static properties are easily determined for an implant material. They present a first step in the selection procedure of a particular implant material. The second step is the fatigue properties. Standard fatigue tests of materials involve load or displacement-controlled cycling.

Mechanical properties are very important criteria for selecting an orthopaedic implant material. For example, the mismatch between the mechanical behaviour of an implant and bone results in "stress shielding" phenomena, bone damage and, consequently, implant loosening [13].

1.1.3 Other requirements

Given the high stability of metallic materials, such requirements as sterilizability (sterilizable by steam, ethylene oxide and gamma rays, for example), and manufacturability to intricate shapes and sizes do not generally require any special precautions. However, in the case of some exotic alloys, there are problems with getting a sufficient quantity of homogeneous material for industrial use.

1.2 Types of metallic implant materials

Metallic materials used for implants can be classified as follows: stainless steels, Co-Cr-based alloys, Ti and titanium alloys, Ag-Sn-Cu (dental amalgams) and pure metals such as Au, Pt, Ta, Zr, etc. [2]. Let us consider the advantages and limitations of the most commonly used orthopaedic implant materials. The major mechanical characteristics of these materials are shown in Table 1.2 and Figure 1.2.

Table 1.2 Mechanical properties of metallic implant materials compared with bones

Material	**Property**				
	E, GPa	S_y, MPa	UTS, MPa	δ, %	K_I, MPa$\sqrt{m}$
Stainless steels (austenitic 316L stainless steels) [5]	210	240 – 800	600 – 1000	55 – 20	~100
Co-Cr-based alloys [5]	225	525	735	10	~100
Pure Ta [1],[14]	186 – 191	140	250	20 – 30	–
Pure α-Ti, grade 4 [15]	103	480	550	15	–
Ti-based alloys:					
α+β alloys [1],[16]	100 – 110	585 – 860	690 – 930	6 – 15	~80
β alloys [1],[16]	78 – 84	655 – 908	795 – 137	10 – 22	–
Metastable β alloys [1],[16]	55 – 88	736 – 1060	827 – 1100	10 – 22	–
Cortical bone [3],[5]-[12]	1 – 30	30 – 70	50 – 150	0 – 8	2 – 12

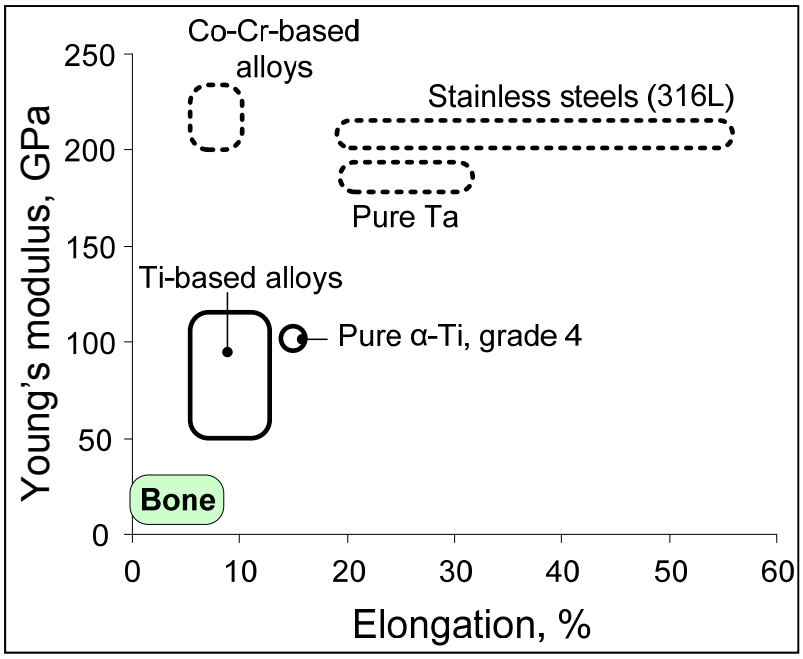

Figure 1.2 Comparison of mechanical properties of metallic implant materials and bone (from [1],[3],[5],[14]-[16])

1.2.1 Stainless steel

These ferrous alloys were the first metallic materials used for implant manufacturing. Distinctive features of this class of metallic implant materials are low cost and availability, whereas disadvantages are insufficient corrosion resistance for long-term use and mechanical behaviour, which is far from the behaviour of bone (Figure 1.2). Stainless steels are most frequently used as temporary fixation devices, such as bone plates, intramedullary nails, rods etc. [1].

1.2.2 Co and Co-Cr-based alloys

Cobalt and cobalt alloys were originally used as dental alloys. These alloys have higher corrosion resistance than stainless steel (Figure 1.1), but, according to some literature data, their biocompatibility is still not good enough [16]. The mechanical properties of Co alloys

are similar to the properties of stainless steel and distant from those of bones (Figure 1.2), which complicates their use as bone tissue replacement. Nevertheless, Co-based alloys are widely used as load-bearing components of orthopaedic implants.

1.2.3 Commercially pure Ta

Figure 1.1 shows that Ta is a vital metal. Due to the fact that Ta is inert to the human body, this material is widely used in surgery and neurosurgery as suture wires for skin closure, tendon and nerve repair; as foils and sheets for nerve anastomosis; clips for vessel ligation; and staples for abdominal surgery. Also, due to their low tensile yield stress (Table 1.2), Ta is successfully used as material for cranioplasty plates and reconstructive surgery and for spongy bone tissue replacement [1]. However, this metal has two significant drawbacks: high Young's modulus (Figure 1.2) and high density (about 16.6 g/cm^3, whereas the density of steel is 7.99 g/cm^3).

1.2.4 Commercially pure Zr

This metal has excellent resistance to corrosion due a self-healing oxide film formed spontaneously in the air or in the water at ambient temperature. Zr is the most biocompatible of the metals (Figure 1.1), but it is not used in pure form, or as a principal alloying element for orthopaedic implants. This may be due to the high cost of the metal itself and its processing, as well as because of the high anisotropy of its properties [17], although the exact answer to this question is not fully clear. At the moment, this metal is used in the implantology as a component of Ti-based implant alloys or "zirconia" ceramics (zirconium oxide) [1].

1.2.5 Ti and Ti alloys

Titanium is the second best biocompatible metal after zirconium (Figure 1.1). Ti and titanium alloys have low Young's modulus (about 100 MPa), which is much closer to that of bone

tissue than other metallic implant materials (Figure 1.2). All that makes titanium the benchmark material for orthopaedic implants. Ti-based alloys have even better properties than pure titanium: Young's modulus of metastable Ti-based alloys can be two times less than that of pure Ti (Table 1.2).

Titanium has two modifications: α (hcp) below 882°C, and β (bcc) above 882°C [18]. Accordingly, titanium alloys may be classified as α, α+β or β depending on their microstructure at test temperature. Their microstructure depends on the type and amount of alloying elements (Figure 1.3). The alloying elements can be divided into three groups: α-stabilizers such as Al, O, N, C; β-stabilizers such as Mo, V, Nb, Ta, (isomorphous), Fe, W, Cr, Si, Ni , Co, Mn, H (eutectoid), and neutral, such as Zr or Hf [1],[16]. Also, properties of titanium alloys depend strongly on their phase structure and composition (Table 1.3).

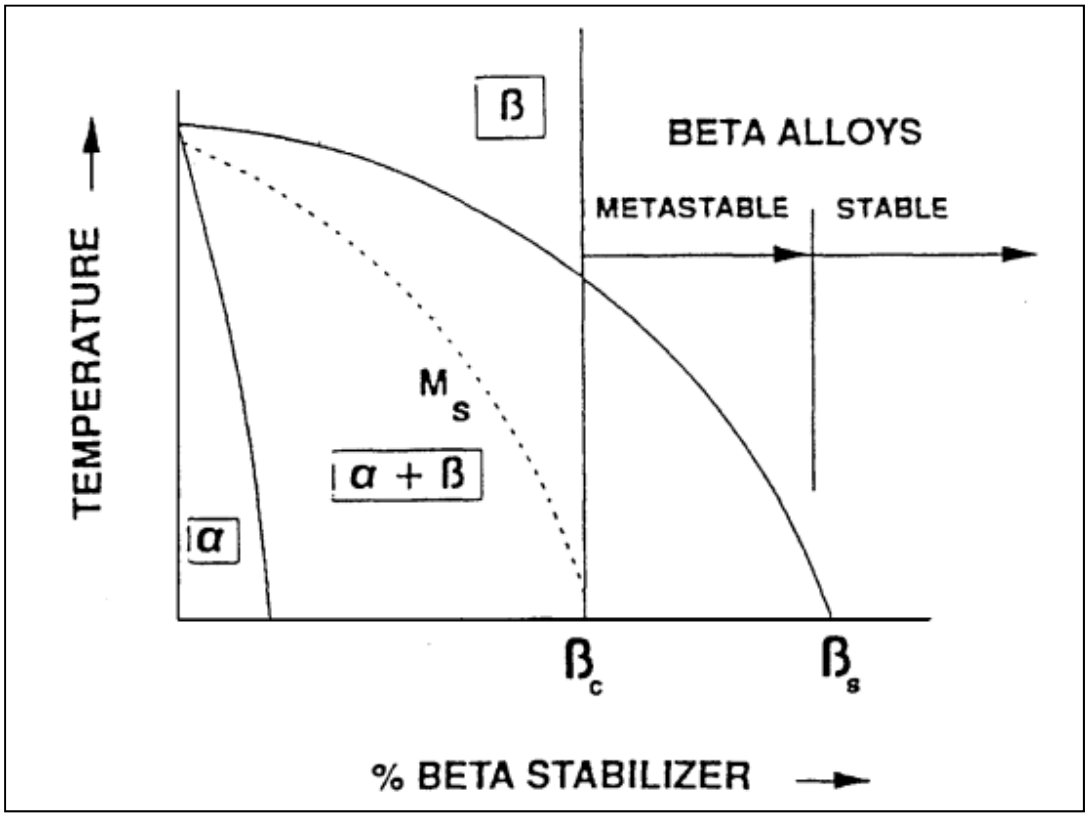

Figure 1.3 Pseudo-binary phase diagram of Ti-β stabilizer [16]: β_c – the minimal content of β-stabilizer for β alloy, β_s – the minimal content of β-stabilizer for stable β alloy

Table 1.3 Orthopaedic alloys and their mechanical properties [16]

Alloy designation	**Microstructure**	**E, GPa**	**S_y, MPa**	**UTS, MPa**
cpTi	A	105	692	785
Ti-6Al-4V	α+β	110	850 – 900	960 – 970
Ti-6Al-7Nb (protasul-100)	α+β	105	921	1024
Ti-5Al-2.5Fe	α+β	110	914	1033
Ti-0/20Zr-0/20Sn-4/8Nb-2/4Ta+(Pd,N,O)	α+β	N/A	726 – 990	750 – 1200
Ti-13Nb-13Zr	α'+β	79	900	1030
Ti-Zr	Cast α'+β	N/A	N/A	900
Ti-12Mo-6Zr-2Fe (TMZF)	Metastable β	74 – 85	1000 – 1060	1060 – 1100
Ti-15Mo-5Zr-3Al	Metastable β	75	870 – 968	882 – 975
	Aged α+β	88 – 113	1087 – 1284	1099 – 1312
Ti-15Mo-2.8Nb-3Al	Metastable β	82	771	812
	Aged α+β	100	1215	1310
Ti-15Mo-3Nb-0.3O (21SRx)	Metastable β + silicides	82	1020	1020
Ti-35Nb-5Ta-7Zr (TNZT)	Metastable β	55	530	590
Ti-35Nb-5Ta-7Zr-0.4O (TNZTO)	Metastable β	66	976	1010
Co-Cr-Mo	Austenite(fcc)+ hcp	200 – 230	275 – 1585	600 – 1795
Stainless Steel 316 L	Austenite	200	170 – 750	465 – 950
Cortical bone [3],[5]-[12]	Viscoelast. composite	7 – 30	30 – 70	50 – 150

1.2.5.1 α and near-α titanium alloys

As the name implies, these alloys do not contain β-stabilizers or their quantity is so small (near-α alloys) that the alloys do not leave the α-phase range. The most common alloying elements of α alloys are Al, Sn, and sometimes Zr. These alloys are generally more resistant

to creep at high temperatures than other titanium alloys. Some of these alloys, such as extra-low interstitial α-alloys (ELI grades, Ti-5Al-2.5Sn-ELI, for example [1]) also preserve their toughness at cryogenic temperatures. Thermomechanical processing does not allow strengthening of these alloys, in contrast to α+β and β alloys, so α-alloys are most often used in the annealed or recrystallized conditions (to remove residual stresses induced by cold working) [1].

Near-α alloys, containing a small amount of β-stabilizers (Ti-8Al-1Mo-1V, Ti-6Al-2Nb-1Ta-0.8Mo, for example [1]) are, properly speaking, α+β alloys, but the amount of β phase is so small that it does not influence the alloys' properties.

Currently, α and near-α titanium alloys are not used as metallic implant materials due to their low strength [1],[16]. In cases where non-load-bearing corrosion-resistant material must be used, commercially pure titanium is preferred to α and near-α alloys [1], because of its higher biocompatibility.

1.2.5.2 α+β titanium alloys

This class of alloys contains both α and β-stabilizers. Furthermore, since the quantity of β-phase is greater in these alloys, α+β alloys exhibit higher strength than α, near-α alloys and commercially pure Ti (Table 1.3). The properties of α+β alloys depend on the composition and relative proportions of the α and β phases [16].

A two-phase structure of these alloys makes it possible to control their properties by thermomechanical treatment. Alloys are often strengthened by solution treatment and ageing [1]. Solution treatment is usually performed at a high temperature corresponding to the two-phase state and followed by quenching in water. As a result, β-phase at the solution treatment temperature may be partially or completely transformed during cooling, due to martensitic transformation. Then, the alloy is aged in a 280 to 650^{o}C temperature range to initiate α-phase precipitation. Ageing produces a fine mixture of α and β phases as a replacement of the

β phase remaining after solution treatment. Such a heat treatment can increase the strength of α+β alloys by 30 or 50% [1]. These alloys are widely used for total joint replacement, hip stems, fracture fixation plates, nails, rods, wire, etc.

1.2.5.3 β titanium alloys

As the amount of alloying elements increases, titanium alloys modify their phase structure from α+β to β (after β_c, Figure 1.3), i.e. β-phase dominates in the structure after quenching in water or air cooling.

In turn, β alloys can be divided into metastable β alloys (composition lies between β_c and β_s, Figure 1.3) and stable β-alloys (composition above β_s). The difference is that stable alloys do not change their phase composition during thermomechanical treatment, whereas in metastable alloys, phase transformation is possible (precipitation of α-phase or other transformations). Virtually all commercial β alloys are metastable, due to the possibility of phase transformation under external load or temperature variation [1].

Thermomechanical treatment of metastable β alloys implies solution treatment and ageing at 450 – 650^{o}C for the partial transformation of β phase into α phase. The α phase is formed in the initial β-phase as fine particles, which can raise the strength of these alloys to the level of α+β alloys. β alloys have several drawbacks: lower creep strength than that of the α+β alloys and lower ductility in aged conditions. However, despite the low plasticity of β alloys, their fracture toughness is generally higher than that of α+β alloys with the same yield stress [1]. Furthermore, β alloys, before ageing (i.e. when they are composed of only β-phase), have excellent ductility combined with a low yield strength, which provides outstanding formability [1],[16]. From the metallic implant materials standpoint, β alloys possess a unique combination of high corrosion resistance and low Young's modulus with sufficient ductility (Figure 1.4).

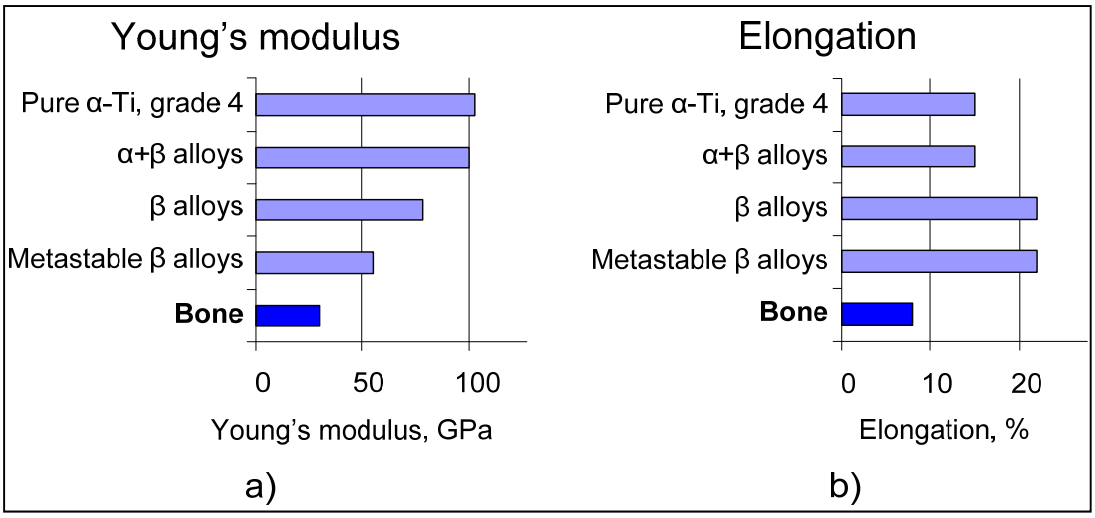

Figure 1.4 Comparison of (a) Young's modulus and (b) elongation of pure titanium and Ti-based alloys with those of bone (from [1],[3],[5],[15],[16])

1.3 Ti-based shape memory alloys

Among metastable titanium β alloys, a special group of these alloys exhibits a shape memory effect (SME) (see Figure 1.5). Generally speaking, shape memory alloys (SMA) are materials that recover their shape due to thermoelastic martensitic phase transformation. This transformation takes place under the influence of external load and/or temperature changes. There are different manifestations of SME: one-way shape memory effect (shape recovery upon heating), two-way shape memory effect (the alloy remembers two shapes, i.e., recovers the shape during both the heating and cooling) and superelasticity (transformation occurs during the alloy deformation at a constant temperature, thereby increasing the range of reversible (quasi-elastic) behaviour. In addition to Ti-based SMA, there are also shape memory alloys based on other metals (Cu, for example) [17],[19].

The following specific parameters are used to describe SMA behaviour: direct martensitic transformation start (M_s) and finish (M_f) temperatures, reverse martensitic transformation start (A_s) and finish (A_f) temperatures (Figure 1.5), as well as the so-called functional properties: the value of recoverable strain and recovery stress, generated by the material upon

heating (shape memory effect) or strain recovery during isothermal loading/unloading cycle (superelasticity).

In fact, for bone tissue replacement material, not only the proximity of the basic mechanical characteristics (E, S_y, UTS, δ) to those of bone is important (see Table 1.1 and Figure 1.2), but also the highly desirable similarity between their behaviour during deformation. As shown in Figure 1.6, in contrast to the majority of metals and metallic alloys, bones have nonlinear elastic behaviour. The behaviour of the superelastic alloy is very different from that of other metallic implant materials being closer to that of bone tissue due to superelasticity and premartensitic lattice softening [20].

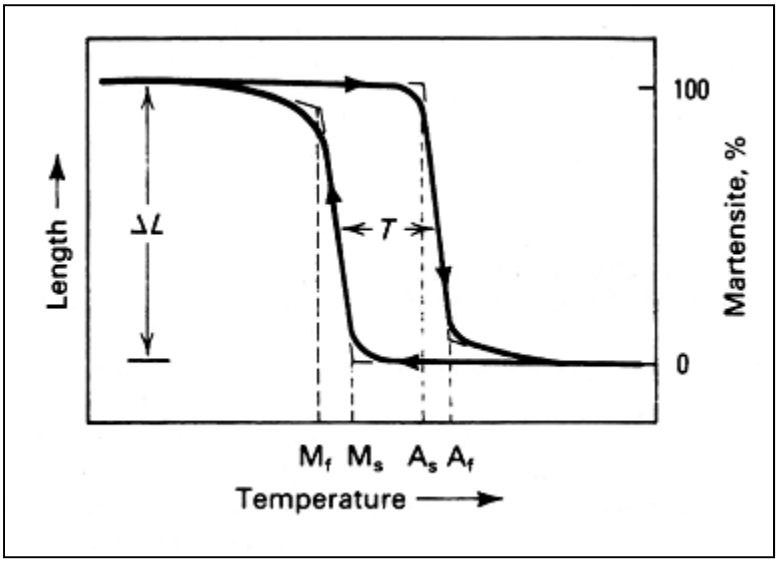

Figure 1.5 Typical transformation versus temperature curve for a shape memory alloy specimen under constant load (stress) as it is cooled and heated [1]

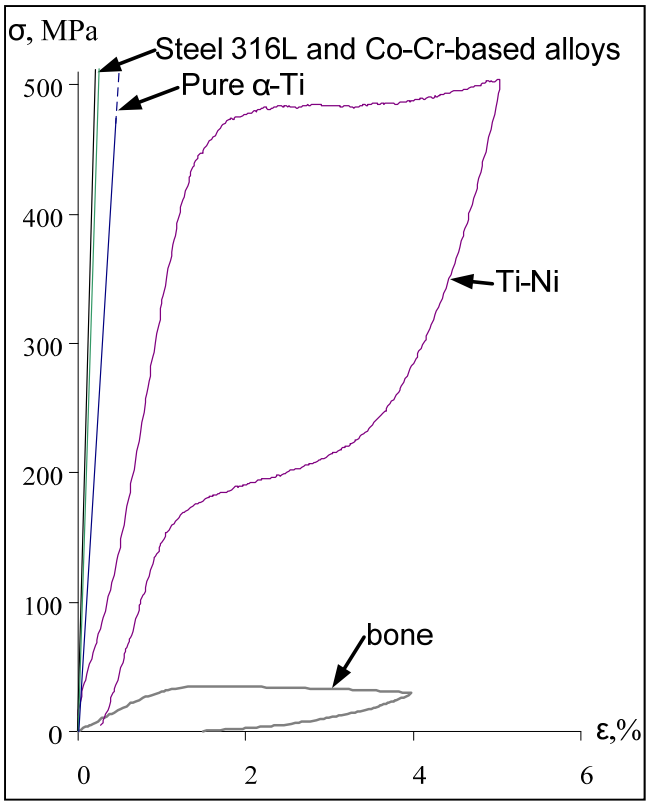

Figure 1.6 Comparison of the stress-strain diagrams of austenitic 316L stainless steel [5], Co-Cr-based alloy [5], pure α-Ti (grade 4) [15], Ti-Ni-based SMA [21] and trabecular bone [22]

Titanium is a very reactive element, so these alloys are melted in vacuum or inert atmosphere. The most frequently used melting methods are plasma-arc, electron-beam and vacuum-induction melting. After melting, an oxide film forms on the alloy surface and it may be subjected to conventional heat treatment [1],[17].

Among all the shape memory alloys, the most common are Ti-Ni-based [1],[19], but these alloys contain toxic nickel, which makes them less suitable for biomedical purposes than the other promising group of SMA – Ni-free Ti-Nb-based alloys. Both groups of alloys will be described in detail in the following section in a comparative manner since they are concurrently contemplated for medical use.

1.3.1 Phase transformation in Ti-based SMA

1.3.1.1 Phase transformation in Ti-Ni-based SMA

Most of the Ti-Ni-based shape memory alloys are binary near-equiatomic alloys (containing 49 – 51at.% Ni) (Figure 1.7), representing the intermetallic compound TiNi. This intermetallic compound is unusual because it has a limited range of solubility of Ti or Ni (Figure 1.7) and a greater ductility than the majority of conventional alloys. The most common alloying is the addition of nickel in the range of 1% in respect of 50at.% Ni.

In addition to the Ti-Ni binary composition, there are many ternary and quaternary Ti-Ni-based alloys. Ternary and quaternary alloys are obtained on the base of Ti-Ni equiatomic alloy, where a part of one component is replaced by the third alloying element or a group of Cu, Al, Fe etc. [24]. Despite the variety of Ti-Ni-based shape memory alloys, only binary alloys are mainly commercially available and widely used [1],[17].

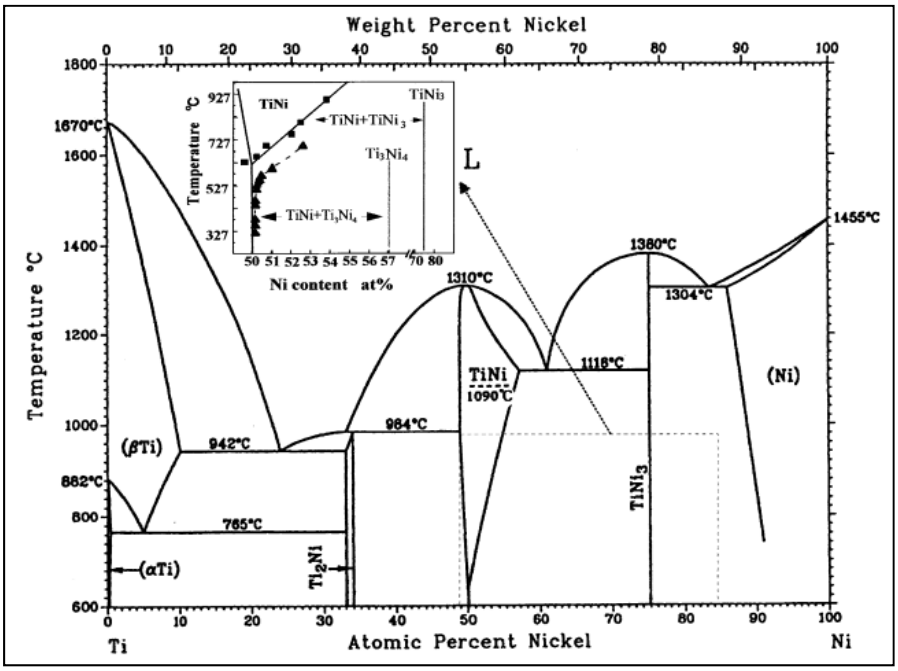

Figure 1.7 Phase diagram of a Ti–Ni alloy, to which the phase equilibrium between the B2 and Ti_3Ni_4 phases is added [24]

Ti-Ni alloys manifest martensitic transformations like all the SMA and, accordingly, have at least two phases: high-temperature phase and low-temperature phase. The high-temperature phase (austenite) is a B2 (CsCl) type ordered structure [25], and the low-temperature phase (martensite) has a monoclinic lattice (B19') [24]. In addition, martensite may have an orthorhombic lattice B19 in the case of alloying by a third element [26]. There is a possibility of martensitic transformation through an intermediate R-phase with the trigonal lattice structure in the case of nickel supersaturated solid solution [24]. Also, a precipitation of Ti_3Ni_4, Ti_2Ni_3 and $TiNi_3$ dispersed particles is possible during ageing (insertion in Figure 1.7). The different types of phase allow martensitic transformation routes (B2→B19', B2→R→B19' and B2→B19→B19' transformations) [24]. The maximum theoretical lattice strain during martensitic transformation is about 11% [19],[27]. Consequently, the maximum recoverable strain is around 8...10%, due to grain misorientation in polycrystalline samples.

1.3.1.2 Phase transformation in Ti-Nb-based SMA

Historically, the minimum concentration of niobium in the Ti-Nb-based SMA is not below 22at.% [28]-[34]. This can be explained by the fact that these alloys are designed primarily as implant materials, where the temperature of the martensitic transformation should be kept around body temperature.

In addition to the binary shape-memory Ti-Nb alloys, there are also ternary and quaternary Ti-Nb-based alloys. As alloying elements, Zr, Ta, Mo, Au, Pd, Pt, Al, Ga, Ge and O are used [35]. Currently, the most promising for medical applications are ternary and quaternary Ti-Nb-Zr, Ti-Nb-Ta and Ti-Nb-Zr-Ta alloys [28]-[31],[35]-[38].

In Ti-Nb alloys, two stable solid-state phases can be observed: high-temperature β-phase (body-centred cubic) and low-temperature α-phase (hexagonal close-packed), as can be seen from the Ti-Nb phase diagram, shown in Figure 1.8 [36]. In this case, the occurrence of martensitic transformation is possible, and high-temperature β phase can be transformed into either α'-martensite (hexagonal) or α"-martensite (orthorhombic) [24]. The maximum lattice

strain during martensitic transformation is about 4% for alloys with niobium content near 22 at.% [39], which is two times lower than that of Ti-Ni alloy.

Besides, low-temperature α-phase can be transformed into ω-phase (hexagonal) [28],[39]. Two types of ω-phase are differentiated: athermal ω-phase (formed during quenching) and isothermal ω-phase (formed during ageing). The interval of the ω-phase formation is approximately 200 – 600^{o}C [39]. The shape memory effect in these alloys is determined by the difference in the lattice parameters of α" and β phases involved in the martensitic transformation [40].

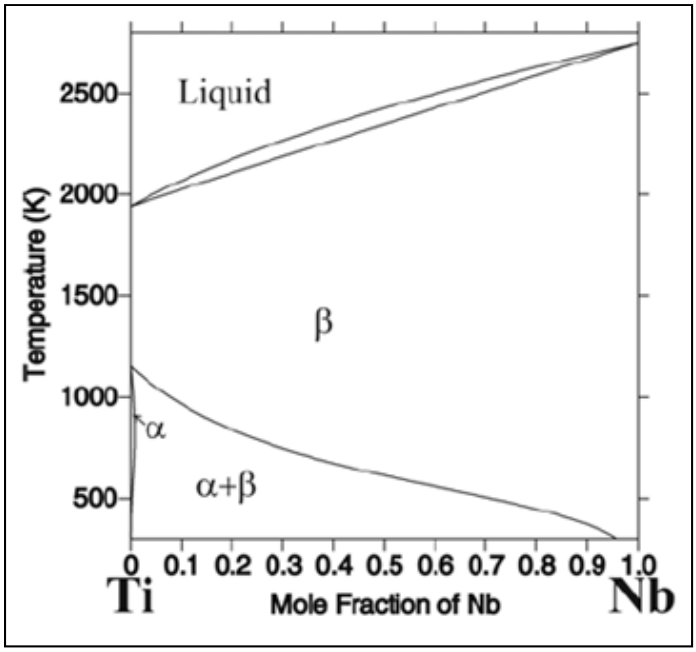

Figure 1.8 Calculated Ti-Nb equilibrium phase diagram [36]

1.3.1.3 Effect of the Ni and Nb contents on the functional properties of Ti-based SMA

In Ti-Ni based SMA, increasing the nickel concentration decreases significantly the martensitic transformation start temperature (M_s) (Figure 1.9) and increases the austenite

yield stress [17],[24]. Consequently, changing the Ni content by 0.1at.% can shift the transformation temperature by 10 – 20 ^{o}C [19]. Alloy composition variations affect the alloy properties by changing the phase structure (for example, precipitation of dispersed Ti_3Ni_4 from the initial austenite [24],[41],[43]) and martensitic transformation sequence.

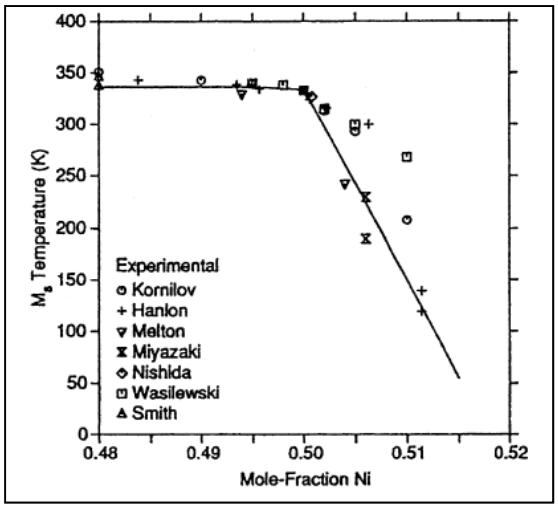

Figure 1.9 M_s temperature as a function of Ni content for binary Ti-Ni alloys [24]

For Ti-Nb-based SMA, the start temperature of martensitic transformation and maximum lattice strain during martensitic transformation increase with decreasing niobium content in the range of 15 to 35at.%. (Figure 1.10) [39].

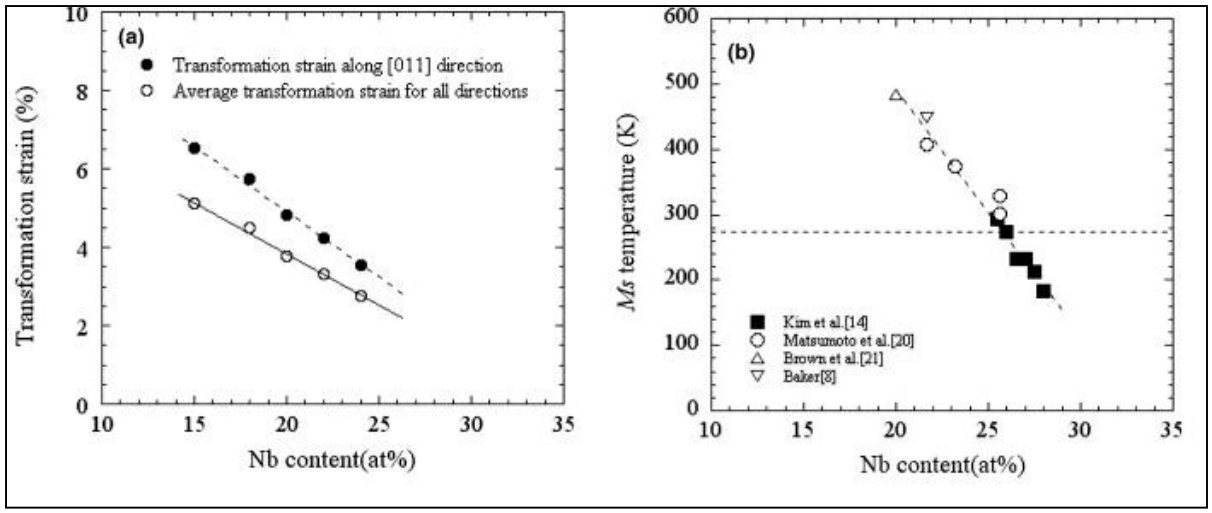

Figure 1.10 Effect of Nb content on the transformation strain (a) and martensitic transformation start temperature (b) [39]

Third elements such as Ta, Zr and O decrease the martensitic transformation temperatures, as shown in Figure 1.11, which should be considered when designing an alloy for medical use. In contrast to the martensitic transformation temperature, the effect of alloying elements on the yield stress and the recoverable strain is not linear, and it is possible to increase the recoverable strain through alloying (for example, Ta in Figure 1.12, [35]).

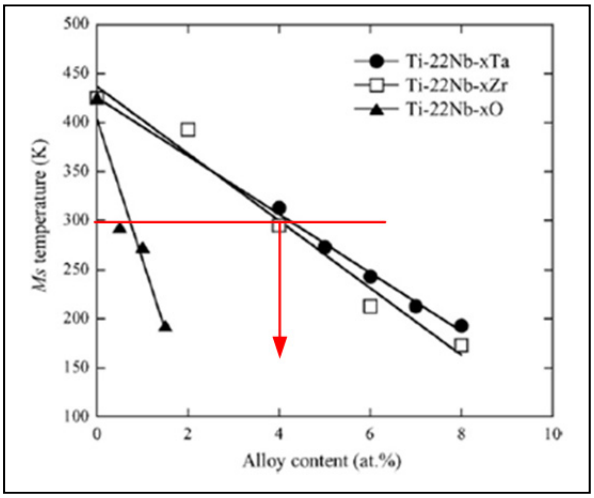

Figure 1.11 Effect of Ta, Zr and O addition on Ms temperature of Ti-22at.%Nb alloy (modified [35])

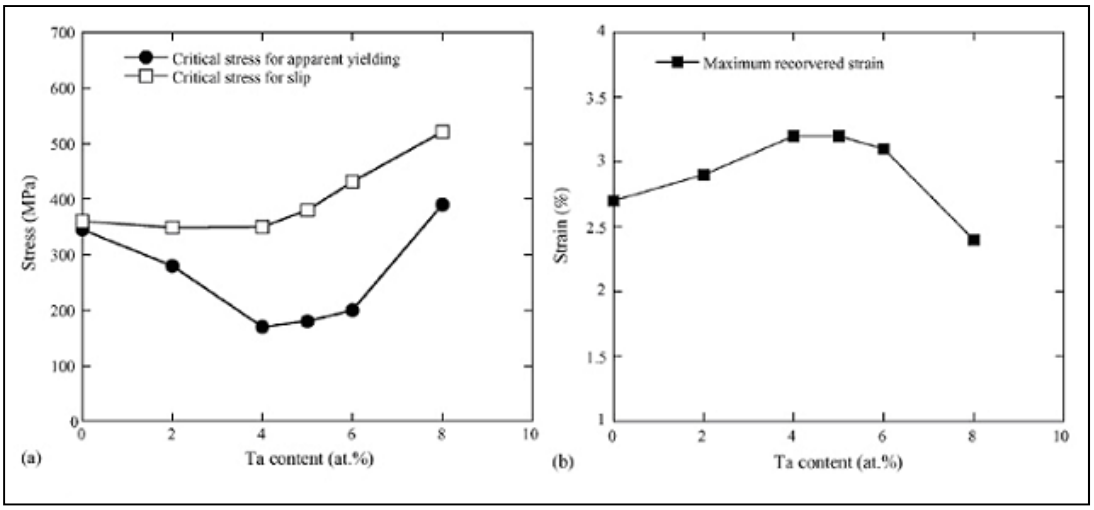

Figure 1.12 Influence of Ta content on (a) critical stress for slip (σ_s) and apparent yield stress and (b) maximum recovery strain of Ti-22at.%Nb alloy (modified [35])

It should be noted that niobium and tantalum are potent β-stabilizers and effectively decrease the Young's modulus of Ti alloys [43]-[45]. Zirconium has a similar effect in combination with Nb or Ta [44]; Zr taken alone is not a strong β-stabilizer [1],[16].

Based on [35],[39],[46]-[48], the three main alloy compositions which are the most promising in terms of body-temperature superelasticity can be selected: Ti-22Nb, Ti-22Nb-6Ta and Ti-22Nb-6Zr (Table 1.4).

Table 1.4 Lattice strains (η_1, η_2 and η_3) of Ti-27Nb, Ti-22Nb-6Zr and Ti-22Nb-6Ta (at.%) alloys [35]

Alloy, at.%	**η_1 (%)**	**η_2 (%)**	**η_3 (%)**
Ti-22Nb	-4.06	4.24	-0.08
Ti-27Nb	-2.04	2.55	-0.39
Ti-22Nb-6Ta	-2.08	2.46	-0.44
Ti-22Nb-6Zr	-2.61	3.37	-0.48

1.3.2 Processing of the Ti-based SMA

The functional properties, as well as the transformation temperature range, not only depend on the chemical composition of the alloy, but are structure-sensitive, which makes it possible to control them by thermomechanical processing (a combination of deformation and heat treatment). The choice of the thermomechanical processing for Ti-based SMA and its parameters may be different depending on the required level of functional properties.

1.3.2.1 Heat treatment

Quenching

Quenching is the heating of an alloy up to the temperature of the austenite recrystallization (700 – 900^{o}C) and subsequent cooling at a sufficient rate to conserve the high-temperature phase at temperatures higher than the martensitic transformation start temperature. This type of treatment is used for alloy softening, for residual stress relaxation, for recovery, homogenization and to prevent diffusion-related transformation during cooling [19].

B2-austenite grains in Ti-Ni do not manifest rapid growth since, when it is heated to 1000^{o}C, the grain size of B2-austenite is less than 50 μm. However, the grain size affects the recovery strain and transformation temperature range. In the case of coarse-grained structures, the resource of recovery strain and transformation temperature range is higher than in the case of fine-grained structures [19].

At the moment, quenching is the most common heat treatment of the Ti-Nb-based SMA. Quenching is generally the reference heat treatment. Thus, most samples are subjected to plastic deformation up to 95%, to post-deformation annealing in the 800 – 1000^{o}C range followed by water-quenching [28]-[31],[33],[39]. After such treatment, despite the high degree of initial strain, recrystallized structure is formed [29]-[31],[33],[49].

Fast cooling is very important in the case of Ti-based SMA because, in these alloys, there may be precipitation of the secondary phase particles (Ti_3Ni_4 in TiNi or ω- and α-phases in Ti-Nb alloys) at temperatures below 600^{o}C.

Ageing

Ti-Ni-based SMA are aged in the 250 – 600^{o}C temperature range. Precipitation of the coherent Ti_3Ni_4 particles is a result of ageing – these particles are oval in shape and their size is 10 – 100 nm [19]. Precipitation of Ti_3Ni_4 leads to a change in the composition and hardening of the initial austenite, which, in turn, affects the functional properties and martensitic transformation temperatures.

Ageing at 250 – 300^{o}C decreases the temperature range of the martensitic transformation, and ageing in the range 300 – 600^{o}C increases the martensitic transformation temperatures [50]-[54]. The initial decrease of TRMT can be explained by accumulation of lattice distortions in the solid solution structure and relaxation of quenching stresses. Ageing at higher temperatures leads to the reduction of nickel concentration in the initial austenite, which increases TRMT (Figure 1.9) [19].

As already mentioned, ageing leads to hardening of the parent phase, i.e. increases the "dislocation yield stress", which leads to enlargement of the difference between the dislocation and the phase yield stresses. Consequently, martensitic transformation can be realized more fully, thereby increasing the value of recoverable strain. The yield stress and ultimate tensile strength of B2-austenite, as well as the consequent maximum recovery stress increase by 5 – 10%, as compared to quenching after ageing of the Ti-50.7at.% Ni alloy at temperatures near 450^{o}C [55]. Ageing in combination with thermomechanical processing can improve the recovery stress and recovery strain [56].

In [30],[34],[37],[39], ageing of quenched Ti-Nb-based SMA in the 200 – 600^{o}C temperature range is performed. With such a heat treatment, dispersed metastable thermal ω-phase and

stable α-phase precipitate. As shown in Figure 1.13, precipitation of these phases strengthens the alloy and increases the UTS and Young's modulus [57].

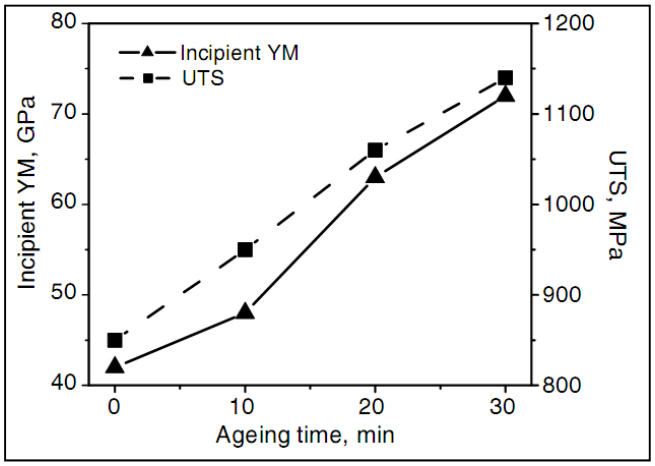

Figure 1.13 Variations of the Young's modulus and ultimate tensile strength of Ti-24Nb-4Zr-7.9Sn (wt.%) alloy as a function of time of ageing at 500^{o}C [57]

From the superelasticity standpoint, ageing may be an effective way to acquire almost perfect superelasticity at RT of Ti-Nb alloys (Figure 1.14) [39].

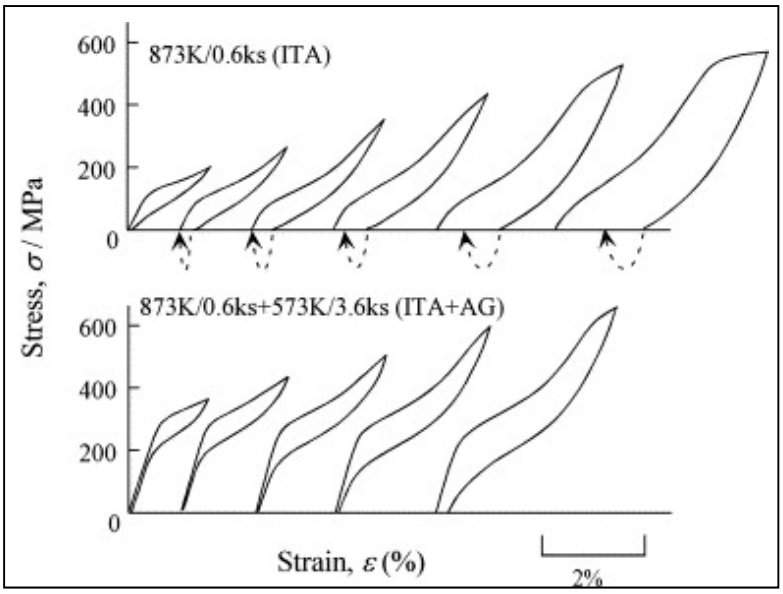

Figure 1.14 Stress-strain curves obtained at RT by cyclic loading-unloading tensile tests for the Ti-26at.%Nb alloy specimen annealed at 873 K for 0.6 ks (intermediate-temperature annealing, ITA) and the specimen aged at 573 K for 3.6 ks after annealing treatment (intermediate-temperature annealing + ageing, ITA+AG) [39]

Thermal cycling

Thermal cycling is carried out through the interval of the martensitic transformation, i.e. direct and reverse martensitic transformations repeatedly occur in the alloy. Thermal cycling may be performed both in stress-free conditions and under applied external stress. Stress-free thermal cycling leads to the strengthening of the initial austenite due to multiple transformation-induced phase hardening [58], while thermal cycling under load creates oriented dislocation substructure and oriented stress fields in the Ti-based SMA [59]-[62]. Both these treatments are commonly used for stabilization of the functional properties and the martensitic transformation temperatures prior to their practical use [19],[63]-[66].

1.3.2.2 Thermomechanical treatment

Thermomechanical treatment involves deformation and thermal treatment which can be carried out simultaneously or sequentially. Historically, thermomechanical treatments have been divided into two types: high-temperature thermomechanical treatments (HTMT) and low-temperature thermomechanical treatments (LTMT). The line between these two types of thermomechanical treatment is conditional and corresponds to 0.5 of the melting point temperature (in Kelvin).

High-temperature thermomechanical treatment

High-temperature heat treatment (HTMT) of Ti-Ni-based shape memory alloys is conducted in the 500 – 1000^{o}C temperature range [19]. Processes of deformation strengthening and softening develop simultaneously during this type of treatment [67]. Consequently, a wide range of structures can be created: from so-called "hot-worked" substructure with a high density of dislocations (more than 10^{10} cm^{-2}) to fully recrystallized structure [68],[69]. However, HTMT is mostly used for the shaping of materials without causing significant changes in their crystalline structure and functional properties.

For Ti-Nb SMA, in some works [38],[57], HTMT at 800^{o}C is used as a preparation technique prior to the main thermomechanical treatment.

Low-temperature thermomechanical treatment

Low-temperature thermomechanical treatment (LTMT) consists of the alloy's deformation at temperatures below the beginning of the recrystallization of the parent phase. It should be noted that the deformation may take place in the temperature range corresponding to martensite, or martensite can be induced and deformed during deformation [19],[70],[71].

LTMT can stabilize and significantly improve SMA properties, such as recovery stress and recovery strain, through the creation of a wide range of dislocation substructures and grain structures [19].

Ti-Ni-based SMA

LTMT is the best studied thermomechanical treatment for TiNi SMA, due to its capacity to regulate the functional properties and temperatures of the martensitic transformation of this material.

Plastic deformation by cold rolling (CR) with e = 0.3 – 2 is most common for Ti-Ni-based SMA, because deformation lower than e = 0.3 is not enough to induce significant structural changes [72],[73], and deformation higher than e =2 can lead to destruction of samples [19]. Let us consider next the impact of different degrees of deformation on the structure and properties of the alloy: the moderate (e≈0.3) and severe (e≈2) deformations.

Moderate plastic deformation (e=0.3) leads to the formation of a well-developed dislocation substructure in martensite (Figure 1.15a). The post-deformation annealing of the cold-worked material causes the reverse martensitic transformation and material softening. When the annealing temperature increases, static recovery and polygonization (formation of subgrain boundaries) occur (Figure 1.15b-e) [74],[75]. With a further increase of annealing temperature, the process of recrystallization and subsequent grain growth will take place. The growth of subgrains is observed in the 200 – 400^{o}C temperature range. Consequently, after 300^{o}C, there is polygonized nanosubstructure, whereas after 400^{o}C, the subgrain size is about 300 – 500 nm [74].

After severe plastic deformation (e=2), mixed nanocrystalline and amorphous structures are formed; the size of the nanograins is about 2 – 8 nm (Figure 1.16a) [74]. Annealing at 300^{o}C forms nanostructure with 5 – 20 nm grain size (Figure 1.16b) [74]. Temperature increase leads to the subsequent grain growth (Figure 1.16c, d). It is impossible to notice any

difference in the structure regardless of the degree of the initial strain, after annealing at 700°C [19],[74].

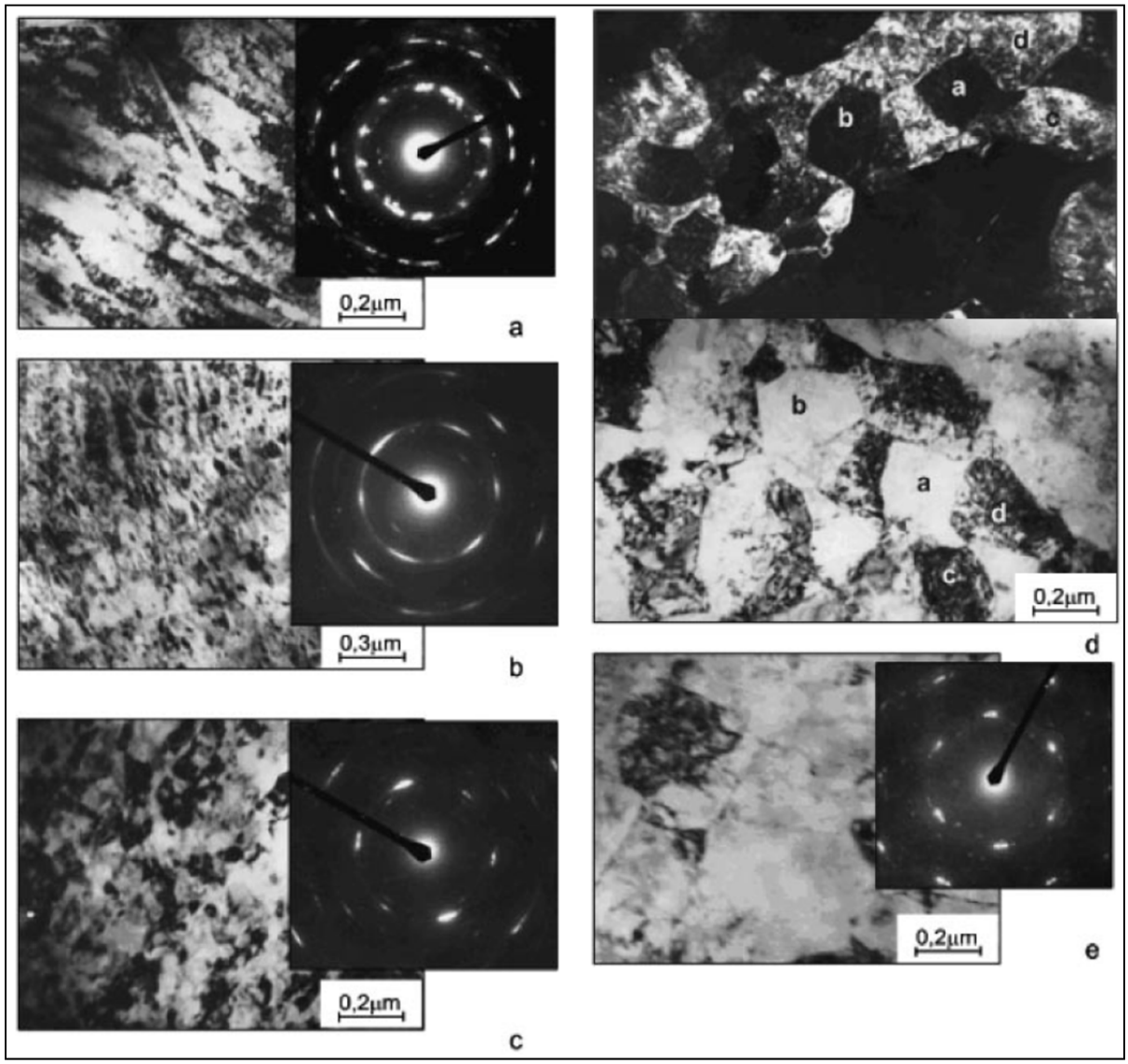

Figure 1.15 Transmission electron microscopy of Ti-50.0at.% Ni alloy subjected to (a) cold-rolling (e=0.30) and cold rolling with post-deformation annealing at (b) 200°C, (c) 300°C, (d) 350°C and (e) 400°C [74]

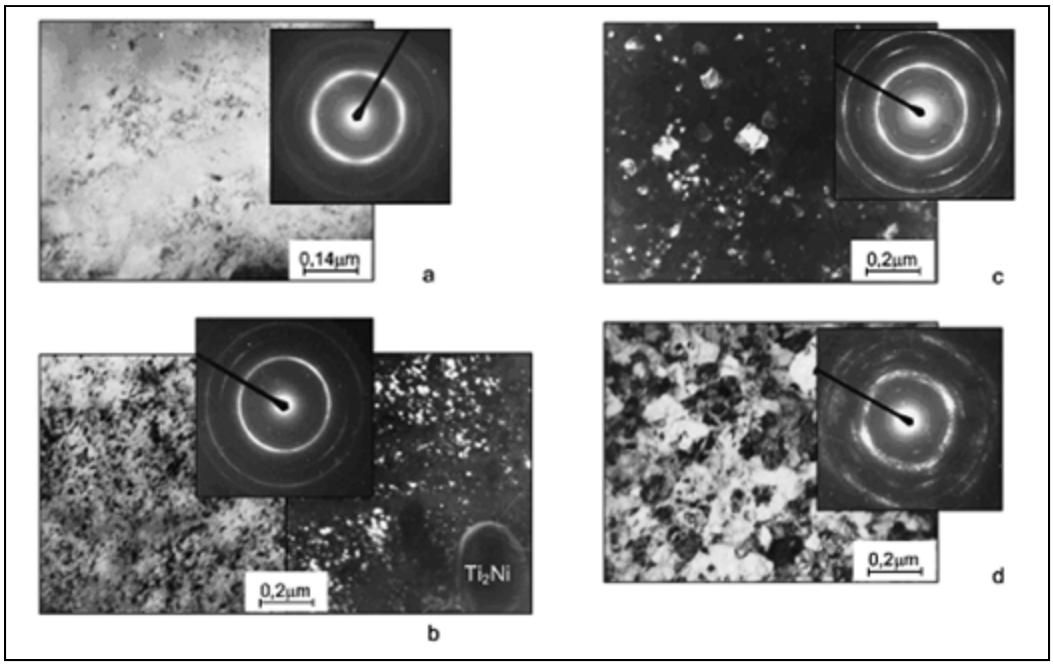

Figure 1.16 Transmission electron microscopy of Ti-50.0at.% Ni alloy subjected to (a) cold-rolling (e=1.9) and cold rolling with post-deformation annealing at (b) 250°C, (c) 300°C and (d) 400°C [74]

As shown in Figure 1.17 and Figure 1.18, thermomechanical treatments significantly affect the functional properties of Ti-Ni SMA. The temperature of martensitic transformation decreases with an increase in the density of defects (Figure 1.17). Additionally, nanocrystalline and amorphous structures lead to a significant reduction in the temperature of martensitic transformation (Figure 1.17c) compared with the polygonization substructure (Figure 1.17a). It should be noted that grain refinement less than a certain size (25 nm) makes the martensitic transformation impossible, according to [76]. With a refining of the structure or substructure in the nanoscale region, the improvement of functional properties is obtained (Figure 1.18). In the case of the nanocrystalline structure, there is a maximum of functional properties: reversible strain is 8%, and recovery stress reaches 1400 MPa, which is 3 – 4 times higher than for the quenched sample [19],[74],[77].

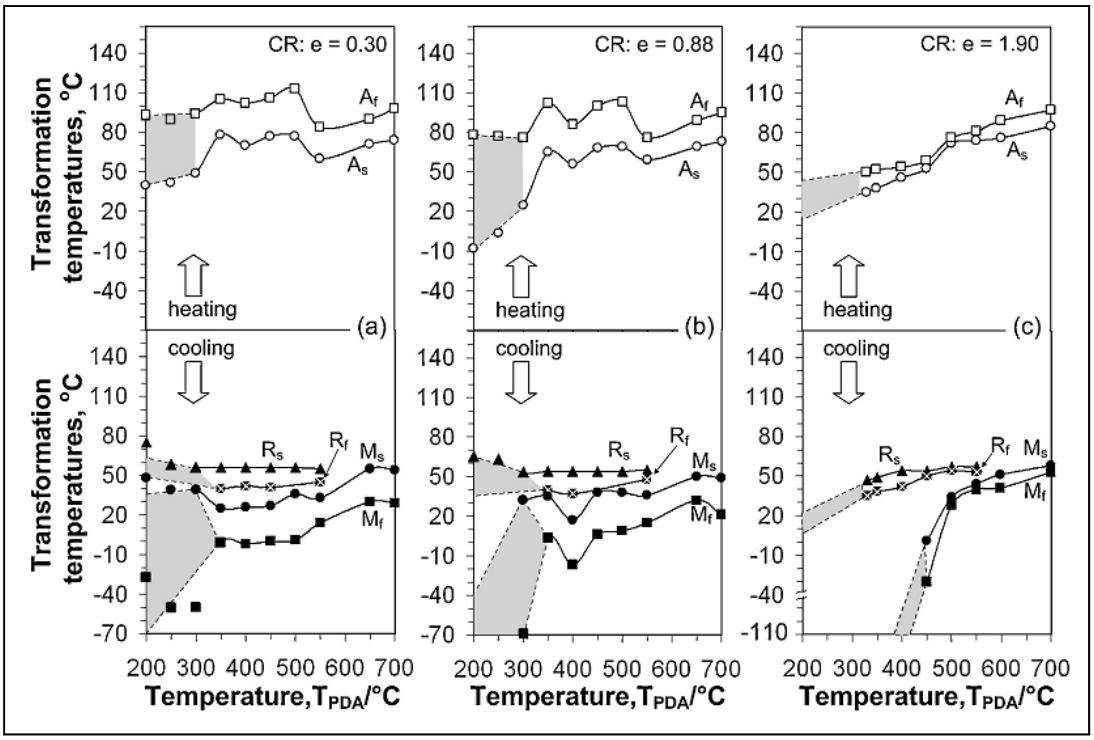

Figure 1.17 Transformation temperatures as functions of the PDA temperature for three levels of cold work (a) e=0.30; (b) e=0.88 and (c) e=1.9 [74]

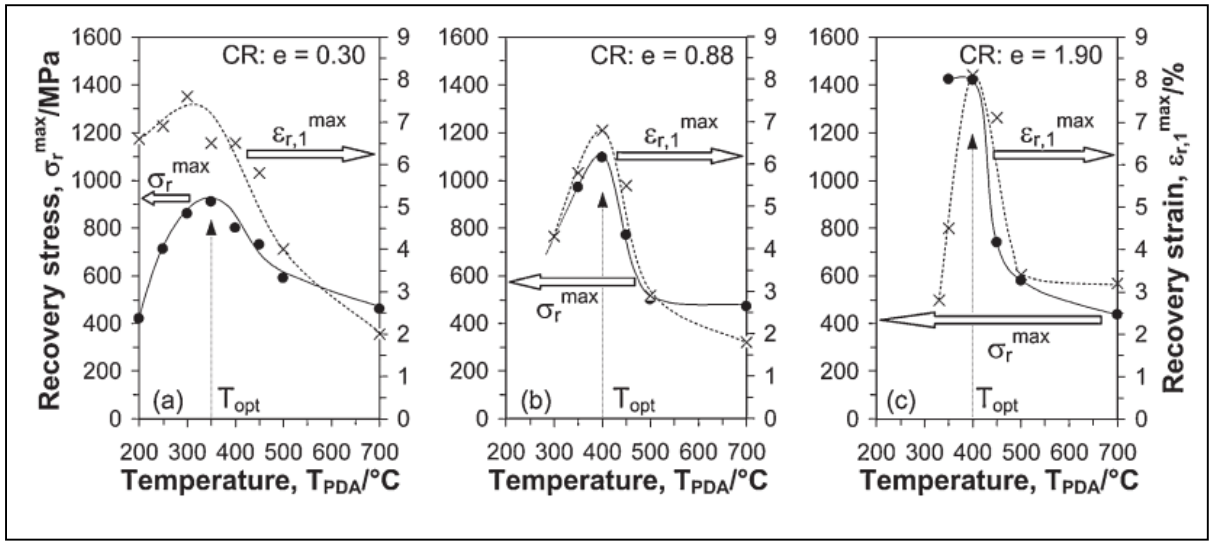

Figure 1.18 Maxima of recovery stress σ_r (●) and completely recoverable strain $\varepsilon_{r,1}$ (0.2% offset) (×) measured as functions of the PDA temperature after different cold works: (a) e=0.30; (b) e=0.88 and (c) e=1.9 [74]

Ti-Nb-based SMA

The influence of cold and warm deformation on the basic mechanical properties of Ti-Nb-based SMA was exclusively studied [32]. Cold deformation of Ti-Nb-based alloys leads to the formation of nanocrystalline structure and the precipitation of a large number of α"-phase in the β-phase particles and results in alloy brittleness [32]. Warm deformation at 200^{o}C allows the α"-phase precipitation phenomenon and reduction of the alloy's brittleness to be avoided, as shown in Figure 1.19 [32]. Regardless of the deformation temperature, increasing the degree of deformation increases the strength and decreases the plasticity and the recoverable strain. The positive effect of this treatment is the decrease of Young's modulus (Figure 1.19a).

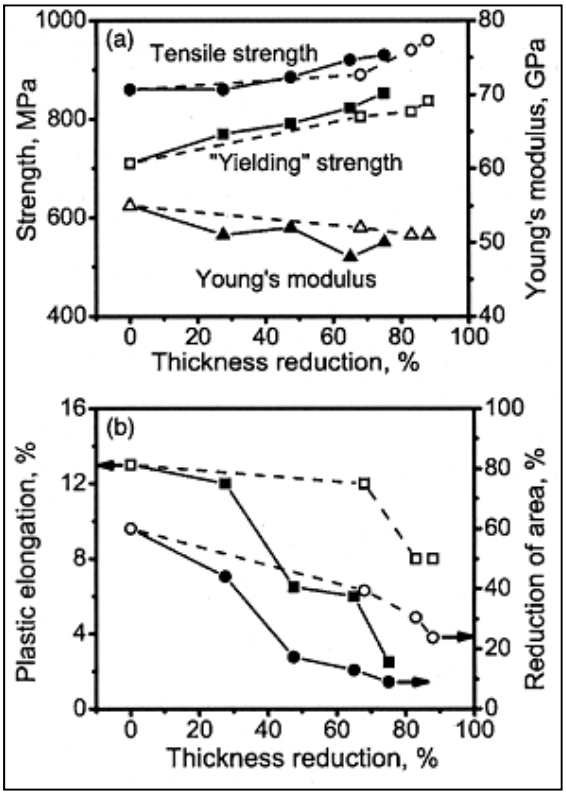

Figure 1.19 Young's modulus and strength (a) and plastic elongation and reduction in area (b) of cold- (solid symbols) and warm- (open symbols) rolled sheets of Ti-24Nb-4Zr-7.9Sn (wt.%) alloy [32]

As seen from the literature analysis, knowledge of the Ti-Nb-based SMA thermomechanical treatment was quite limited at the time of the beginning of the current work. For example, we were not able to find any comprehensive information about the influence of LTMT on the crystalline and phase structure, lattice parameters and functional properties of Ti-Nb-based SMA.

1.4 Research objectives

Despite having lower recovery strain than compared to Ti-Ni SMA, Ti-Nb-based SMA have a very important advantage from the medical applications standpoint. They are Ni-free and may consist of non-toxic alloying elements only. It is known from the literary sources that the functional properties of these alloys are structure-sensitive. Consequently, their functional properties can be controlled by thermomechanical treatment. However, there is not enough information about the effects that thermomechanical treatment has on the functional properties of these alloys. The objectives of my Ph.D. project are therefore:

- To study the interrelations between the composition, microstructure and functional properties of superelastic Ti-Nb-Zr(Ta) alloys;

- To maximize the functional properties of Ti-Nb-Zr(Ta) alloys, more specifically superelastic strain and fatigue resistance, through optimization of their composition and thermomechanical processing conditions.

1.5 Methodology

The methodology used in this work is presented in detail in each article (Chapters 2-5). However, a brief overview of the materials, thermomechanical treatments and characterization techniques used in this work is presented below for better understanding.

1.5.1 Materials

Ti-Nb-based alloys with compositions close to the target (Ti-22Nb-6Zr and Ti-22Nb-6Ta, at.%) are as follows: Ti-Nb-Ta small-weight ingots (about 250 g) cast in *GIREDMET* (Russia), while Ti-Nb-Ta and Ti-Nb-Zr large-weight ingots (about 7 kg) produced in *TSNIICHERMET* (Russia) and *Flowserve Corp.* (USA) correspondingly. Then the ingots are EDM-cut into samples and subjected to thermomechanical treatment. It should be noted that such large-weight ingots of the experimental Ti-Nb-Ta and Ti-Nb-Zr SMA have been obtained for the first time in this work.

1.5.2 Thermomechanical treatment

Based on the literature data, thermomechanical treatment consisted of cold rolling and subsequent thermal treatment such as annealing or/and ageing.

Cold rolling is performed on a *FENN* four-high rolling mill at room temperature with the e=0.3 – 2 deformation range. There are no significant changes in the alloy's structure below this range of deformation; above this range, the material fractures.

Annealing is conducted in a *PYRADIA* laboratory furnace in air. The annealing temperature is varied in the 450 – 900^{o}C range. There are active processes of ω- and α-phase precipitation at temperatures below this range, which is not suitable. The structure is fully recrystallized after annealing at 900^{o}C, and further temperature increase serves no purpose. The alloy is quenched in water after annealing, to prevent precipitation of the isothermal brittle ω-phase.

Ageing is carried out in the 300^{o}C temperature range using the same annealing furnace.

1.5.3 Characterization

Interrelations between the alloys' composition, microstructure and functional properties should be studied at the microstructural and macrostructural levels.

Microstructural analysis consists of the following:

• *Optical microscopy* is a classical tool of crystalline structure analysis. *Metallovert, LEITZ* metallographic microscopes are used with resolution 50×...500×. However, in the case of nanostructured materials, resolution of light microscopy is not enough, and conventional transmission electronic microscopy should be used.

• *Transmission electronic microscopy (TEM)* is a powerful method of a local material characterization. In the current work, *JEM 2100* and *JEM 2100CX*, *JEOL* transmission electron microscopes are used to study the alloys' crystalline and phase structures: grains and subgrains identification, phase identification, structural elements and phase size measurement and characterization. TEM study was carried out at NUST "MISiS", Moscow, Russia.

• *X-ray diffractometry* is used as the main method for integral phase analysis. It was performed with $Cu_{K\alpha}$-rays using *PANalytical X'Pert Pro* and *Ultima IV Rigaku* diffractometers. A thermal chamber *TTK450* attached to the first diffractometer allows us to investigate phase transformations *in situ* in the -150...+100^{o}C range and under external temperature and load variations (using a custom tensile stage fitted within the thermal chamber).

Macrostructural characterization consists of the following:

• *Microhardness testing* is used for express preliminary analysis of the thermomechanical treatment's influence on the mechanical properties of materials. Testing is

performed with an *INSTRON Wilson Tukon 2100* microhardness tester and *Nano-Hardness Tester CSM*;

• *Static and cycling tensile testing* evaluates the mechanical and functional properties of the studied alloys. *MTS' MiniBionix* with a thermal chamber is used for testing in the -35...+60^{o}C temperature range.

• *Thermomechanical testing* consists of stress-free shape recovery and recovery stress generation under load during heating from -150^{o}C to +150^{o}C. The recovery stress testing is performed using the custom laboratory tensile stage with the thermal chamber elaborated *LAMSI*. Thermomechanical testing shows the values of recovery strain and temperature range of reverse martensitic transformation, which are important functional properties of SMA.

1.6 Thesis organization

The main results of the research are presented in three journal articles in Chapters 2, 3, 5 and one conference article – Chapter 4. The latter is a detailed description of a custom-made tensile loading stage for a diffractometer's thermal chamber and its working principle.

- The first article: "**Structure formation during thermomechanical processing of Ti-Nb-(Zr, Ta) alloys and the manifestation of the shape-memory effect**" by S.M. Dubinskiy, S.D. Prokoshkin, V. Brailovski, K.E. Inaekyan, A.V. Korotitskiy, M.R. Filonov and M.I. Petrzhik was published in The Physics of Metals and Metallography, 2011, Vol. 112, No. 5, pp. 503-516. The main objective of this article was to study opportunities to improve the structure formation and functional properties of Ti-Nb-based SMA by means of thermomechanical treatment. The most important results are:

- Cold plastic deformation with subsequent post-deformation annealing can create a wide range of structure, from developed dislocation substructure to fully recrystallized structure;

- Thermomechanical treatment in a studied range does not affect a crystallographic resource of recoverable strain;

- The best combination of functional properties in the studied alloys is obtained in the case of a mainly polygonized substructure of the β-phase with nano- and submicron-sized structural elements.

- The second article with title: "**Structure and properties of Ti-19.7Nb-5.8Ta shape memory alloy subjected to thermomechanical processing including aging**" by S. Dubinskiy, V. Brailovski, S. Prokoshkin, V. Pushin, K. Inaekyan, V. Sheremetyev, M. Petrzhik and M. Filonov was published in the Journal of Materials Engineering and Performance, 2013, Vol. 22, No. 9, pp.2656-2664. The aim of this article was to study the influence of thermomechanical treatment, including ageing, on the structure and functional properties of Ti-Nb-Ta SMA. The most important results are:

  - Low-temperature ageing of the β-phase nanosubgrained structure is accompanied by the ω-phase precipitation phenomena;

  - Depending on the annealing temperature, the studied alloy manifests either mainly superelastic or mainly shape memory behaviour at RT;

  - As compared to an unaged alloy, an "optimum" ω-phase precipitation hardening increases cyclic life;

- The third article with title: "***In situ* X-ray diffraction strain-controlled study of Ti-Nb-Zr and Ti-Nb-Ta SMA: crystal lattice and transformation features**" by S.

Dubinskiy, S. Prokoshkin, V. Brailovski, K. Inaekyan, A. Korotitskiy was submitted to the Materials Characterization journal in August 2013. The objective of this article was the investigation of the crystal lattice and transformation features in Ti-Nb-Zr and Ti-Nb-Ta SMA in the -150...+100^{o}C temperature range with or without external mechanical counteraction. The most important results are:

- Upon heating to M_s the lattice parameters of α”-phase change in the direction of the corresponding “genetically-linked” lattice parameters of β-phase;

- The crystallographic resource of recovery strain in Ti-Nb-Zr at RT is almost double that in Ti-Nb-Ta SMA with the same concentration of alloying elements, and it decreases with heating;

- Application of external load results in certain additional β→α” transformation;

- Application of external load during heating leads to a two-step transformation sequence: ω→β + β→α” (or (β+ω)→α”) transformations precede α”→β transformation in Ti-Nb-Zr SMA;

- The observed reversible β-phase X-ray line widening and narrowing during temperature scanning are the direct result of appearance and disappearance of microstresses caused by reversible thermoelastic martensitic transformation.

CHAPTER 2

ARTICLE #1:
STRUCTURE FORMATION DURING THERMOMECHANICAL PROCESSING OF Ti-Nb-(Zr, Ta) ALLOYS AND THE MANIFESTATION OF THE SHAPE-MEMORY EFFECT

2.1 Summary

This paper studies the interrelation between the structure and the functional properties of Ti-Nb-Zr and Ti-Nb-Ta SMAs for biomedical applications subjected to cold rolling (e = 0.28 – 2.0) and post-deformation annealing (T = 450 – 900^{o}C). As a preliminary evaluation of the microstructure and properties of the thermomechanically-treated alloys, light microscopy and microhardness testing are used. To study in more depth the structure evolution and functional behaviour of these alloys, X-ray diffraction and transmission electronic microscopy analyses and tensile testing are carried out.

Moderate cold deformation (e≈0.3) forms a developed dislocation substructure in the parent β-phase, while severe deformation (e≈2) results in a local formation of nanocrystalline structure without traces of amorphization. Post-deformation annealing (1h) with temperature above 450^{o}C starts a polygonization process: nanosubgrained substructure is created at 500°C, which grows to reach submicron size level at 600°C. In the case of severe plastic deformation (*e*≈2), mixed substructure and crystalline structure is observed in the same range of annealing temperatures. The recrystallization develops at temperatures above 600^{o}C. Traces of ω-phase are visible after annealing at temperatures of up to 550^{o}C. The lattice parameters of the strain-induced α”-martensite are constant in the 600 to 900^{o}C range of annealing temperatures. The most perfect superelasticity is obtained after initial moderate deformation and annealing at temperatures around 600^{o}C, which corresponds to nano- and submicron-sized structural elements and a small amount of the ω-phase. The article was originally written in Russian, then officially translated and published by The Physics of Metals and Metallography in both Russian and English in 2011.

STRUCTURE FORMATION DURING THERMOMECHANICAL PROCESSING OF Ti-Nb-(Zr, Ta) ALLOYS AND THE MANIFESTATION OF THE SHAPE-MEMORY EFFECT

S. M. Dubinskiy[a, b], S. D. Prokoshkin[a], V. Brailovski[b], K. E. Inaekyan[b],
A. V. Korotitskiy[a], M. R. Filonov[a], and M. I. Petrzhik[a]

[a]National Research and Technology University "MISiS," Leninskii pr. 4, 119049 Moscow

[b]Ecole de Technologie Superieure, 1100, rue Notre-Dame Ouest, Montreal, H3C 1K3, Canada

2.2 Abstract

The formation of structure during thermomechanical processing by the regime of cold plastic deformation by rolling and postdeformation annealing (PDA) and its influence on the mechanical properties of Ti-Nb-(Zr, Ta) shape-memory alloys (SMAs) have been investigated. A moderate strain ($e \approx 0.3$) leads to the formation of a developed dislocation substructure in the β phase. With going to severe plastic deformation ($e \approx 2$), a nanocrystalline structure can locally be formed without the amorphization of the structure. There are also present α"-, α-, ω phases in the deformed alloys. When the PDA (1 h) is performed below 450°C, the structure of the β phase changes only slightly. Above 450°C, a polygonized substructure is formed in the β phase, which is nanosubgrained at an annealing temperature of 500°C and transforms completely into a submicron one at 600°C. In the case of severe plastic deformation to $e \approx 2$, in this range of annealing temperatures, high-angle misorientations of blocks are also observed. The recrystallization of the β phase in the Ti-Nb-(Zr, Ta) SMAs develops at temperatures above 600°C. The presence of the ω phase is detected at temperatures of up to 550°C. The lattice parameters of the strain-induced α" martensite formed in the Ti-Nb-Ta alloy are independent of the PDA temperature in the range from 600 to 900°C, where the polygonized substructure transforms into the recrystallized structure of the β phase. The range of PDA temperatures that are most favorable for the manifestation of the effect of superelasticity in the Ti-Nb-(Zr, Ta) alloys is in the vicinity of 600°C.

Keywords: shape-memory alloys, titanium alloys, thermomechanical treatment, structure, mechanical properties

2.3 Introduction

One of the main disadvantages of metallic implants used in orthopedics is a significant difference in their mechanical behavior as compared to the bone tissue. The metallic implants have a higher modulus of elasticity as compared to bone tissue, which results in the loss of the mechanical connection between the implant and bone upon cyclic loading [1]. The shape-memory alloys (SMAs), for example, nearly equiatomic Ti-Ni alloys, exhibit a superelastic behaviour close to that of bone and dental biological tissues, which leads to their wide application in medicine [2–4]. However, their further medical usage is limited by the carcinogenic properties of nickel [5].

The need for metal implants which combine super-elasticity and a low modulus of elasticity, i.e., ensure biomechanical compatibility, resulted in developing the research in the field of binary and multicomponent nickel-free superelastic alloys based on titanium, such as Ti-Nb, Ti-Nb-Ta, Ti-Nb-Zr [6–10]. The shape-memory effect is observed in the titanium alloys in which the alloying elements play the role of β stabilizers and so impede the occurrence of the β → α" phase transformation and lower the temperature of the direct martensitic transformation upon quenching. In titanium alloys, the β stabilizers can be divided into three groups [11, 12].

(1) Elements isomorphic to β-Ti and forming solid solutions with a limited solubility in the α phase (Ta, Nb, V, and Mo).

(2) Elements isomorphic to β-Ti and forming solid solutions with an unlimited solubility in the α- and β-Ti (Zr and Hf).

(3) Elements with a limited solubility in the α- and β-Ti and forming intermetallic compounds, i.e., Mn, Cr, Fe, Cu, Ni, Si, and Co.

The alloying of titanium alloys with niobium and tantalum leads to the formation (upon quenching) of the α" phase by the martensitic mechanism, while an increase in their concentration stabilizes the β phase at room temperature. In the vicinity of the α" + β/β boundary in quenched alloys, Young's modulus decreases and the shape-memory effect related to the reversible β → α" martensitic transformation appears [13]. The alloying of Ti-(Nb, Ta) alloys with zirconium favors solid-solution strengthening and reduces the probability of the formation of a brittle ω phase [14], thereby improving the functional properties of the nickel-free shape-memory alloys [8, 10–12, 14, 15].

It is known that the functional properties of Ti-Ni SMAs can efficiently be controlled by a thermomechanical treatment (TMT) [16–19]. For instance, in shape-memory Ti-Ni alloys upon the transition from a recrystallized structure to a polygonized nanosubgrained substructure of the B2 austenite as a result of TMT there is observed an enhancement of the complex of functional properties (the maximum values of the reactive stress and completely reversible strain, the expansion of the temperature range of the superelastic behavior). The extremely high values of the functional properties are achieved upon the formation of the nanocrystalline structure of the initial austenite [20–22]. The improvement in the properties in this case is due to an increase in the difference between the so-called "dislocation" and "phase" yield stresses [21, 23, 24], which accounts for the delay of the switching on of the mechanism of irreversible plastic deformation.

The polygonized nanosubgrained substructure (NSS) or nanocrystalline structure (NCS) of austenite is formed in the case of a PDA of moderately (upon the true strain by rolling to e = 0.3–0.5) or severely (e from 1.5 to 2) strain-hardened Ti-Ni alloys, respectively [20–22, 24, 25]. The TMT scheme of moderate cold or warm deformation by rolling or drawing is widely used in practice [19, 20, 22, 26]. The common nature of the structural processes underlying the formation of the functional properties of SMAs of the Ti-Ni and Ti-Nb-(Ta, Zr) systems

suggests the possibility of using similar modes of cold plastic deformation and PDA of these alloys to control their structure. Although the different crystal structure of the main phases (ordered B2 in the Ti-Ni SMAs and the β solid solution in the Ti-Nb-(Zr, Ta) SMAs), the different phase composition, and the different diffusion mobility of atoms must certainly make their contributions.

In this paper we have investigated the possibility of forming a nanocrystalline structure and polygonized nanosubgrained substructure of β austenite by the methods of thermomechanical treatment in the Ti-Nb-(Ta, Zr) SMAs, as well as the impact of such a structure on the mechanical properties of these alloys.

2.4 Experimental

Alloys of the Ti-Nb-Ta and Ti-Nb-Zr systems (Table 2.1) have been investigated.

Table 2.1 Chemical composition of the Ti-Nb-Ta and Ti-Nb-Zr alloys (at %)*

Alloy	**Concentration of basic elements, at %**			
	Ti	Nb	Ta	Zr
Alloys of the Ti-Nb-Ta system				
TNT1	74.0	19.5	6.5	–
TNT2	73.0	20.2	6.8	–
TNT3	72.0	21.0	7.0	–
Alloys of the Ti-Nb-Zr system				
TNZ1	76.6	18.3	–	5.1
TNZ2	73.2	21.2	–	5.6
TNZ3	73.4	20.9	–	5.7

* The chemical composition of the Ti-Nb-Ta alloys is given according to the synthesis data.

The alloys of the Ti-Nb-Ta (TNT1, TNT2, and TNT3) system were smelted by vacuum electric-arc melting from pure charge materials in the form of lentil-shaped ingots with a

diameter of 50 mm and a thickness of 15 mm in the center. The ingots were annealed at 900°C for 1 h and cooled in water. The alloys of the Ti-Nb-Zr (TNZ1, TNZ2, and TNZ3) system were smelted by vacuum induction melting followed by hot pressing at 900°C. After pressing, the ingots of the Ti-Nb-Zr alloys looked like cylinders with a diameter of 50 mm and a length of 660 mm. It should be noted that in terms of commercial applications, obtaining of homogeneous ingots of a large weight, 5–10 kg, is preferable, which indeed was achieved in the Ti-Nb-Zr alloys.

The blanks for rolling, with dimensions of 4 × 10 × 50 (Ti-Nb-Ta), 2 × 8 × 20–50, 1.2 × 0.8 × 100, and 2 × 1.5 × 100 mm (Ti-Nb-Zr), were produced from the ingots by electric-spark and abrasive-disk cutting. Then, the alloys were subjected to a TMT, including repeated cold rolling, and a PDA, followed by cooling in water according to regimes given in Table 2.2.

Table 2.2 Regimes of thermomechanical treatment of the Ti-Nb-Ta and Ti-Nb-Zr alloys

Alloy	**Strain upon cold rolling** $(e = \ln\frac{h_1}{h_0})$	**PDA temperature, °C**
TNT1 TNT2 TNT3	0.28 – 0.3	450, 600, 750 (1 h) and 900 (0.5 h)
TNZ1 TNZ2 TNZ3	0.27 – 0.47, 0.75, 2.75 0.3, 2.0 0.37, 2.0	450, (500, 550 (only TNZ2)), 600, 750, 900 (1 h)

The limits for the degree of deformation during cold rolling were chosen from the following considerations. The lower limit of the degree of strain is determined by the value of the deformation which provides strain hardening that is sufficiently strong to ensure processes of polygonization and recrystallization during annealing [23]. The upper value of the degree of

deformation is determined by the ability of the material to be deformed upon cold rolling without failure. For the alloys similar to those under consideration, it is from 95 to 99% [27].

The temperature range for PDA (see Table 2.2) was chosen assuming that at a minimum annealing temperature (450°C) the processes of recovery begin developing, and after annealing at the maximum temperature (900°C) a fully recrystallized structure of the β phase is formed.

The samples for metallographic studies were prepared by polishing on a P120–P1200 abrasive paper and, then, on a felt wheel using an emulsion of aluminum oxide, Al_2O_3, with a particle size of about 1 micron. The microstructure was revealed by etching in $2HF : 1HNO_3 : 17H_2O$, $1HF : 15HNO_3 : 5H_2O$, and $1HF : 4HNO_3 : 5H_2O$ solutions in different sequences, depending on the type of the preceding TMT; and was examined using a Metallovert LEITZ light microscope. The thin foils for electron microscopic studies using a JEOL 2100 microscope were produced by electrolytic polishing of plates 0.1 mm thick at -38°C in a 15% alcohol solution of HNO_3 using a Tenupol-5 apparatus. To determine the phase composition and to evaluate the theoretical reserve of the reversible strain, X-ray diffraction studies using a Panalytical X'Pert Pro and a Rigaku D/MAX 2500 diffractometers were performed. The samples for the X-ray diffraction study were prepared similarly to those for metallographic investigation to remove the work-hardened surface layer.

The lattice parameters of the phases and the maximum lattice strain upon the martensitic transformation were calculated by the methods similar to those described in [28–30]. The theoretical reserve of reversible strain was evaluated for an isotropic polycrystal as well. The lattice parameters of the α" martensite were calculated based on its X-ray diffraction lines by the least squares procedure. The lattice parameters of martensite were calculated for the cases where the number of distinct lines of the α" phase was no less than five ({110}, {020}, {021}, {130}, and {131}). The lattice parameters of the β phase used in the calculations were determined by extrapolation to $\theta = 90°$.

The hardness measurements were performed at room temperature using an Instron Wilson Tukon 2100 (500 g, 10 s) and a Nano-Hardness Tester CSM. The isothermal mechanical tensile tests were carried out at temperatures of -18, 25, 37, 75 and 200°C employing a specially designed testing machine and an MTS MiniBionix unit at -35, -20, 0, 25, 60, and 100°C.

2.5 Results and discussion

Light Microscopy

The lightmicroscopy study showed that in its original state, before cold rolling, the grain structure of the β phase in the Ti-Nb-Zr and Ti-Nb-Ta alloys was equiaxed, with grain sizes from 200 to 500 microns. In the Ti-Nb-Zr alloys, after cold rolling to an intermediate strain e = 0.75, elongated grains of the β phase (Figure 2.1a) are observed. After annealing at 450°C, this structure is retained almost unchanged (Figure 2.1b, c). After annealing at 600°C, a recrystallized structure is observed to start forming; i. e., there appear separate recrystallized grains with a size of 10–20 μm within the initial grains and along their boundaries (Figure 2.1d, e). With a further increase in the annealing temperature, complete recrystallization (750°C) and growth of recrystallized grains (900°C) take place (Figure 2.1f–i). Inside the β phase grains, individual crystals of the α phase or their groups are observed.

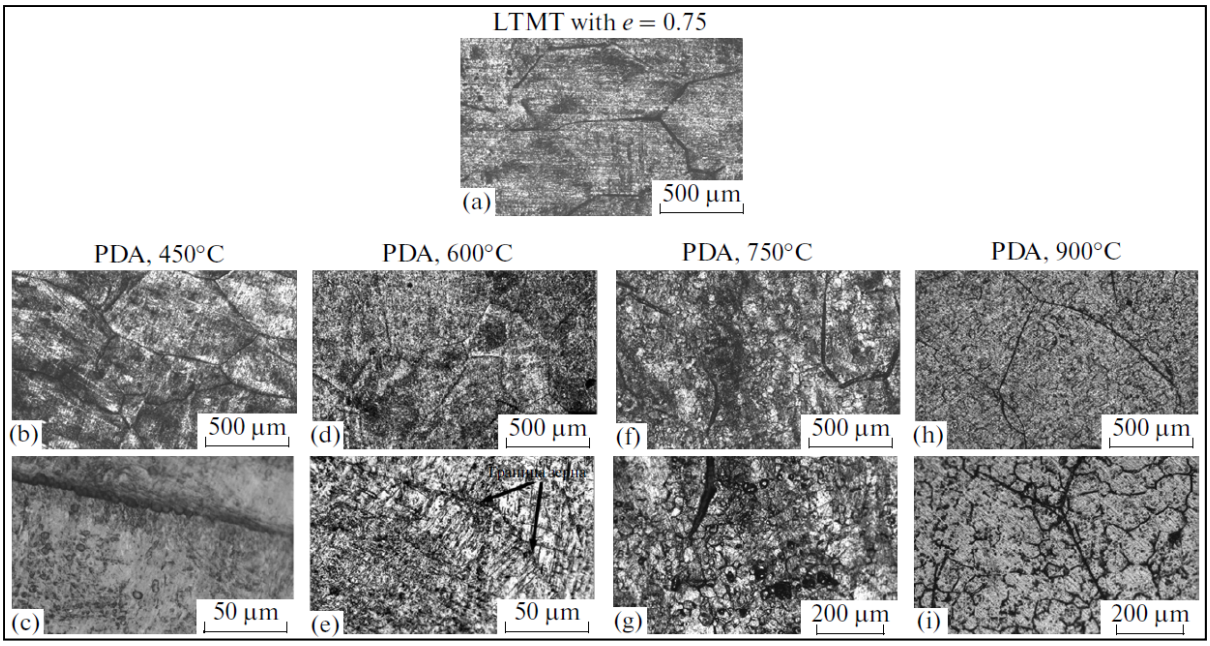

Figure 2.1 Structure of the Ti-18.3Nb-5.1Zr (TNZ1) alloy after (a) deformation to e = 0.75 and postdeformation annealing for 1 h at (b, c) 450, (d, e) 600, (f, g) 750, and (h, i) 900°C. Light microscopy

Of special note is the effect of "grain boundary heredity" [31], which is clearly observed after annealing at 900°C (Figure 2.1i). This effect consists in the retention of traces of the initial boundaries of deformed grains against the background of the fine recrystallized structure, whose grains as if inherit these boundaries. In fact, there are etched out not the high-angle boundaries of large initial grains themselves, but only their "traces" due to an enhanced etchability of the border regions of the initial grains that were enriched by impurities at the preliminary stage of processing. The smaller structural elements within the "traces" of the grains are the really grown recrystallized grains.

In the Ti-Nb-Ta alloys, the boundaries of fine grains are not etched after cold deformation (e = 0.3) and PDA at 450 and 600°C, which indicates the absence of recrystallization. The fully recrystallized β phase was detected after annealing at 700°C (Figure 2.2a). The parallel stripes of different orientations in different grains represent surface deformation-induced martensite crystals formed during mechanical polishing of the sample surface.

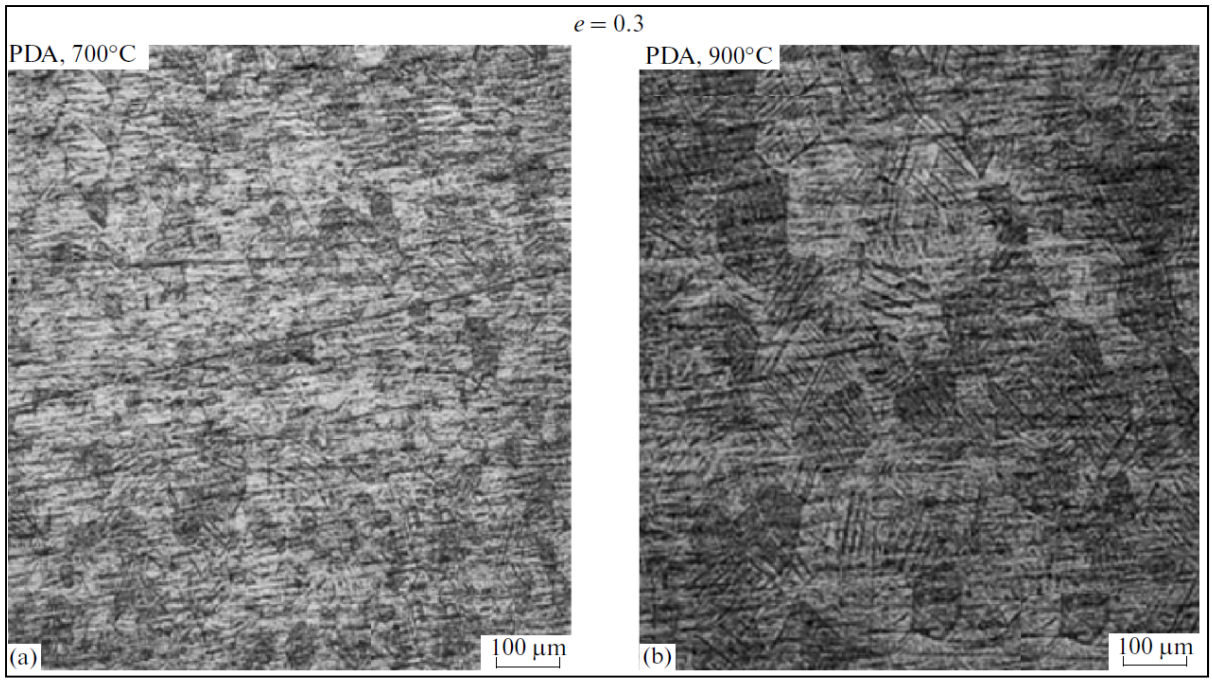

Figure 2.2 Structure of the Ti-19.5Nb-6.5Ta (TNT1) alloy after deformation to $e = 0.3$ and postdeformation annealing for 1 h at (a) 700°C (1 h) and (b) 900°C (30 min). Light microscopy

X-ray Diffraction Investigation

X-ray diffraction study of the TNZ1 alloy was performed at room temperature in the undeformed state, after cold plastic deformation in the range of $e = 0.28$ to 2, and after PDA at temperatures from 450 to 900°C. In the initial state and after any type of deformation, it is the β phase that remains main. There are also an additional phase, the α" martensite, formed during deformation and further deformed plastically together with the β phase, as well as α- and ω phases. After the PDA at all temperatures, the β phase remains basic.

The moderate cold deformation (e = 0.28) leads to a sharp broadening of the X-ray diffraction lines of the β phase (Figure 2.3). An increase in the initial strain to $e = 2$ is accompanied by a gradual increase in the width of the X-ray lines (see Figure 2.3) the increment of which is much less than that observed in the Ti-Ni alloy under the same conditions [32]. Thus, the {110}-line width after deformation to $e = 2$ in the TNZ1 alloy is

0.75° on the 2θ scale (Figure 2.3), while in the Ti-50.26%Ni alloy it reaches 5°, and the Ti-Ni alloy becomes nanocrystalline and partly amorphized [32]. Therefore, no significant development of the nanocrystalline structure and, especially, of the amorphous one can be expected in the Ti-Nb-Zr alloy, in contrast to the Ti-Ni alloys, during SPD to $e = 2$.

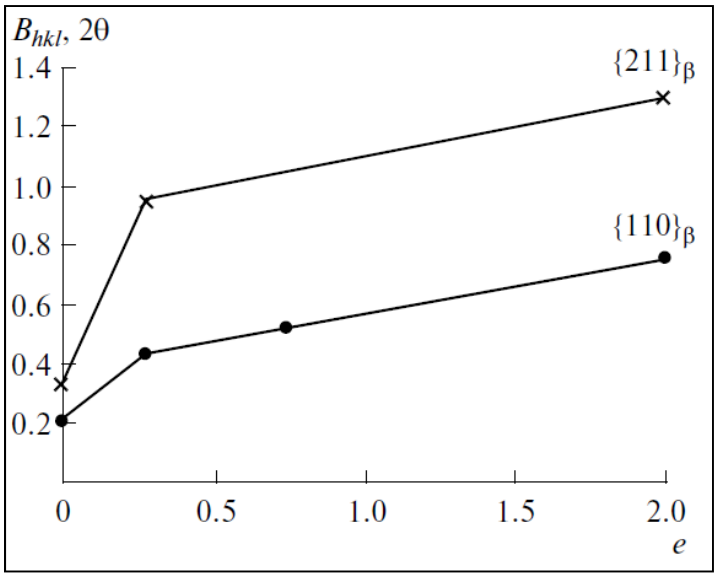

Figure 2.3 Dependence of the X-ray diffraction line width B_{hkl} of the β phase on the degree of initial deformation in the Ti-18.3Nb-5.1Zr (TNZ1) alloy

The X-ray diffraction lines of the β phase after annealing at 450°C remain strongly broadened (Figure 2.4a–c); i.e., the initial strain hardening is largely preserved. The β-phase texture changes only a little, which confirms the absence of recrystallization.

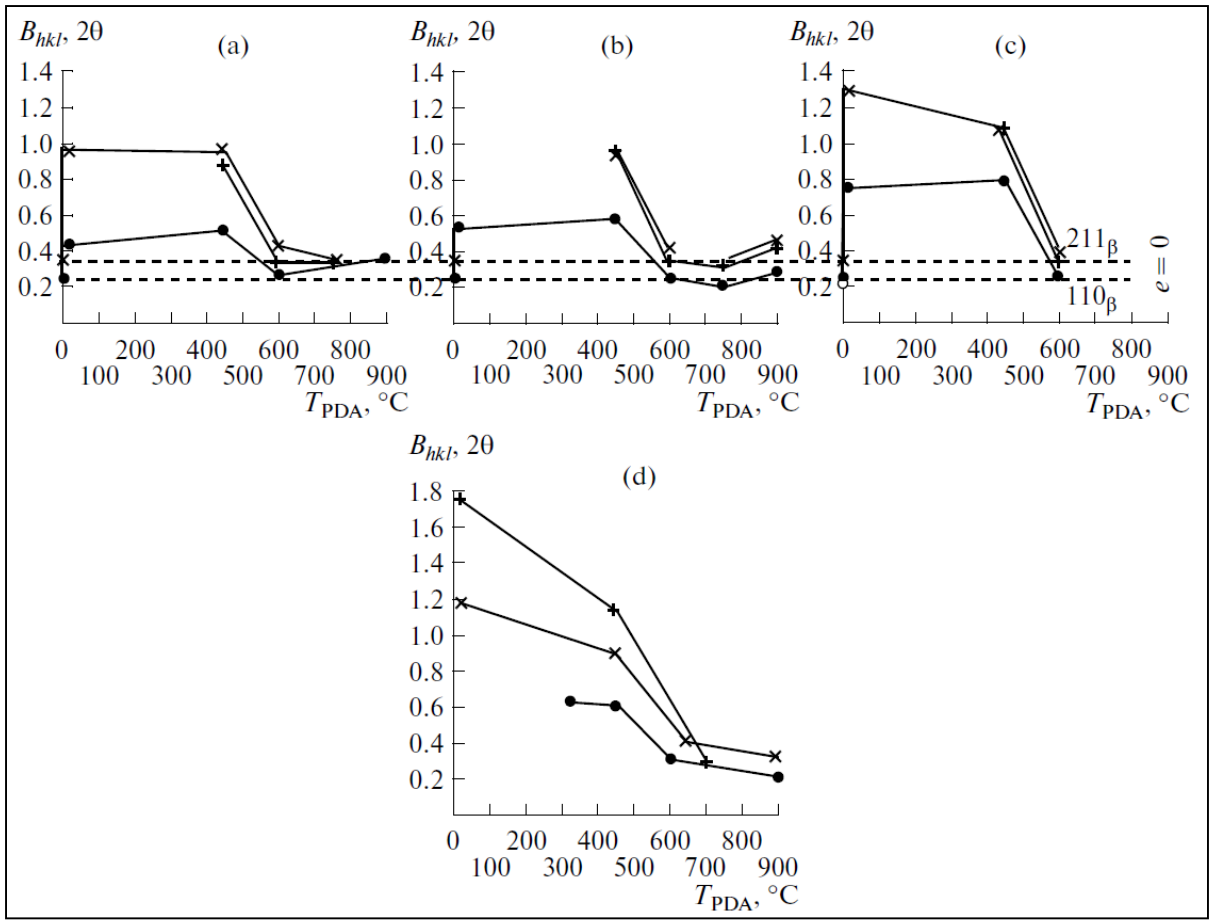

Figure 2.4 Variation of the width of the X-ray diffraction lines of the β phase of the Ti-18.3Nb-5.lZr (TNZ1) alloy after deformation to (a) e = 0.28, (b) 0.75, and (c) 2; and (d) the Ti-19.5Nb-6.5Ta (TNT1) alloy after deformation to e = 0.26 and postdeformation annealing. Horizontal lines indicate the levels of B_{hkl} for the quenched state (e = 0) (×) 211β, (+) 200β, and (●) 110β

After the PDA at 600°C the line widths drop sharply, approaching values typical of the initial undeformed state, and after the PDA at 750°C they reach these values, which corresponds to the complete recrystallization (Figure 2.4a–c).

After the PDA at 900°C, there is seen some broadening of the lines as compared to 750 °C (Figure 2.4b, c), which can be related to the superposition of additional lines, to the incomplete etching-off of the surface work-hardened layer, or to the dissolution of Zr atoms, which have a larger atomic diameter. The latter factor is supported by a systematic increase

in the lattice period of the β phase with increasing annealing temperature to 900°C (Figure 2.5).

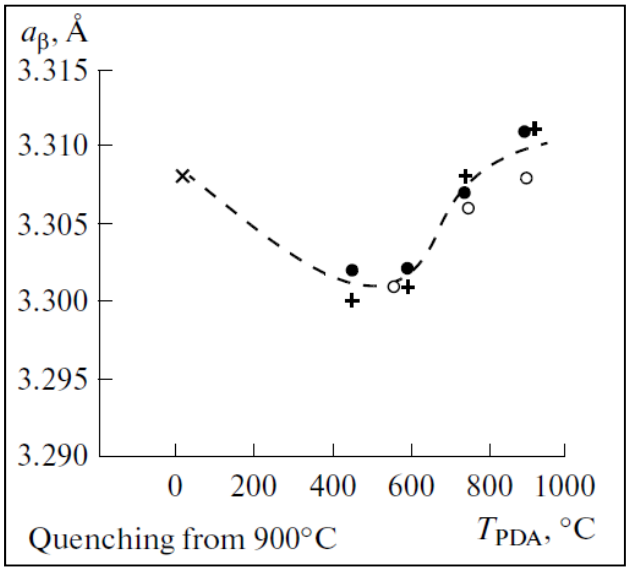

Figure 2.5 The lattice parameter of the β phase in the Ti-21.2Nb-5.6Zr (TNZ2) alloy after different treatments: (×) $e = 0$ (quenching at 900°C); (●) $e = 0.28$; (+) $e = 0.75$; and (○) $e = 2$)

The {101} and {102} lines of the α phase are clearly observed after PDA at all temperatures, and the {001} line of the ω phase is detected only below 600°C

Figure 2.4d presents the data on the widths of the X-ray diffraction lines of the β phase in the TNT1 alloy taken at room temperature after cold deformation by rolling with a reduction to $e = 0.26$ and PDA at a temperature from 450 to 900°C. This figure shows that the X-ray lines of the β phase in the deformed TNT1 alloy become broader as compared to those observed in the Ti-Nb-Zr alloy. The behavior of the width of the X-ray lines in the TNT1 alloy after PDA is similar to that observed in the Ti-Nb-Zr alloys (Figure 2.4a, d). Under such a deformation at $e \approx 0.3$ the lines of Ti-Nb-Ta become broader than those in Ti-Nb-Zr.

The most important functional property of SMAs is the reversible strain, whose crystallographic reserve is determined by the maximum strain of the crystal lattice during martensitic transformation [33]. In other words, this reserve is determined by the ratio of the lattice parameters of martensite and high-temperature phase (austenite), and it is equal to 3–4% in such SMAs as Ti-Nb-Ta and Ti-Nb-Zr [8, 9]. Since the lattice parameters of martensite in the Ti-Ni SMAs and, hence, the strain during martensitic transformation depend on the extent of the defectiveness of the initial phase [21, 28, 29, 34], it was interesting to check whether this dependence manifests itself in alloys based on Ti-Nb as well.

The X-ray diffraction patterns of the TNT1 alloy were taken at room temperature. The samples after rolling to $e = 0.28$ were annealed at temperatures of 450, 600, 750, and 900°C (with cooling in water) and then subjected to tensile deformation to fracture. From these X-ray diffraction patterns, it was only possible to calculate the lattice parameters of the α" martensite in the case of annealing at 600°C and higher temperatures. In the case of annealing at 450°C, the small amount of martensite prevents obtaining the number of lines sufficient for calculations. At the same time, the greatest change in the lattice parameters of the martensite should be expected at a lowest PDA temperature of 450°C when, judging from the large broadening of the X-ray lines, there is retained a high defectness of the structure [34, 35]. The PDA temperature equal to 600°C refers to the region of transition from polygonized substructure to the recrystallized structure (according to the residual broadening of X-ray lines, see Figure 2.4d); and the retained dislocation density seems to be insufficient to affect the lattice parameters of martensite.

Figure 2.6 depicts the calculated parameters of the orthorhombic α"-martensite lattice *a*, *b*, and *c* and the volume of the unit cell of the ω TNT1 alloy after deformation to failure at room temperature as a function of the PDA temperature. As is shown in the figure, the lattice parameters of martensite do not differ after PDA within the measurement error in the temperature range from 600 to 900°C. Therefore, the maximum lattice strain upon the martensitic transformation calculated from the lattice parameters of the martensite and the

β phase turned out to be the same. Its values after the PDA at 600–900°C lie within ε_{max} = 3.0 ± 0.2% (Figure 2.6).

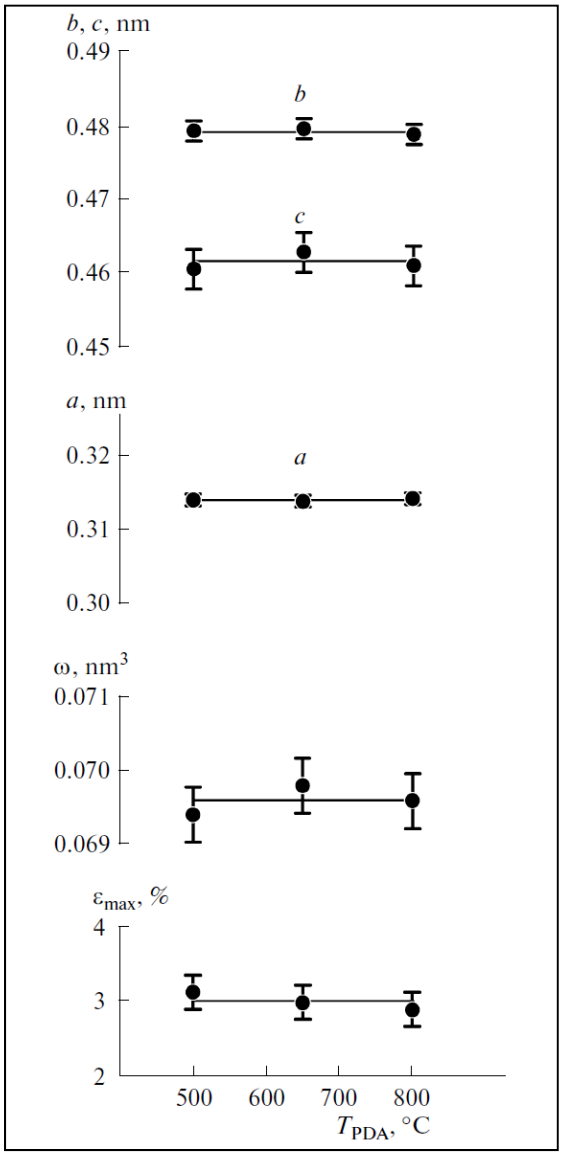

Figure 2.6 Lattice parameters of the α" martensite and the maximum strain of the lattice upon the martensitic transformation of the Ti-19.5Nb-6.5Ta (TNT1) alloy after rolling to e = 0.28, annealing at different temperatures, and deformation to failure at room temperature

It should be noted that in the Ti-Ni alloys the value of ε_{max} upon the martensite formation from austenite with a high concentration of lattice defects is reduced by about 10% as compared to the value of ε_{max} of quenched martensite [34, 35]. If this ratio is also valid for the Ti-Nb-Ta alloys, the retention of even a very large thermomechanical hardening upon PDA of these alloys will lead to only an insignificant difference in the ε_{max}. In addition, the calculations indicate that the theoretical reserve of reversible strain in the polycrystalline isotropic Ti-Nb-Ta alloy corresponds to 2.74 %, which is by 0.26% less than the maximum lattice strain of the single crystal (3%).

As to the Ti-Nb-Zr alloy, it was not possible to calculate the lattice parameters of the α" martensite because of the insufficient number of indexed lines.

Transmission Electron Microscopy

Electron micrographs of the structure of the Ti-21.2Nb-5.6Zr (TNZ2) alloy subjected to PDA at 450, 500, 550 and 600°C for 1 h after cold rolling with strains e = 0.28 and e = 2 are illustrated in Figure 2.7 and Figure 2.8.

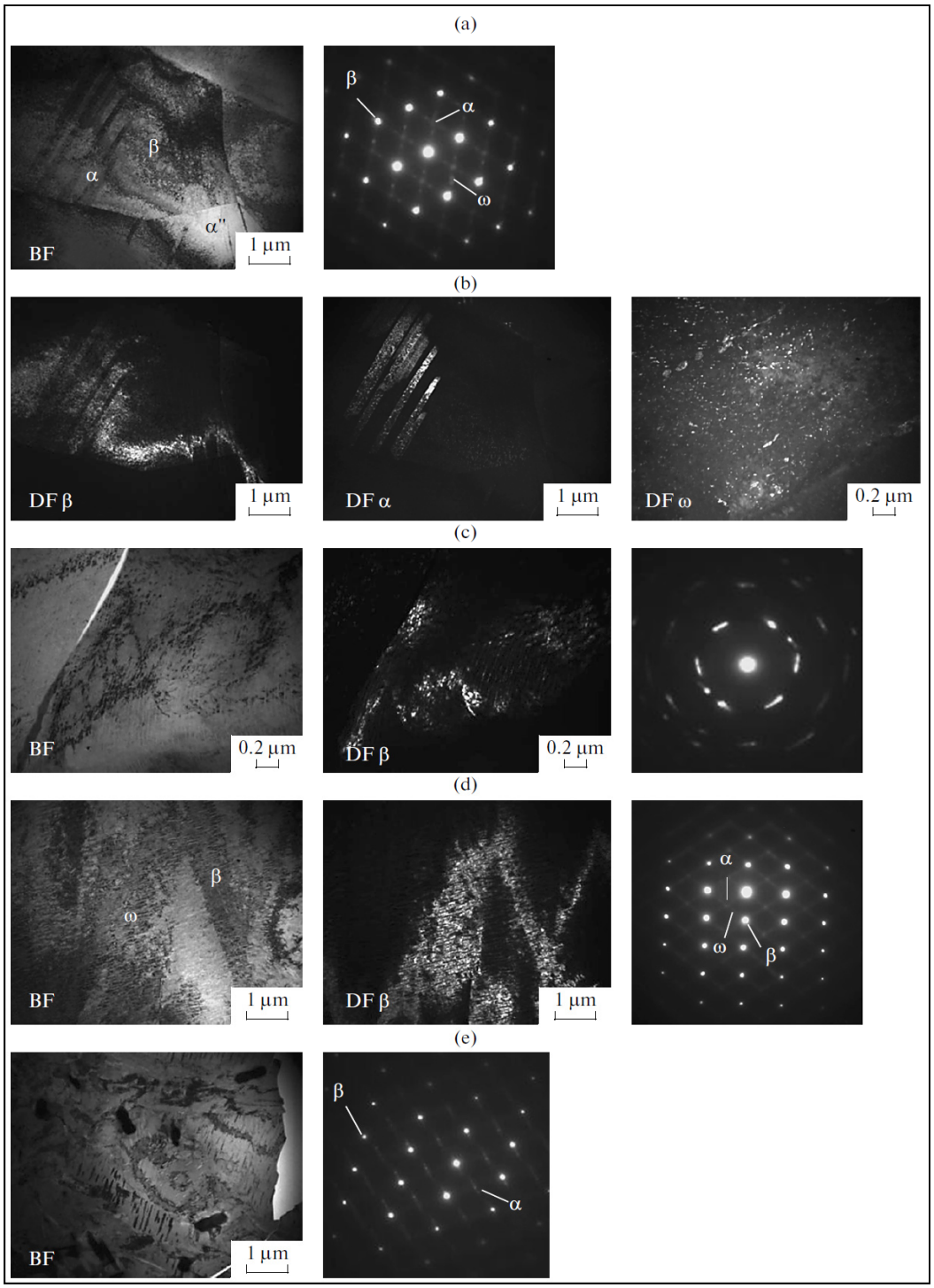

Figure 2.7 Structure of the Ti-21.2Nb-5.6Zr (TNZ2) alloy subjected to moderate cold deformation (e = 0.28) and postdeformation annealing (1 h) at the temperatures (a) 450, (b) 500, (c) 550, and (d) 600°C. Diffraction electron microscopy: (BF) bright-field images, (DF) dark-field images, and diffraction patterns

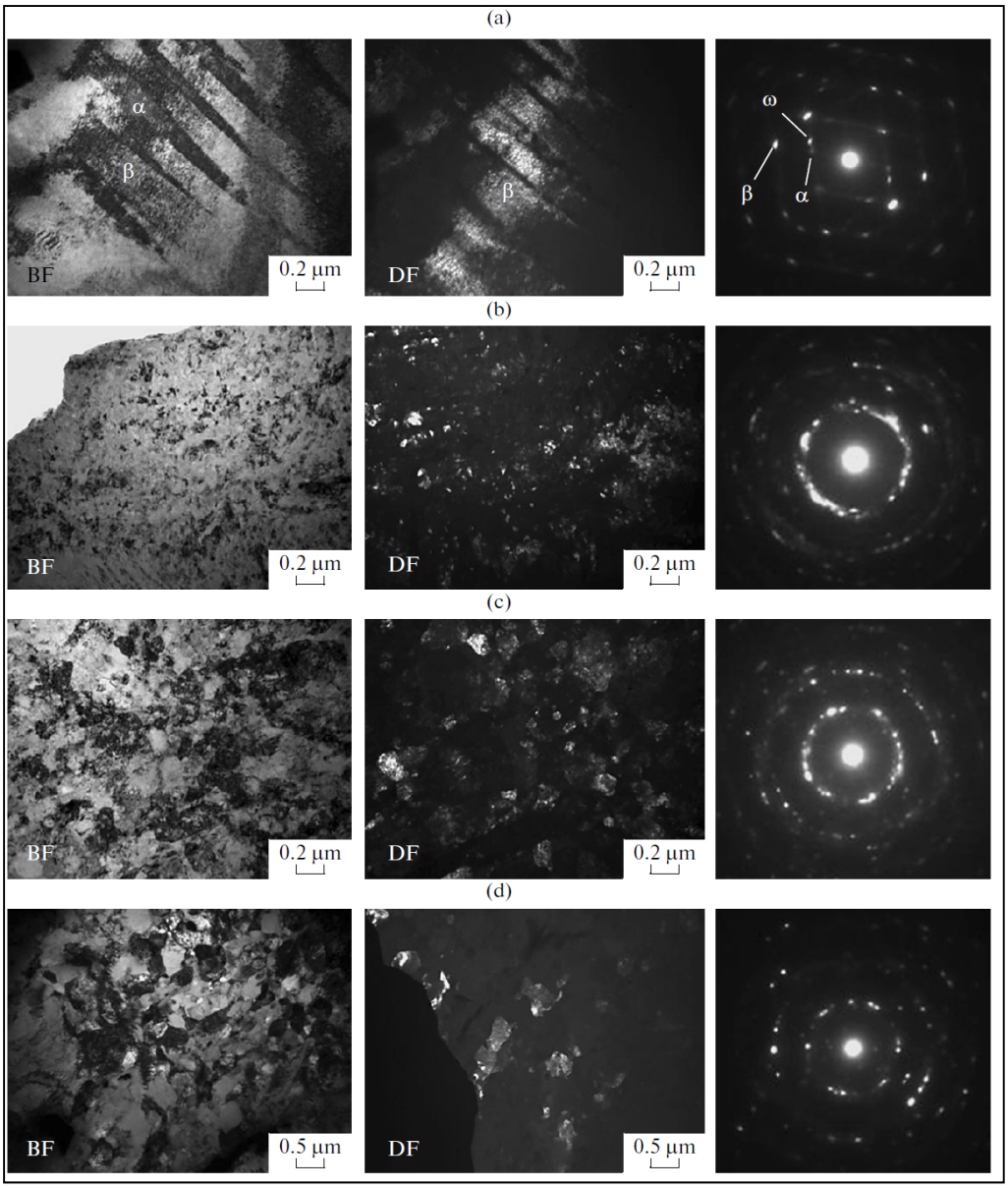

Figure 2.8 The structure of the Ti-21.2Nb-5.6Zr (TNZ2) alloy subjected to severe cold plastic deformation (e = 2) and postdeformation annealing at the temperatures (a) 450, (b) 500, (c) 550, and (d) 600°C. Diffraction electron microscopy: (BF) bright-field images, (DF) dark-field images of the β phase, and diffraction patterns

The Ti-Nb-Zr alloys are multiphase; they contain β-, α”-, α-, and ω phases, but the main phase is β. Of primary interest is the structure of the β phase, since it determines the peculiarities of the martensitic β → α” transformation underlying the shape-memory effect in

Ti-Ni-based alloys. Of course, one should keep in mind that the presence of the α- and ω phases in excessively large quantities reduces reversible strain.

A moderate cold deformation (e = 0.28) of the Ti-Nb-Zr alloy causes the formation of a developed dislocation substructure in the β-phase matrix and in the α(α")-phase plates; there are also seen deformation bands and the ω phase. After PDA at 450°C, there are no significant changes in the dislocation substructure of the β and α phases; a high density of dislocations is detected as before, the general view of the structure is preserved, but the ω-phase content increases (Figure 2.7a). Upon PDA at 500°C, after a moderate deformation (e = 0.28), a polygonized substructure is formed ("nanosubgrained," with subgrain sizes from 20 to 100 nm) (Figure 2.7b). When the PDA temperature rises to 550°C, the subgrains grow and reach the limits of the nanometer and submicron range (an average size of about 100 nm) (Figure 2.7c, where stitched precipitates of the ω phase are revealed against the background of β-phase subgrains); after PDA at 600°C for 1 h, their sizes increase to submicron one (200–500 nm) (Figure 2.7d). Judging from the small smearing of diffraction reflections of the β phase both after deformation and after PDA to 600°C, there are observed only low-angle misorientations on the selected areas. After PDA at 600°C for 1 h, in the structure there are also detected some recrystallized β-phase grains a few microns in size. After PDA at 750°C, there is already seen a recrystallized structure of the β phase (see Figure 2.1f, g). The α phase was found throughout the PDA temperature range from 450 to 600°C, while no ω-phase reflections were detected after PDA at 600°C in the diffraction pattern.

In the case of the initial severe deformation (e = 2) of the Ti-Nb-Zr alloy, a high density of dislocations is observed in the β- and α phases, and, apparently, a nanocrystalline structure (NCS) is locally generated, which is difficult to observe visually, and in the analyzed selected-area diffraction patterns no signs of an NCS were found. The amorphization of the structure in this case does not take place, in contrast to the Ti-Ni alloys. After PDA at 450°C, no substantial changes are revealed in the structure (Figure 2.8a). The PDA at 500°C after severe deformation generates a mixed nanosubgrained plus nanocrystalline structure; i.e., there is predominantly formed a polygonized nanosubgrained structure (NSS) of the β and α

phases, although there are also seen high-angle misorientations in the diffraction pattern (Figure 2.8b). The NCS grains could arise as a result of recrystallization in the NSS, although, after the PDA at 550°C (Figure 2.8c) and then at 600°C (Figure 2.8d) the structure does not change, only the size of grains and subgrains increases, and at 600°C exceeds the nanorange.

Effect of Structure on the Mechanical Properties of the Ti-Nb-(Zr, Ta) Alloys

The structures of the Ti-Nb-Ta and Ti-Nb-Zr alloys formed as a result of thermomechanical processing, as well as their behaviors during TMT, are close enough.

The alloys investigated were subjected to a thermomechanical treatment consisting of cold rolling and postdeformation annealing. Accordingly, the structure can be controlled by changing the TMT parameters, such as the degree of deformation and conditions of postdeformation annealing.

The structure investigation shows that the effect of the degree of strain (within the ranges studied) on the alloy structure is not as pronounced as that of the PDA temperature. Therefore, the dependences of the microhardness on the PDA temperature for different degrees of strain are close and appear to be similar upon the variation of the alloy composition (Figure 2.9a, b) [36].

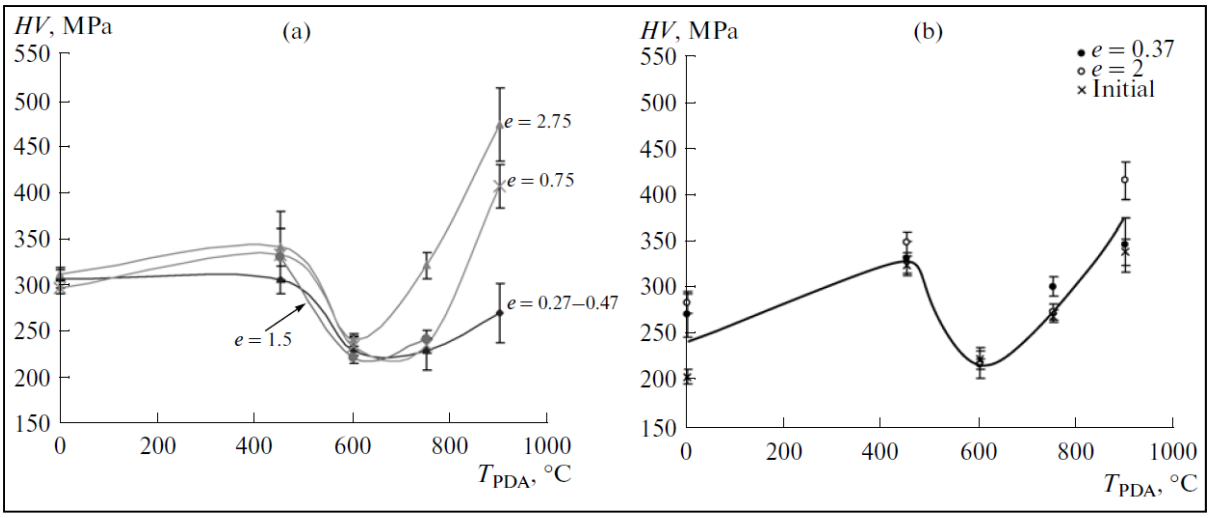

Figure 2.9 Hardness dependence on the PDA temperature of the alloys: (a) Ti-18.3Nb-5.1Zr (TNZ1); and (b) Ti-20.9Nb-5.7Zr (TNZ3)

It is known that the metallic materials used as implants should, in the ideal case, imitate the mechanical behavior of the bone tissue and, therefore, have a low Young's modulus and a nonlinear mechanical behavior with a hysteresis, that is, to show a superelasticity effect [1]. Let us consider how these properties are implemented on the example of the Ti-20.9Nb-5.7Zr (TNZ3) alloy after moderate plastic deformation (e = 0.37) and PDA.

As is seen from Figure 2.10, partial superelasticity appears in tensile tests of the Ti-Nb-Zr alloy at room temperature already in the first cycle of deformation by loading-unloading and, especially, after annealing, which results in the formation of polygonized substructure with submicron subgrains and fine recrystallized structure in the β phase (600 and 750°C). In the case of the Ti-Nb-Ta alloy, there is observed an analogous regularity in the change in the mechanical properties depending on the PDA temperature (Figure 2.11). In the TNZ3 alloy, the value of the reversible strain upon unloading (including superelastic and elastic deformation) after PDA at 600°C is 1.5% (at an induced deformation of 2.4%). The change in the diagram of deformation, i.e., the manifestation of partial superelasticity and the character of the variation of the yield stress with temperature of mechanical tests (see inset in Figure 2.10), indicates the occurrence of a martensitic transformation under stress. Note that the samples annealed at 450°C undergo fracture in a brittle manner, which is caused by the

combined effect of a strong total residual strain hardening and precipitation of the embrittling ω phase [6].

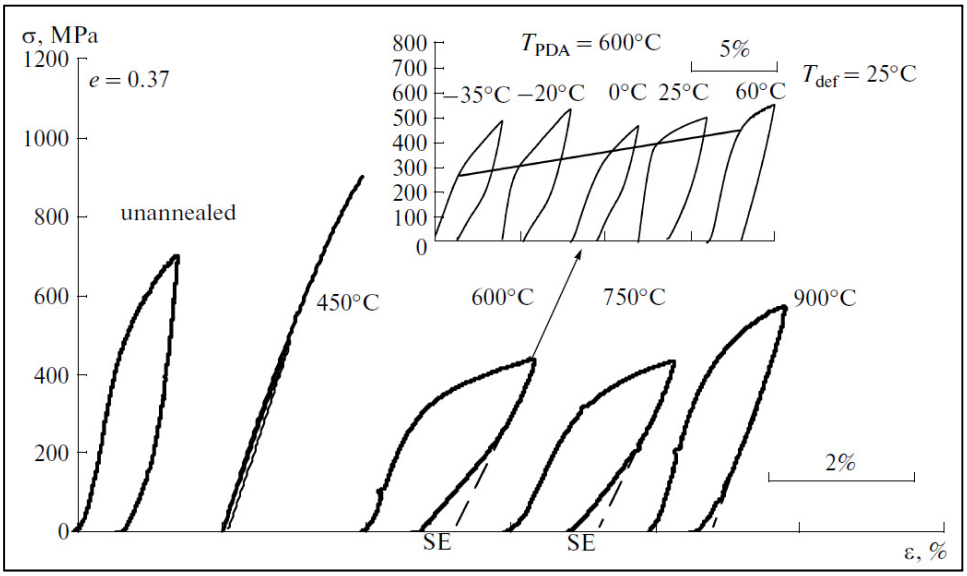

Figure 2.10 Loading-unloading deformation diagrams of the Ti-20.9Nb-5.7Zr (TNZ3) alloy annealed in the range from 450 to 900°C after moderate plastic deformation (e = 0.37). The inset shows the deformation diagrams of loading-unloading tests at various temperatures after *e* = 0.37 and PDA at 600°C

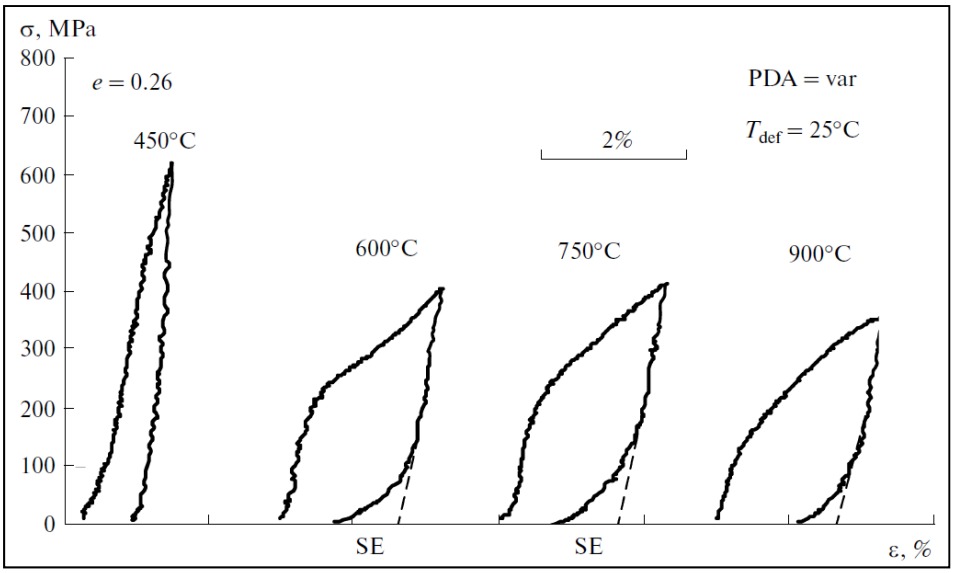

Figure 2.11 Deformation diagrams of loading-unloading of the Ti-19.5Nb-6.5Ta (TNT1) alloy annealed in the range from 450 to 900°C after moderate plastic deformation (e = 0.26)

Figure 2.12 compares the variation of the Young's modulus of the TNZ3 alloy found from the deformation diagrams shown in Figure 2.10 and of the microhardness (Figure 2.9b) depending on the PDA temperature. As is seen from Figure 2.12, both the microhardness and the Young's modulus exhibit a minimum in the range of PDA temperatures from 600 to 750°C.

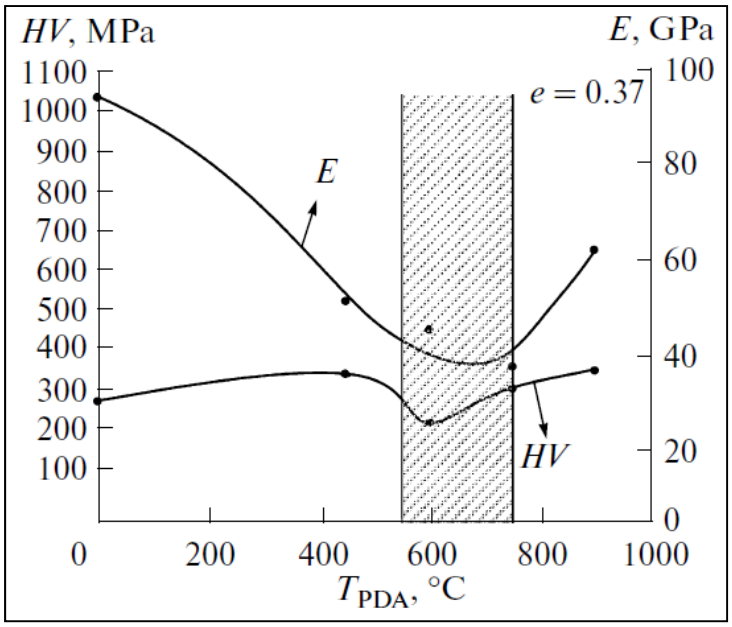

Figure 2.12 Variation of the microhardness and Young's modulus of the Ti-20.9Nb-5.7Zr (TNZ3) alloy depending on the PDA temperature. The initial strain *e* is 0.37.

The microhardness and the yield stress of SMAs are structure-sensitive properties, which depend on the size of grains and subgrains, dislocation density, sizes of precipitate and their location, on the phase composition, test temperature relative to the martensitic transformation temperature, etc. The decrease in the microhardness and Young's modulus near 600°C is primarily due to the depletion of the β phase of the third alloying element, Zr [37], and possibly of Nb, which favors the occurrence of the β → α" transformation upon loading and thus a decrease in the "phase" yield stress. As the annealing temperature increases to 600°C, the structure imperfection decreases (the width of the X-ray diffraction lines of the β phase decreases sharply, see Figure 2.4; polygonization develops; recrystallization starts, see Figure 2.7, Figure 2.8), which leads to a decrease in the contribution of strain hardening to the strengthening of the alloy. A further increase in the annealing temperature is accompanied by a strengthening of the β phase caused by the saturation of the sample with oxygen (oxygen embrittlement) [36] and by an increase in the concentrations of Zr and Nb in this phase. This causes a lowering of the M_s temperature and, hence, reduces the probability of the occurrence

of the β → α” transformation upon loading. In the case of annealing at temperatures close to 900°C, one should take into account strengthening caused by the saturation of the sample with oxygen (oxygen embrittlement) [36].

Thus, the range of PDA temperatures of the Ti-Nb-Ta and Ti-Nb-Zr alloys in which we can expect the maximum superelasticity lies in the vicinity of 600°C and corresponds to the formation of mainly polygonized substructure of the β phase with submicron structural elements (subgrains and grains).

2.6 Conclusions

(1) Moderate cold plastic deformation (e ≈ 0.3) of the Ti-Nb-Ta and Ti-Nb-Zr shape-memory alloys (SMAs) leads to the formation of a developed dislocation substructure in the β phase. With going to severe plastic deformation (e ≈ 2), along with the development of a dislocation substructure there can be observed local regions of a nanocrystalline structure; no amorphization of the structure occurs under these conditions, in contrast to the Ti-Ni SMAs. In the deformed alloys, there are also formed α”-, α-, ω phases in limited amounts.

(2) During postdeformation annealing at temperatures below 450°C, the structure of the β phase in the Ti-Nb-Zr SMAs varies only slightly. Above 450°C, there is mainly formed a polygonized substructure in the β phase, which is nanosubgrained at the annealing temperature of 500°C, transition to submicron at 550°C, and submicron at 600°C. In the case of the initial severe deformation (e = 2), within the whole range of annealing temperatures there are observed highangle misorientations of microstructure blocks. The recrystallization of the β phase in the Ti-Nb-Zr and Ti-Nb-Ta SMAs develops above 600°C. The ω phase is present up to 550°C.

(3) The lattice parameters of the deformation-induced α” martensite formed in the Ti-Nb-Ta alloy are independent of the PDA temperature in the range from 600 to 900°C, in which the β-phase transition from polygonized substructure to the recrystallized structure takes place.

The crystallographic reserve of reversible strain does not change in this process and is equal to ε_{max} = 3.0 ± 0.2% (the reserve of reversible strain in the isotropic-polycrystal approximation amounts to 2.7 ± 0.2%).

(4) From the regularities of the Young's modulus variation and from the loading-unloading deformation diagrams, it follows that the range of PDA temperatures that is most favorable for the manifestation of the effect of superelasticity in the Ti-Nb-Zr and Ti-Nb-Ta alloys lies near 600°C and corresponds to the formation of mainly polygonized substructure of the β phase with submicron-sized structural elements and a small amount of the ω phase.

2.7 Acknowledgments

This work was supported in part by the Ministry of Education and Science, Russian Federation, by the Natural Science and Engineering Research Council of Canada, and by the Program of Establishment and Development of the National Science and Technology University (MISiS).

2.8 References

1. J. R. Davis, Handbook of Materials for Medical Devices (ASM Int., Materials Park, Ohio, 2003).

2. V. E. Gyunter, V. I. Itin, L. A. Monasevich, et al., Shape Memory Effects and Their Application in Medicine, Ed. by L. A. Monasevich (Nauka, Novosibirsk, 1992) [in Russian].

3. J. Ryhänen, Biocompatibility Evaluation of Nickel-Titanium Shape Memory Alloy, Academic Dissertation, University of Oulu, 1999.

4. T. Yoneyama and S. Miyazaki, Shape Memory Alloys for Biomedical Applications (Woodhead, England, 2010).

5. K. Takamura, K. Hayashi, N. Ishinishi, T. Yamasda, and Y. Sugioka, “Evaluation of Carcinogenicity and Chronic Toxicity Associated with Orthopedic Implants in Mice,” J. Biomed. Mater. Res. 28, 583-589 (1980).

6. H. Y. Kim, Y. Ikehara, J. I. Kim, H. Hosoda, and S. Miyazaki, “Martensitic Transformation, Shape Memory Effect and Superelasticity of Ti-Nb Binary Alloys,” Acta Mater. 54, 2419-2429 (2006).

7. M. Morinaga, Y. Murata, and H. Yukawa, “Molecular Orbital Approach to Alloy Design,” in Applied Computational Materials Modeling: Theory, Simulation and Experiment, Ed. by G. Bozzolo, R.D. Noebe, and P. B. Abel (Springer, Berlin, 2007). pp. 255-306.

8. J. I. Kim, H. Y. Kim, T. Inamura, H. Hosoda, and S. Miyazaki, “Shape Memory Characteristics of Ti-22Nb-(2-8)Zr(at. %) Biomedical Alloys,” Mater. Sci.Eng., A 403, 334-339 (2005).

9. H. Y. Kim, T. Sasaki, K. Okutsu, J. I. Kim, T. Inamura, H. Hosoda and S. Miyazaki, “Texture and Shape Memory Behavior of Ti-22Nb-6Ta Alloy,” Acta Mater. 54, 423-433 (2006).

10. M. Long and H. J. Rack, “Titanium Alloys in Total Joint Replacement – A Materials Science Perspective,” Biomaterials 19, 1621-1639 (1998).

11. E. W. Collings, The Physical Metallurgy of Titanium Alloys (American Society for Metals, Metals Park, Ohio, 1984; Metallurgiya, Moscow, 1988).

12. S. G. Glazunov and V. N. Moiseev, Structural Titanium Alloys (Metallurgiya, Moscow, 1974) [in Russian].

13. M. I. Petrzhik and S. G. Fedotov, “Thermal Stability and Dynamics of Martensitic Structure in Ti-(Ta,Nb) Alloys,” in Proc. 16th Conf. on Applied Crystallography (World Sci., Singapore, 1995), pp. 273-276.

14. M. Abdel-Hady, K. Hinoshita, and M. Morinaga, “General Approach to Phase Stability and Elastic Properties of β-Type Ti-Alloys Using Electronic Parameters,” Scr. Mater. 55, 477-480 (2006).

15. M. Abdel-Hady, H. Fuwa, K. Hinoshita, H. Kimura, Y. Shinzato, and M. Morinaga, “Phase Stability Change with Zr Content in β-Type Ti-Nb Alloys,” Scr. Mater. 57, 1000-1003 (2007).

16. S. Miyazaki, K. Otsuka, and Y. Suzuki, “Transformation Pseudoelasticity and Deformation Behavior in Ti-50.6 at% Ni,” Scr. Metall 15, 287-292 (1981).

17. S. D. Prokoshkin, I. Yu. Khmelevskaya, V. Brailovski, F. Trochu, S. Turenne, and V. Yu. Turilina, “Thermomechanical Treatments and Their Influence on the Microstructure and Stress/Strain Diagrams of NiTi Shape Memory Alloys,” Can. Metall. Quart. 13 (1), 95-108 (2004).

18. S. D. Prokoshkin, I. Yu. Khmelevskaya, V. Brailovskii, F. Trochu, V. Yu. Turilina, and L. E. Inaekyan, “Effect of Low-Temperature Thermomechanical Treatment and Postdeformation Heatings on Structure and Properties of Titanium-Nickel Shape Memory Alloys,” in Proc. 38th Semin. “Actual Problems of Strength”, St. Petersburg, 2001, pp. 83-89.

19. V. Brailovski, I. Yu. Khmelevskaya, S. D. Prokoshkin, V. G. Pushin, E. P. Ryklina, and R. Z. Valiev, “Foundations of Heat and Thermomechanical Treatments and Their Effect on the Structure and Properties of Titanium Nickelide-Based Alloys,” Phys. Met. Metalogr. 97 (Suppl. 1), S3-S55 (2004).

20. S. D. Prokoshkin, V. Brailovskii, I. Yu. Khmelevskaya, S. V. Dobatkin, K. E. Inaekyan, V. Demers, and E. C. Tat'yanin, "Formation of Nanocrystalline Structure upon Severe Plastic Deformation by Rolling and Annealing and to Improve the Complex of Functional Properties of Ti-Ni Alloys," Izv. Ross. Akad. Nauk, Ser. Fiz. 70, 1344-1348 (2006).

21. V. Brailovski, S. D. Prokoshkin, I. Yu. Khmelevskaya, K. E. Inaekyan, V. Demers, S. V. Dobatkin, and E. V. Tatyanin, "Structure and Properties of the Ti-50.0 At% Ni Alloy after Strain Hardening and Nanocrystallizing Thermomechanical Processing," Mater. Trans. JIM 47, 795-804 (2006).

22. S. D. Prokoshkin, V. Brailovski, K. E. Inaekyan, V. Demers, I. Yu. Khmelevskaya, S. V. Dobatkin, and E. V. Tatyanin, "Structure and Properties of Severely Cold-Rolled and Annealed Ti-Ni Shape Memory Alloys," Mater. Sci. Eng., A 481-482, 114-118 (2008).

23. K. E. Inaekyan, S. D. Prokoshkin, V. Brailovski, I. Yu. Khmelevskaya, V. Demers, S. V. Dobatkin, E. V. Tatyanin, and E. Bastarache, "Substructure and Nanocrystalline Structure Effects in Thermomechanically Treated Ti-Ni Alloys," Mater. Sci. Forum 503-504, 597-602 (2006).

24. V. Brailovski, S. D. Prokoshkin, I. Yu. Khmelevskaya, K. E. Inaekyan, V. Demers, E. Bastarache, S. V. Dobatkin, and E. V. Tatyanin, "Interrelations between the Properties and Structure of Thermomechanically Treated Equiatomic Ti-Ni Alloy," Mater. Sci. Eng., A 438-440, 597-601 (2006).

25. S. D. Prokoshkin, V. Brailovskii, I. Yu. Khmelevskaya, S. V. Dobatkin, K. E. Inaekyan, V. Demers, V.Yu. Turilina, and E. V. Tat'yanin, "Formation of Substructure and Nanostructure upon Thermomechanical Treatment and Control of Functional Properties of Ti-Ni Shape Memory Alloys," Metalloved. Term. Obrab. Met., No. 5, 24-29 (2005).

26. K. Tsuchiya, M. Inuzuka, D. Tomus, A. Hosokawa, H. Nakayama, K. Morii, Y. Todaka, and M. Umemoto, “Martensitic Transformation in Nanostructured TiNi Shape Memory Alloy Formed via Severe Plastic Deformation,” Mater. Sci. Eng., A 438-440, 643-648 (2006).

27. H. Y. Kim, S. Hashimoto, J. I. Kim, T. Inamura, H. Hosoda, and S. Miyazaki, “Effect of Ta Addition on Shape Memory Behavior of Ti-22Nb Alloy,” Mater. Sci. Eng., A 417, 120-128 (2006).

28. S. D. Prokoshkin, V. Brailovskii, S. Tyurenn, I. Yu. Khmelevskaya, A. V. Korotitskii, and I. B. Trubitsyna, “On the Lattice Parameters of the B19' Martensite in Binary Ti-Ni Shape-Memory Alloys,” Phys. Met. Metallogr. 96, 55-64 (2003).

29. S. D. Prokoshkin, A. V. Korotitskiy, V. Brailovski, S. Turenne, I. Yu. Khmelevskaya, and I. B. Trubitsyna, “On the Lattice Parameters of Phases in Binary Ti-Ni Shape Memory Alloys,” Acta Mater. 52, 4479-4492 (2004).

30. Yu. S. Zhukova, M. I. Petrzhik, and S. D. Prokoshkin, “Estimation of Crystallographic Strain Limit during the Reversible β-α Martensitic Transformation in Titanium Shape Memory Alloys,” Russ. Metall. (Metally), No. 11, 1056-1063 (2010).

31. M. L. Bernshtein, L. M. Kaputkina, S. D. Prokoshkin, N. A. Nikishov, and A. V. Lyutsau, “Structure of Hot-Deformed Austenite and Its Change upon Storage after Deformation,” Fiz. Met. Metalloved. 42 (4), 804-813 (1976).

32. S. D. Prokoshkin, V. Brailovskii, A. V. Korotitskii, K. E. Inaekyan, and A. M. Glezer, “Specific Features of the Formation of the Microstructure of Titanium Nickelide upon Thermomechanical Treatment Including Cold Plastic Deformation to Degrees from Moderate to Severe,” Phys. Met. Metallogr. 110, 289-303 (2010).

33. K. Otsuka and C. M. Wayman, Shape Memory Materials (Cambridge Univ. Press, Cambridge, 1998).

34. S. Prokoshkin, A. Korotitskiy, V. Brailovski, and K. Inaekyan, "Effect of Dislocation Substructure and Grain Structure of B2-Austenite on Martensite Lattice Parameters and Transformation Lattice Strain in Binary Ti-Ni Alloys," in Proc. Int. Conf. SMST, Tsukuba, 2007 (ASM Int., Materils Park, Ohio, 2008), pp. 63-70.

35. S. D. Prokoshkin, A. V. Korotitskiy, V. Brailovski, K. E. Inaekyan, and S. M. Dubinskiy, "A Comparative Study of Martensite Crystal Lattice in Nanostructured, Quenched and Deformed Ti-Ni Shape Memory Alloys," in Proc. 8th Europ. Symp. on Martensitic Transformations, ESOMAT 2009 (EDP Science, Prague, 2009), pp. 1-7.

36. V. Brailovski, S. Prokoshkin, M. Gauthier, K. Inaekyan, S. M. Dubinskiy, M. Petrzhik, and M. Filonov, "Bulk and Porous Metastable Beta Ti-Nb-Zr(Ta) Alloys for Biomedical Applications," Mater. Sci. Eng., C 31, 643-657 (2011).

37. K. C. Hari Kumar, P. Wollants, and L. Delaey, "Thermodynamic Assessment of the Ti-Zr System and Calculation of the Nb-Ti-Zr Phase Diagram," J. Alloys Compd. 206, 121-127 (1994).

CHAPTER 3

ARTICLE #2:
STRUCTURE AND PROPERTIES OF Ti-19.7Nb-5.8Ta SHAPE MEMORY ALLOY SUBJECTED TO THERMOMECHANICAL PROCESSING INCLUDING AGING

3.1 Summary

This article is aimed at studying the influence of a thermomechanical treatment procedure consisting of cold rolling (e=0.37), post deformation annealing (400 – 750^{o}C, 1h) and ageing (300^{o}C, 10 min…3h) technological steps on the structure and functional properties of Ti-Nb-Ta SMA for biomedical applications. Transmission electron microscopy and X-ray diffraction analysis are used for evaluation of the structure. Microhardness measurements, single- and multi-cycle isothermal tensile testing, constant-strain temperature scanning and shape recovery testing are performed for evaluation of the mechanical and functional properties.

Post-deformation annealing in the 500 to 600^{o}C temperature range forms a nanosubgrained substructure, which transforms to a recrystallized structure of β-phase if the annealing temperature continues to increase. Simultaneously, annealing affects the phase composition and the β→α" transformation kinetics. After cold rolling and postdeformation annealing, Ti-Nb-Ta SMA manifests superelastic and shape memory behaviours. Ageing at 300^{o}C (1h) causes precipitation of ω-phase particles, which results in a significant improvement of the superelastic cyclic properties. However, ageing at 300^{o}C (3h) changes the ω-precipitates' particle morphology, which negatively affects the alloy's functional properties and cyclic stability. This article was published in the Journal of Materials Engineering and Performance, in 2013.

STRUCTURE AND PROPERTIES OF Ti-19.7Nb-5.8Ta SHAPE MEMORY ALLOY SUBJECTED TO THERMOMECHANICAL PROCESSING INCLUDING AGING

S. Dubinskiy[1,2], V. Brailovski[1], S. Prokoshkin[2], V. Pushin[3], K. Inaekyan[1], V. Sheremetyev[2], M. Petrzhik[2] and M. Filonov[2]

[1] École de technologie supérieure, 1100, Notre-Dame Street West, Montreal (Quebec), H3C 1K3, Canada

[2] National University of Science and Technology "MISIS", 4, Leninskiy prosp., Moscow 119049, Russian Federation

[3] Institute of the Metals Physics, Ural Branch of the Russian Academy of Sciences, 18, Sofia Kovalevskaya st., Ekaterinburg, 620990, Russian Federation

3.2 Abstract

In this work, ternary Ti-19.7Nb-5.8Ta (at.%) alloy for biomedical application was studied. The ingot was manufactured by vacuum arc melting with consumable electrode and then subjected to hot forging. Specimens were cut from the ingot and processed by cold rolling with e=0.37 of logarithmic thickness reduction and post-deformation annealing (PDA) between 400 and 750°C (1h). Selected samples were subjected to aging at 300°C (10 min…3h). The influence of the thermomechanical processing on the alloy's structure, phase composition, mechanical and functional properties was studied. It was shown that thermomechanical processing leads to the formation of a nanosubgrained structure (polygonized with subgrains below 100 nm) in the 500 to 600°C PDA range, which transforms to a recrystallized structure of β-phase when PDA temperature increases. Simultaneously, the phase composition and the β→α" transformation kinetics vary. It was found that after conventional cold-rolling and PDA, Ti-Nb-Ta alloy manifests superelastic and shape memory behaviors. During aging at 300°C (1h), an important quantity of randomly scattered equiaxed ω-precipitates forms, which results in improved superelastic cyclic properties. On the other hand, aging at 300°C (3h) changes the ω-precipitates' particle morphology from equiaxed to elongated and leads to their coarsening, which negatively affects the superelastic and shape memory functional properties of Ti-Nb-Ta alloy.

Keywords: biomaterials, titanium, rolling, heat treating, electron microscopy, mechanical testing.

3.3 Introduction

Ti-based alloys have been recognized for many years as excellent materials for biomedical implants mainly because of their low density, high corrosion resistance and biocompatibility combined with low Young's modulus [1]-[3]. Based on the formation of stable (α, α+β) and metastable (β) phases in these alloys, a wide variety of mechanical properties mimicking those of biological tissues (ex. superelasticity) can be obtained. This is the main reason behind significant interest to novel titanium metastable alloys containing exclusively biocompatible elements, such as Nb, Ta, Zr or Mo [4], [5]. Given that tantalum and niobium are considered as the strongest beta-stabilizing biocompatible metals, ternary or quarternary Ti-Nb-based shape memory alloys are being widely studied [6]-[8]. The structure and properties of these alloys depend on a complex sequence of phase transformations, which are influenced by thermomechanical processing conditions, such as severity of plastic deformation, post-deformation annealing temperature and cooling rate [9], [10]. In this work, Ti-19.7Nb-5.8Ta (at.%) shape memory alloy samples subjected to thermomechanical processing including cold rolling (CR), post-deformation annealing (PDA) and aging (AG) are characterized by TEM and X-ray diffraction techniques, microhardness, single- and multi-cycle isothermal tensile testing, and strain/stress recovery measurement techniques.

3.4 Experimental procedure

Casting

Ti-Nb-Ta ingots were cast by vacuum arc-melting with consumable electrode in a “VDP-0.02” furnace. The electrode was made from bars of pure Ti and Nb-Ta masteralloy. Hot forging of the 7 kg, 80 mm diameter ingot was carried out at 900 – 950^{o}C in air. As a result, the 51 mm diameter cylinder was obtained. The surface layer of the cylinder was removed by machining the cylinder to 50 mm diameter. A chemical analysis performed after this

treatment across the cylinder cross-section showed that the impurities content (including oxygen) corresponded to grade 1, ASTM F67-00 (see Table 3.1). For subsequent study, the ingot was cut into 8 mm thick disks, and then into 2 mm thick 30-50 mm long plates. Based on the data of Table 3.1, the M_s temperature was estimated as being close to $+50^oC$ [7].

Table 3.1 Ti-Nb-Ta ingot composition

Element	**wt%**	**at%**
Ti	55.4	74.5
Nb	28.4	19.7
Ta	16.2	5.8
O	0.039±0.008	-
N	0.0075±0.0021	-
H	0.00556±0.00087	-
C	0.009±0.002	-

Thermomechanical processing

After four-pass cold rolling to logarithmic thickness reduction of e=0.37, Ti-Nb-Ta plates were EDM-cut to form 1x1.5x50 (mm) specimens and subjected to post-deformation annealing (PDA) at 400, 450, 500, 550, 600, 650, 700 and 750°C (all 1h) followed by water-quenching to room temperature (RT). After PDA at 500°C (1h), aging at 300°C for various times (10 min, 30 min, 1h and 3h) was performed to estimate the effect of ω-phase precipitation on the functional properties of the studied alloy.

Experimental methods

The effect of thermomechanical processing on the microstructureand functional (shape memory) properties of Ti-Nb-Ta alloy was studied using the following TEM and X-ray diffraction analyses, mechanical and thermomechanical testing routines.

•**TEM analysis** of selected samples subjected to CR (e=0.37) + PDA (500, 600, 650 and 750^{o}C, all 1 h) and CR (e=0.37) + PDA (T=500^{o}C, 1h) + aging at 300^{o}C (1h and 3h) was carried out using "JEOL 2100CX" transmission electron microscope. Thin foils for TEM were prepared from 0.1 mm-thick platelets by electropolishing at -38 °C using 15% HNO_3 spirit solution and "TENUPOL-5" equipment (Struers, Denmark).

•**X-ray diffraction phase analysis** of selected samples subjected to CR (e=0.37) + PDA (500, 600 and 750°C, all 1h) and CR (e=0.37) + PDA (T=500°C, 1h) + aging at 300°C (1h and 3h) was performed using an "Ultima IV Rigaku"diffractometer (monochromatic CuK_{α}-radiation). The samples for X-ray analysis were mechanically polished and chemically etched using an acid solution of the following composition: $2HF:1HNO_3:17H_2O$.

•**Microhardness measurements** were performed using an "INSTRON Wilson Tukon2100" (500 g, 10 sec); five HV measurements were performed for each thermomechanical processing condition, and mean and standard deviation values were calculated.

•**Single- and multi-cycle isothermal tensile testing** was carried out at RT and at 40°C using an"MTS MiniBionix". Single-cycle testing consisted of loading up to 2% of strain and then unloading down to zero load with strain rate of 0.002 s^{-1}. During multi-cycle testing, a constant strain of ε_t=2% was applied in each cycle to specimen failure. The number of cycles to failure was measured, and the characteristic features of a superelastic loop, such as transformation yield stress $\sigma_{tr}^{A\rightarrow M}$, Young' modulus and accumulated strain were identified.

•**Constant-strain temperature scanning** was performed on selected samples using a LAMSI tensile testing bench. The samples subjected to CR (e=0.37) + PDA (T=450, 500, 600 and 700°C, all 1h) and CR (e=0.37) + PDA (T=500°C, 1h) + AG at 300°C (1h and 3h) were cooled down to -150°C, then stretched to a 2.5% strain, fixed, heated up to 200°C and cooled back to -150°C. The recovery stress generation-relaxation diagrams during heating and cooling were plotted.

•**Shape recovery testing** was carried out on selected samples after e=0.37 and PDA (T=450, 500, 600, 700°C, 1h) as well as after CR (e=0.37) + PDA (T=500°C, 1h) + AG at 300°C (1h and 3h). The samples were bent at -196°C around cylindrical mandrels of different radii, and heated up by hot air to a complete shape recovery. The shape memory (SM) recovery strain ε_r was measured as a function of initial (induced) strain ε_i, and maximum completely SM-recoverable strain $\varepsilon_{r,1}^{max}$ was then determined with 0.15% tolerance.

3.5 Results

Structure of thermomechanically treated Ti-Nb-Ta alloy

As seen in Figure 3.1a, the main phase in Ti-Nb-Ta alloy after conventional cold rolling is β-phase, whereas α", ω and possibly α phases are present in small quantities. Parallel electron microscopy study shows that the β-phase contains high dislocation density. Post-deformation annealing initiates recovery, polygonization and recrystallization processes in β-phase, which is confirmed by the continuous narrowing of the β-phase X-ray lines as PDA temperature increasesup to 750^{o}C (Figure 3.1b, c). This phase composition at RT does not change significantly after PDA at 500^{o}C, however, the α"-phase content is distinctly higher than that of ω- and α-phases (the presence of the latter is not evident) (Figure 3.1b). PDA at 750^{o}C reveals the presence of additional α"- and α -phases and absence of ω-phase (Figure 3.1c).

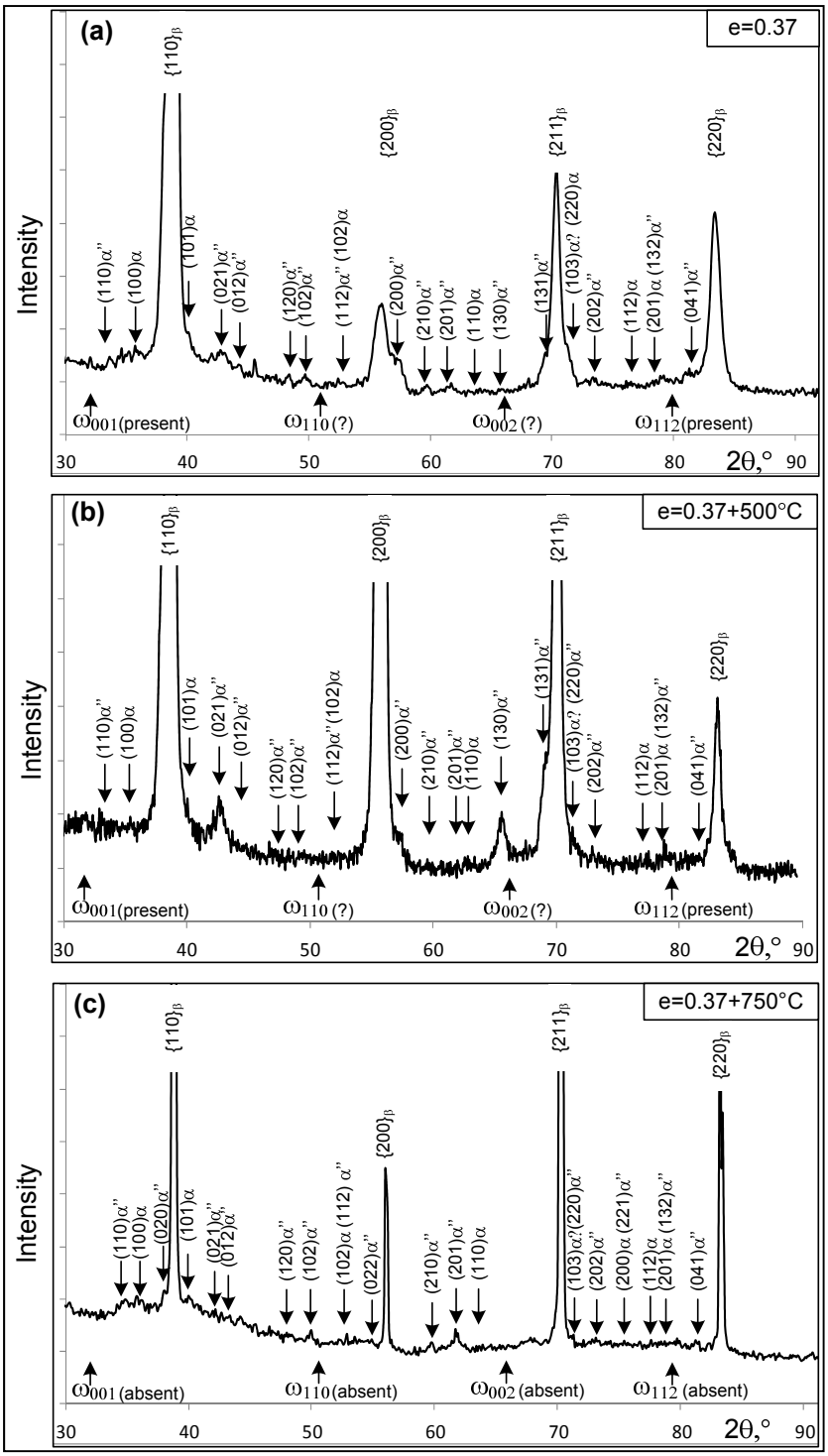

Figure 3.1 X-ray diffractograms of Ti-Nb-Ta alloy subjected to CR e=0.37 (a), e=0.37+PDA (T=500°C, 1h) (b), and e=0.37+PDA (T=750°C, 1h) (c); ↑ - expected locations of ω-phase X-ray lines

A TEM study after PDA at 500 and 600°C reveals a nanosubgrained (NS) dislocation substructure of β-phase (subgrain size below 100 nm) with "imposed" α"-martensite crystals (Figure 3.2a, b). The α"-martensite manifests a typical packet-like morphology of pairly-twinned martensite crystals. The α" crystals inherit the NS structure from the β-phase. Note that a significant α"-martensite quantity at RT may be partially caused by additional α" formation during low-temperature electropolishing of thin foils. Increasing the PDA temperature above 600°C leads to β-phase recrystallization, and PDA at 750°C results in β-phase grain growth up to 20-30 μm with some quantity of α- and α"-phases but without ω-phase (Figure 3.1c).

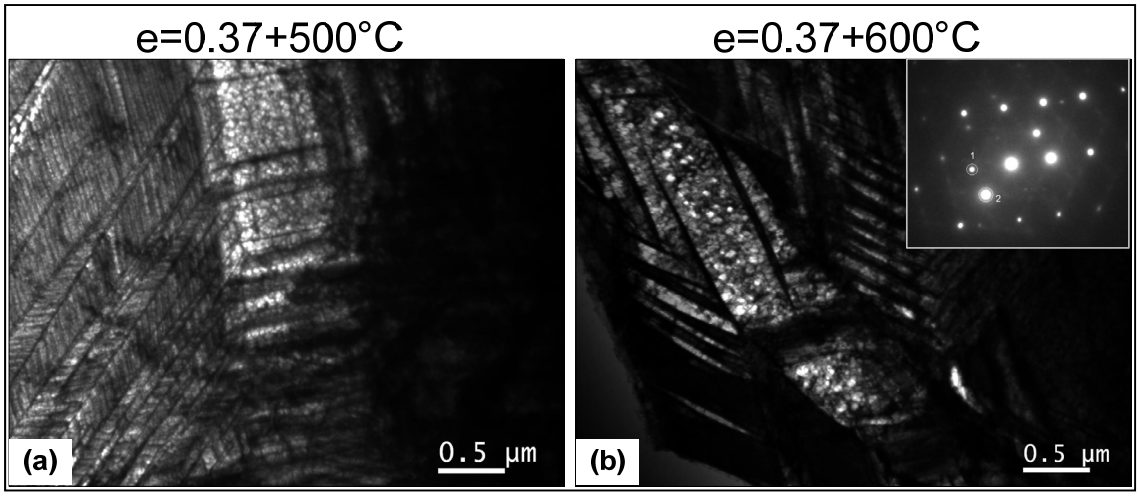

Figure 3.2 Structure of Ti-Nb-Ta alloy subjected to CR (e=0.37)+PDA (T=500 (a) and 600°C (b); 1h); a – bright field image, b – dark field image in a β-phase matrix reflection and SAED pattern (<110>$_\beta$ zone axis with two high-angle misorientations)

Even though X-ray diffraction analysis of the aged after 500°C-PDA samples (300°C, 10 min…3h) does not point to significant variations in the phase composition, TEM makes it possible to reveal the following changes in the ω-phase structure. After 300°C (1h)-aging, very fine (d=5-10 nm) randomly scattered equiaxed ω-phase particles manifest a weak tendency to form elongated rows, as shown on the dark-field image (Figure 3.3a) obtained from a group of very weak ω diffuse reflections in positions close to "1/3"<112>$_\beta$ and "2/3"<111>$_\beta$ (Figure 3.3b). After 300°C (3h)-aging, the system of ω-reflections becomes

more distinct (Figure 3.3d), and the tendency to form elongated rows of coarsened ω particles is enhanced (Figure 3.3c). This morphology cannot be attributed to α-phase crystals because α-phase reflections are absent in the corresponding SAED pattern (Figure 3.3d).

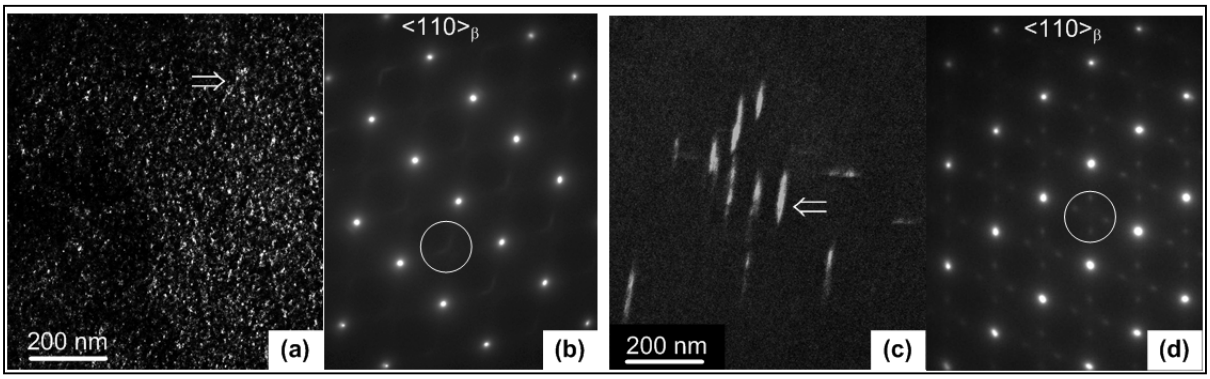

Figure 3.3 Dark-field image in ω-phase reflections of Ti-Nb-Ta alloy after CR (e=0.37)+PDA (T=500°C,1h)+AG(T=300°C, 1h (a) and 3h (c)), and corresponding SAED pattern, <110>$_\beta$ zone axis (b, d). Doubled arrow indicates an elongated row of ω particles

Table 3.2 resumes the correlation between the thermomechanical treatment and microstructure of Ti-Nb-Ta alloy.

Table 3.2 Phase constituents and other microstructural features resulted from TMTs

PDA and AG after CR e=0.3	**Structure of β-phase**	**Other phases in presence**
PDA 500°C (1h) and 600°C (1h)	Nanosubgrained (NS) dislocation substructure with subgrain size less than 100 nm	α”-martensite with typical packet-like morphology of pairly-twinned martensite crystals; α” crystals inherit the β-phase NS substructure; ω-phase is identified only by TEM.
PDA 750°C (1h)	Recrystallized structure with grain size of about 20-30 μm	Some quantity of α”- and α-phases but without ω-phase; α” crystals inherit the β-phase NS substructure.
PDA 500°C (1h) + AG 300°C (1h)	Nanosubgrained (NS) dislocation substructure with subgrain size less than 100 nm	Very fine (d=5-10 nm) randomly scattered equiaxed ω-phase particles
PDA 500°C (1h) + AG 300°C (3h)		ω-reflections system becomes more distinct; formation of elongated rows (up to 100-150 nm long – 30 nm wide) of coarsened (d=20-30 nm) ω-phase particles

Microhardness and single-cycle tensile testing

The results of RT microhardness and tensile testing of Ti-Nb-Ta alloy are presented in Figure 3.4 and Figure 3.5. As confirmed by microhardness measurements and stress-strain diagrams (Figure 3.4), Ti-Nb-Ta alloy subjected to conventional cold-rolling manifests a net softening after PDA at 500-550^{o}C (1h). The shape of loading-unloading diagrams after PDA in that temperature range is typical for shape memory behavior with a certain contribution of superelasticity [11]. In contrast, stress-strain diagrams after PDA at 400-450 and 600^{o}C manifest preferentially superelastic behavior. Furthermore, additional aging at 300^{o}C after PDA at 500^{o}C (1h) leads to appreciable changes in mechanical behavior: the greater the

aging time, the higher the alloy strengthening, and the closer the alloy's behavior comes to perfect superelasticity; the latter is valid up to a certain limit, the best fit corresponding to 1h-aging (Figure 3.5). To sum up these results, Figure 3.6 illustrates the evolution of Young's modulus (E) and transformation yield stress (σ_{tr}) as a function of the annealing temperature and aging time.

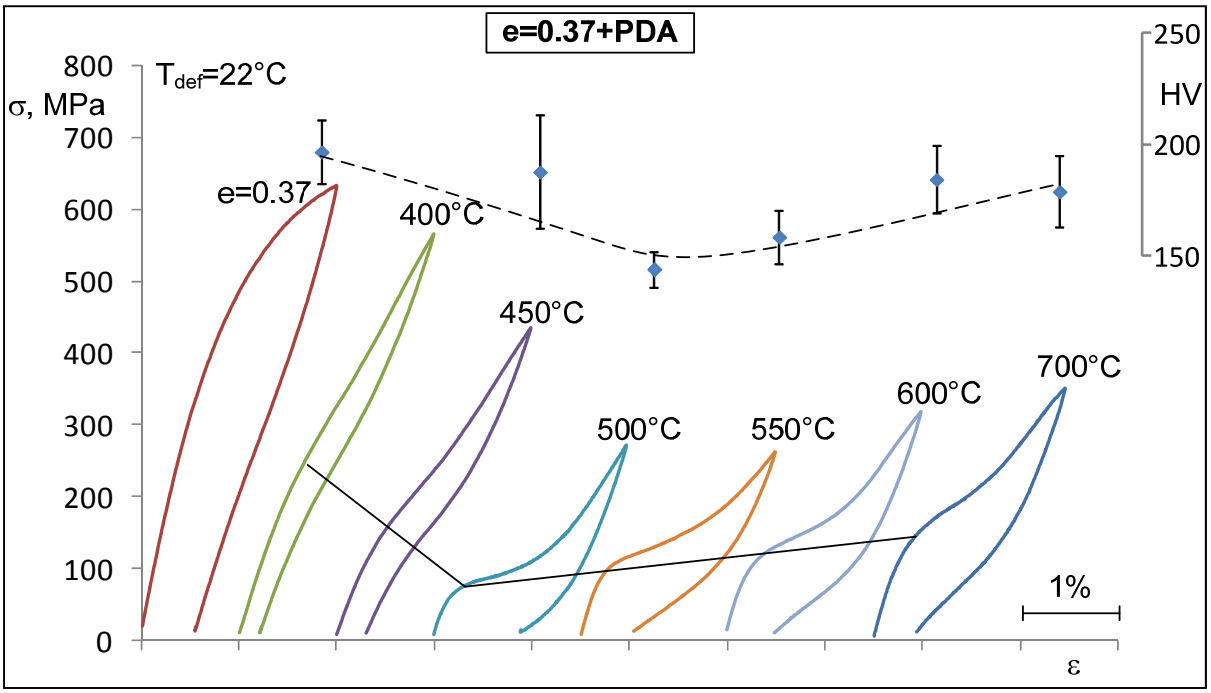

Figure 3.4 Microhardness Vickers measurements and stress-strain diagrams of Ti-Nb-Ta alloy subjected to CR (e=0.37)+PDA (1h) at different temperatures

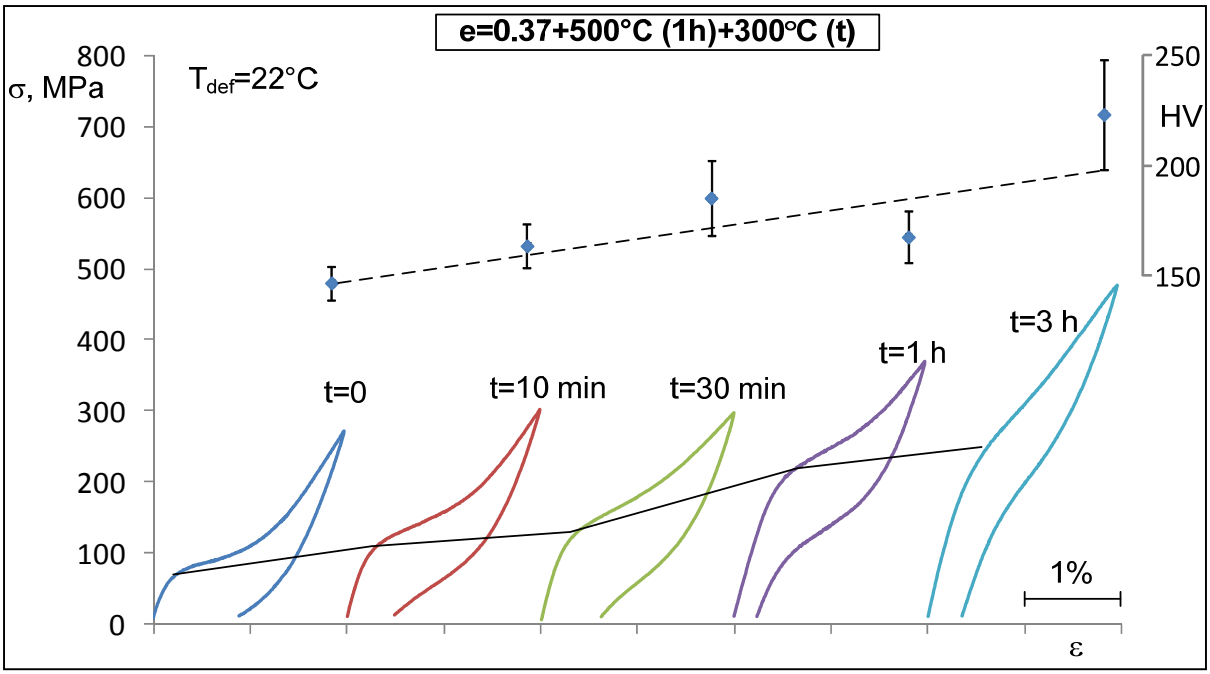

Figure 3.5 Microhardness Vickers measurements and stress-strain diagrams of Ti-Nb-Ta alloy subjected to CR (e=0.37) + PDA (T=500°C, 1h) + AG at 300°C with different aging times (t)

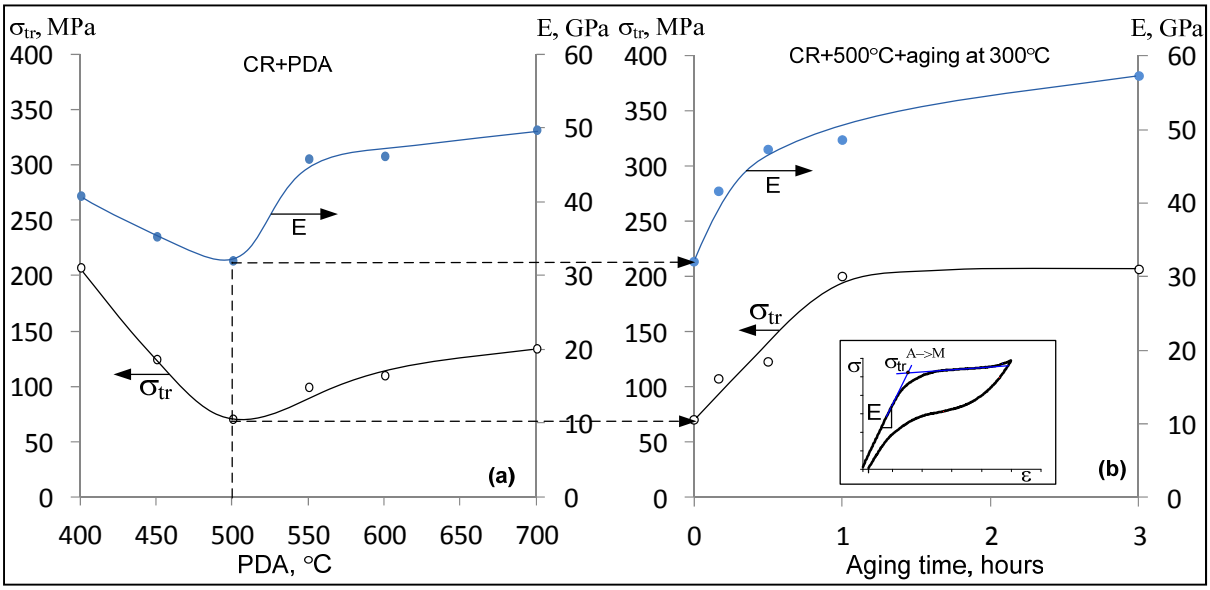

Figure 3.6 Transformation yield stress (σ_{tr}) and Young's modulus of Ti-Nb-Ta alloy subjected to (a) e=0.37+PDA (1h) at different temperatures, and (b) e=0.37+PDA (T=500°C, 1h) + AG (300°C, 10 min…3h). Insert: schematic presentation of the transformation yield stress and Young's modulus measurements

Multi-cycle tensile testing

In Figure 3.7, multi-cycle stress-strain diagrams obtained after different processing routes are collected. A distinct cyclic behavior close to linear superelasticity is observed for low-temperature annealing: 400 and 450^{o}C (Figure 3.7b, c). The accumulated strain to failure in these cases is the lowest – below 3% – as compared to 6.5% after annealing at 700^{o}C (Figure 3.7g). After aging at 300^{o}C of the sample annealed at 500^{o}C, simultaneous improvement of superelastic behavior and cyclic life is observed, the maximum corresponds to 1h aging time (Figure 3.7h-j).

Comparative tensile cycling at RT and at 40^{o}C was performed using the specimens subjected to annealing at 600^{o}C, 1h (Figure 3.8). It can be observed that, according to the Clausius-Clapeyron relationship, the higher the testing temperature, the higher the transformation yield stress: $\Delta\sigma/\Delta T \approx 2.5 \pm 1.0$MPa/^{o}C. This transformation yield stress–temperature slope value is close to those observed for similar alloys in [7], [12]. That supports the assertion that we truly deal with stress-induced thermoelastic martensitic transformation.

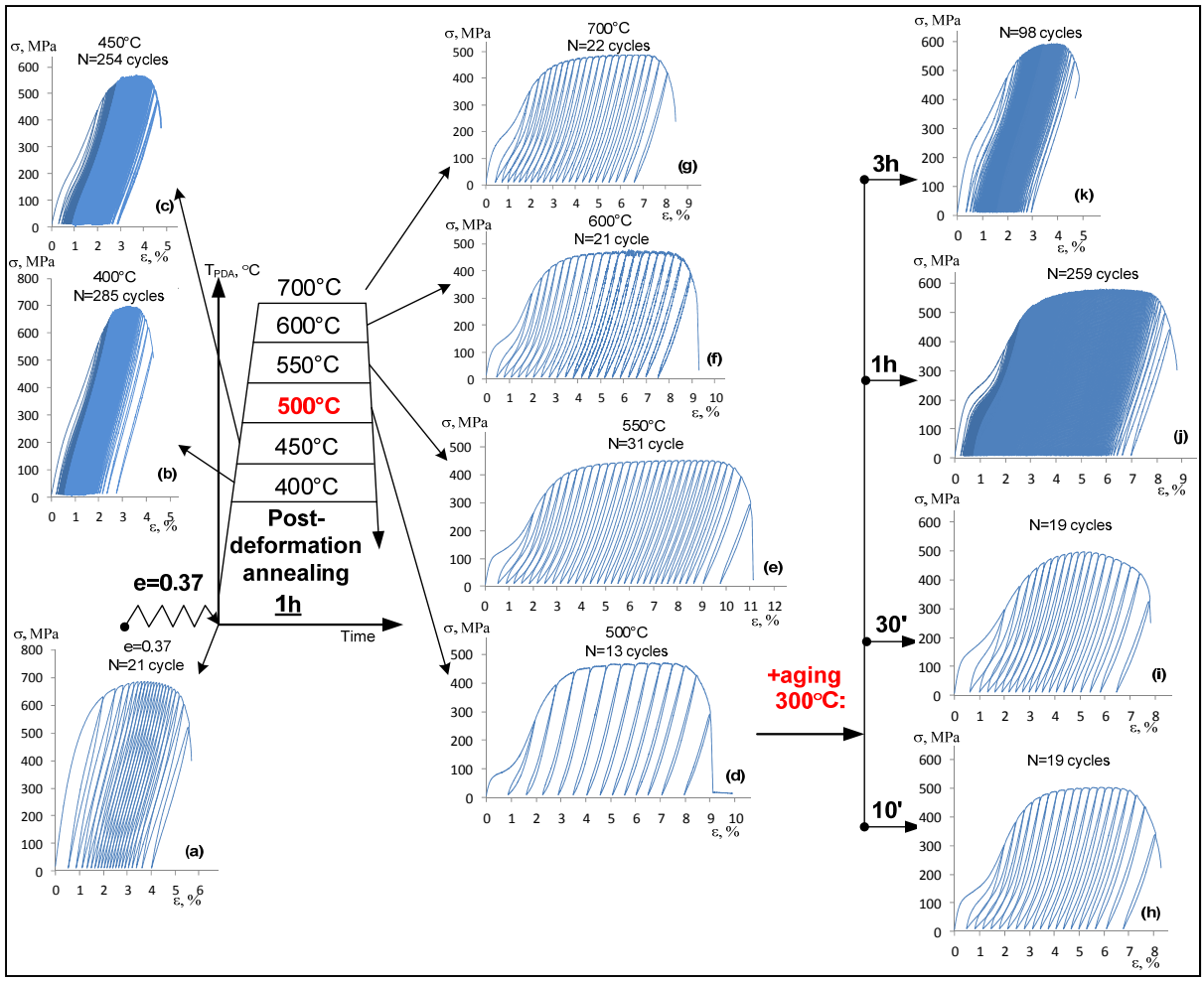

Figure 3.7 Stress-strain cycling diagrams of Ti-Nb-Ta alloys after e=0.37+PDA: (a) as-deformed, e=0.37; deformed and annealed at 400 (b); 450 (c); 500 (d); 550 (e); 600 (f) and 700°C (g) (all 1h). Aged at 300°C after e=0.37+500°C (1h): 10 min (h); 30 min (i); 1h (j) and 3h (k)

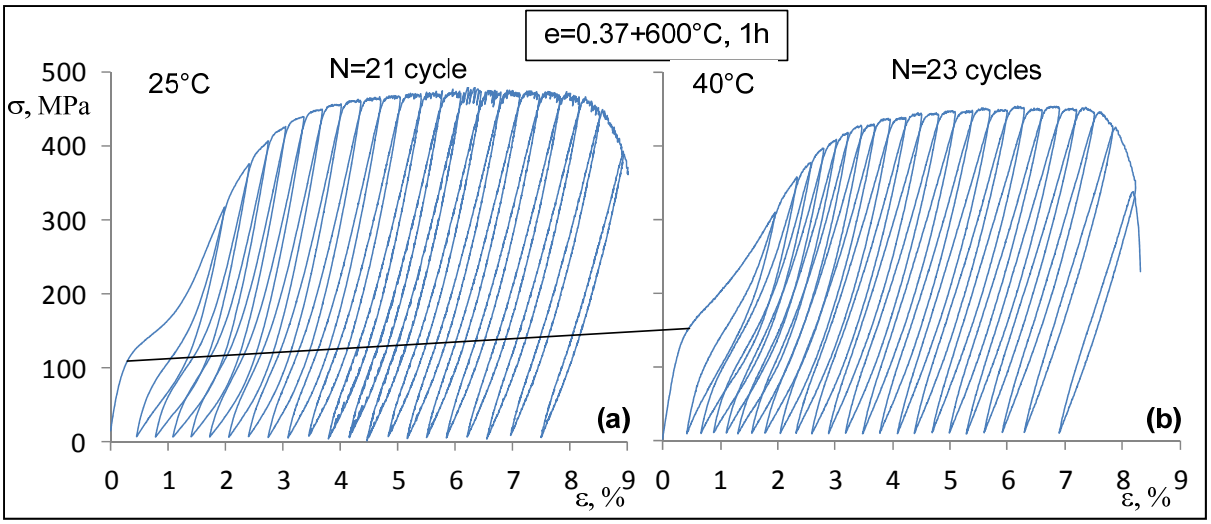

Figure 3.8 Cycling stress-strain diagrams of Ti-Nb-Ta alloys after e=0.37+600°C at (a) 25°C and (b) 40°C

Thermomechanical testing

Recovery stress testing

The results of the constant-strain temperature scanning experiment presented in Figure 3.9a illustrate the influence of the PDA temperature on the recovery stress generation and therefore on the reverse martensitic transformation temperature range under stress. The maximum recovery stresses $\sigma_r^{max} = \sigma^{Af\sigma} - \sigma^{As\sigma}$ correspond to annealing at 600 and 500°C and are equal to 80 and 50 MPa respectively. The effect of the PDA temperature on the characteristic stresses of the generation-relaxation curves, $\sigma^{Af\sigma}$, $\sigma^{As\sigma}$ (Figure 3.10a) is similar to the evolution of the transformation yield stress and Young's modulus shown in Figure 3.6a. The initial lowering of stress upon heating is due to thermal dilatation of the specimen followed by recovery stress generation caused by constrained α"→β martensitic transformation.

Stress-temperature diagrams of the samples subjected to aging at 300°C (1h and 3h) after CR+500°C (1h) reflect a certain evolution in material microstructure (Figure 3.9b) as

compared to the non-aged specimens (Figure 3.9a). After 1h-aging, the stress-temperature diagram shows a distinct stress generation, whereas 3h-aging suppresses the martensitic transformation and, therefore, stress generation becomes very weak (Figure 3.9b, Figure 3.10b).

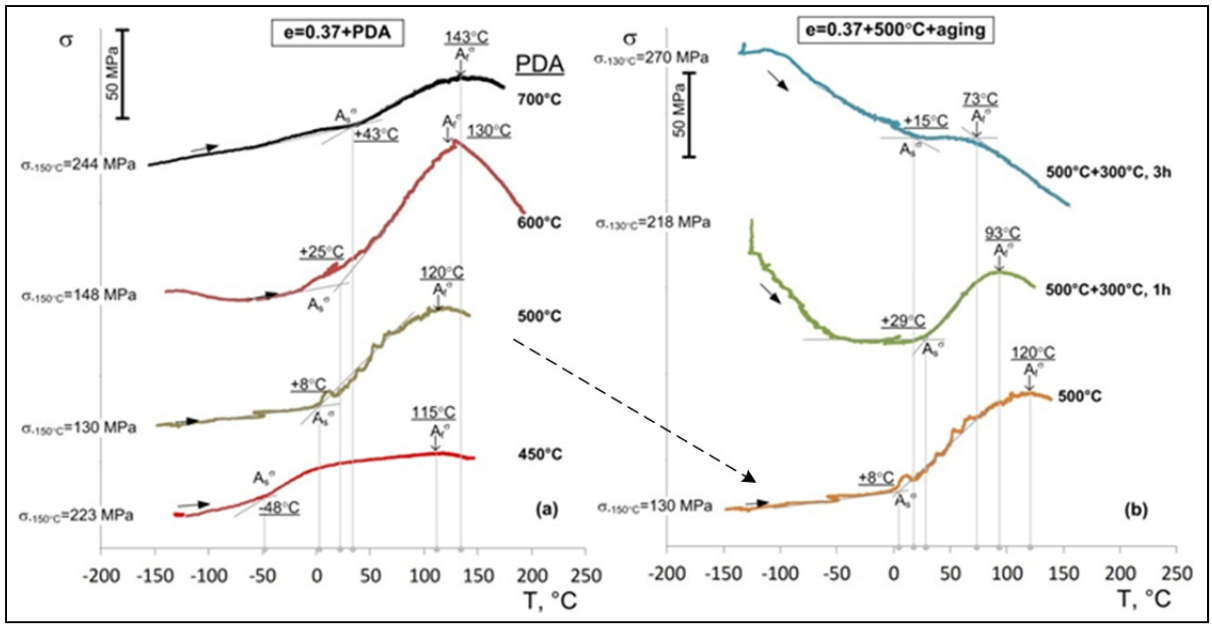

Figure 3.9 Constant-strain temperature scanning diagrams for 2.5% strain for Ti-Nb-Ta subjected to e=0.37+PDA (T=450, 500, 600 and 700°C) (a) and e=0.37+500°C (1h) + aging at 300°C (1 and 3 h) (b)

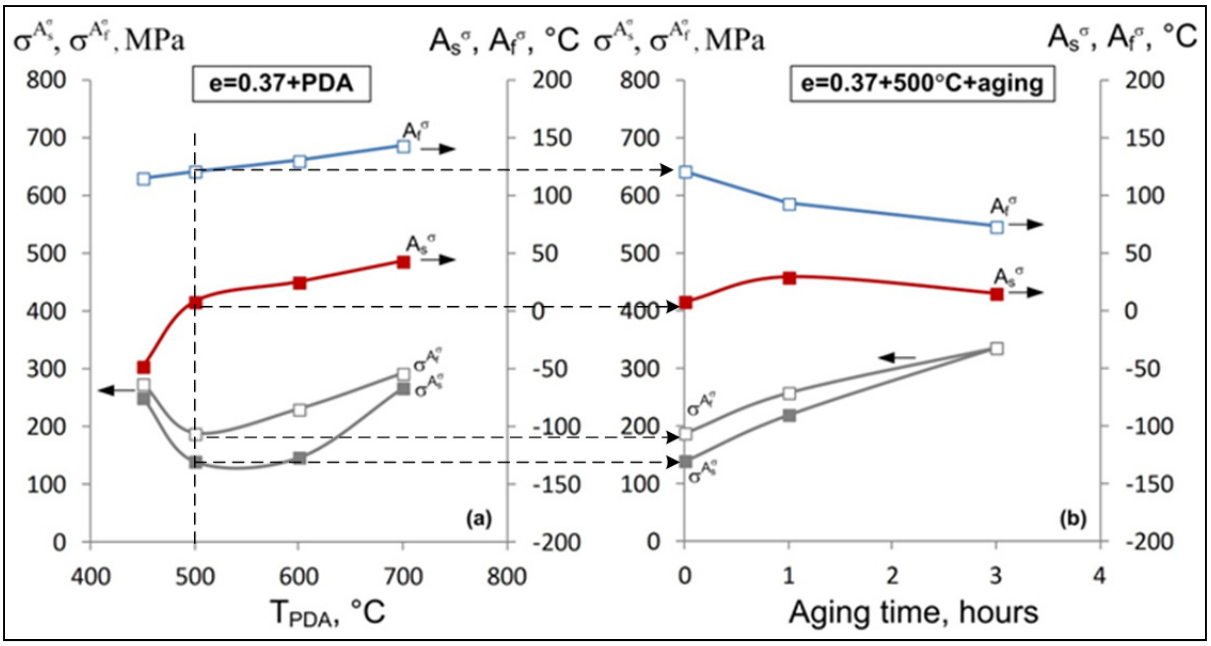

Figure 3.10 Variation of the reverse martensitic transformation temperatures and characteristic stresses for Ti-Nb-Ta subjected to e=0.37+PDA (a) and e=0.37+500°C (1h) + aging at 300°C (1 and 3 h) (b)

Recovery strain testing

For Ti-19.7Nb-5.8Ta alloy, completely recoverable shape memory strain in bending after stress-free heating from -196°C ($\varepsilon_{r,1}^{max}$) reaches its maxima of about 1.5-2% after annealing in the 500-700°C range and about 1% after 400-450°C annealing (Figure 3.11a). Aging at 300°C after e=0.37+PDA (T=500°C,1h) (Figure 3.11b) results in a net decrease ($\varepsilon_{r,1}^{max}$ under 1%) in shape restoration upon heating.

Figure 3.11 presents the recovery strain of shape memory effect (SME) only. This experiment was realized in three consecutive steps: deformation at low temperature, unloading at low temperature and heating. Induced strain was measured after unloading at -196°C, thus elastic + superelastic recovery strains were excluded from consideration. Recovery strain due to shape memory effect (SME) was measured upon heating. Intensive precipitation hardening during aging was accompanied by an increase in the alloy's true and transformation yield stresses. Thus, to induce SME, it was necessary to apply higher stresses

close to the alloy's true yield stress, which leaded to accumulation of residual strain and, therefore to decrease in recoverable strain.

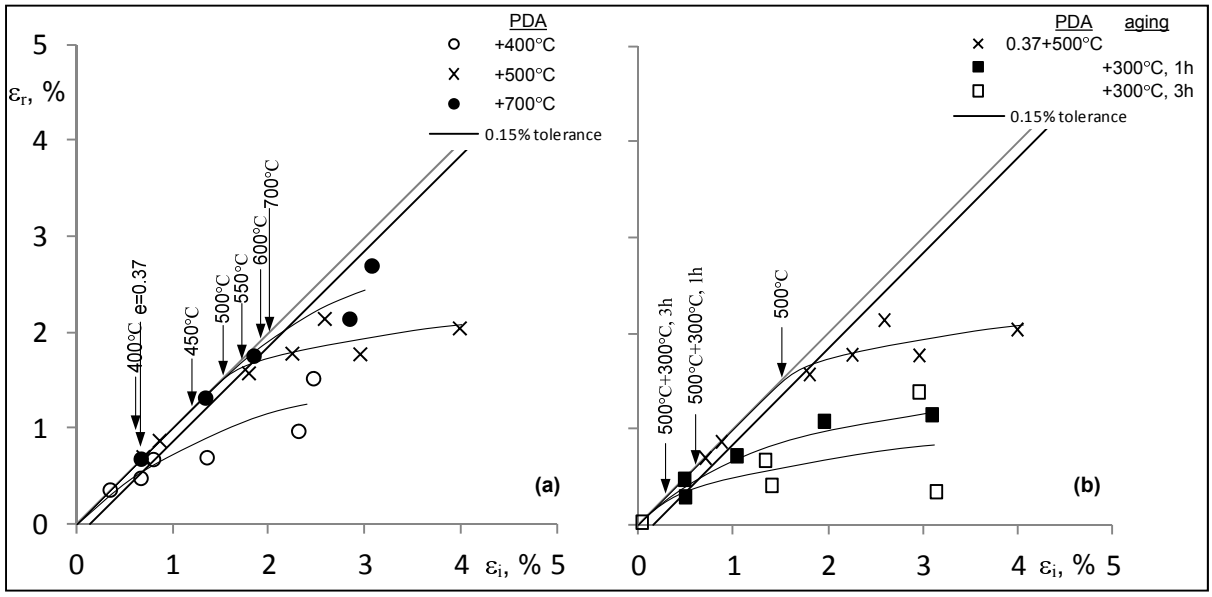

Figure 3.11 Recovery strain dependence on induced strain in bending SM testing at -196°C and subsequent heating above A_f of Ti-Nb-Ta alloy subjected to CR+PDA (1h) (a) and CR+PDA+AG (300°C, 1h and 3h) (b). To facilitate observation, not all the experimental points are presented

3.6 Discussion

It can be shown that the measured mechanical and functional properties of the studied alloy are in direct correlation with the material microstructure. Post-deformation annealing of the Ti-Nb-Ta SMA initiates recovery, polygonization and recrystallization processes in β-phase (Figure 3.1, Figure 3.2). Low-temperature aging of NS structure at 300°C is accompanied by a slow development of the ω-phase precipitation in the nanosubgrained β-phase. The ω-particles preserve their globular shape, random distribution and very fine size for up to 1h of aging (Figure 3.3), thus creating an optimum dispersion hardening for the longest cyclic life. During further aging, a transform to elongated coarsened ω-particles develops (Figure 3.3). As a result, this "overaging" worsens superelastic cyclic life.

Annealing at 500°C corresponds to drastic material softening, which is clearly observed in both single-cycle (Figure 3.4) and multi-cycle (Figure 3.7a-d) testing. On one hand, the higher the annealing temperature, the lower the dislocation density and therefore the higher the alloy's M_s temperature [9]. On contrary, the higher the annealing temperature, the higher the enrichment of β-phase by Nb and Ta β-stabilizers because of the formation of ω- and α"-phases with higher than β-phase Ti content, and therefore the lower the alloy's M_s temperature [13]. These phenomena concurrently influence the alloy's mechanical behavior: the closer the testing temperature to M_s temperature, the lower the phase transformation stress [14]. In the vicinity of 500°C, concurrrence of the above mentioned phenomena is superimposed on the low stability of β-phase (β→α" transformation) and therefore results in accentuated material softening. When annealing temperature approaches 700°C, material recrystallization results in a significant grain refinement of the studied alloy [15], which additionally contributes to the material hardening.

The greater the aging time, the higher the transformation yield stress of the material (Figure 3.5 and Figure 3.7h-k). These observations are explained by two concomitant phenomena: the enrichment of the parent phase by Nb and Ta, and the ω-phase precipitation hardening. The first assertion is based on the information known from [10], whereas the second assertion is supported by a TEM study of the ω-phase precipitation phenomenon presented in section "Structure of thermomechanically treated Ti-Nb-Ta alloy" of this paper.

It can be seen that the following processing sequences: route (A), Figure 3.7b,c: e=0.37+ PDA (T=400, 450°C,1h), and route (B), Figure 3.7j: e=0.37+PDA (T=500°C, 1h) +AG (300°C, 1h), lead to the longest cyclic lives. However, strain accumulated to failure is much larger after route (B) than after route (A). The reason for this difference resides in the quite different material microstructures resulted from these processing routes: route (A) leads to a highly dislocation- and ω precipitation-hardened structure, whereas route (B) leads to an ω-precipitation-hardened NS structure, the latter being more ductile than the former. Indeed the true ("dislocation") yield stresses σ_y are about 600 and 450 MPa, respectively, for these two cases (Figure 3.7c and f). When aging time increases from 1 to 3 h, ω-phase particles change

size, quantity and distribution: they grow, their quantity increases and distribution changes: from random distribution of small equiaxed particles, they form now large elongated rows of coarsened particles (Table 3.2), which naturally leads to excessive structure hardening and to decrease in the crack's propagation resistance under repetitive loading [13, 16]. Figure 3.12 12 contains the quantitative analysis of number of cycles to failure after different TMTs.

Given that the main objective of cyclic testing was to determine the most appropriate processing conditions from the functional fatigue point of view, the number of cycles to failure was by far the most important parameter to be discussed. For example, if we compare diagram (d) and diagram (j) of Figure 3.7, failure strain in both cases is about 9%, whereas the number of cycles to failure is very different: respectively 13 and 259. Based on these observations, the processing conditions leading to diagram (j) are much better suited for cyclic application than processing conditions leading to diagram (d). It should be noted that Ti-19.7Nb-5.8Ta (at.%) SMA of this study manifests significantly lower fatigue life than Ti-21.8Nb-6Zr (at.%), under similar samples' preparation and testing conditions. For example, after e=0.37+PDA (600^{o}C, 30 min), the number of cycles to failure of Ti-Nb-Zr alloy is 877 [12], whereas it is only ~260 in Ti-Nb-Ta alloy of this study. Note also that Ti-50.26at.%Ni SMA outperforms from five to ten times any Ti-Nb-based alloys in this respect: the number of superelastic cycles to failure of Ti-Ni samples reaches 2700 (3% strain applied in each cycle) when the alloy's microstructure corresponds to the mixed nanosubgrained and nanocrystalline structure of B2-phase [17].

In Figure 3.12, maximum completely recoverable strain (Figure 3.11) and the number of cycles to failure (Figure 7) are plotted as functions of PDA temperature and aging time. It can be noted that the higher the annealing temperature, the greater the recovery strain, but the lower the number of superelastic cycles to failure: the longest strain-controlled fatigue life is observed after PDA at 400^{o}C and 450^{o}C (Figure 3.12a). Furthermore, as previously shown (Figure 3.7j), 300^{o}C (1h) aging results in an almost 20-time increase in fatigue life and a smaller maximum completely recoverable SM strains as compared to PDA at 500^{o}C without aging. Both residual strain-hardening (low-temperature annealing) and ω-phase precipitation

(aging) phenomena increase the material yield stress [13]. As a result, in the low-temperature annealed and aged samples, at the same testing temperature (RT), the accumulated plastic deformation is smaller and superelastic fatigue life is longer. On contrary, strain and precipitation-induced hardening decrease the quantity of martensite formed and reoriented at -196°C (SM testing strain-inducing temperature) and therefore recovered upon heating of deformed samples.

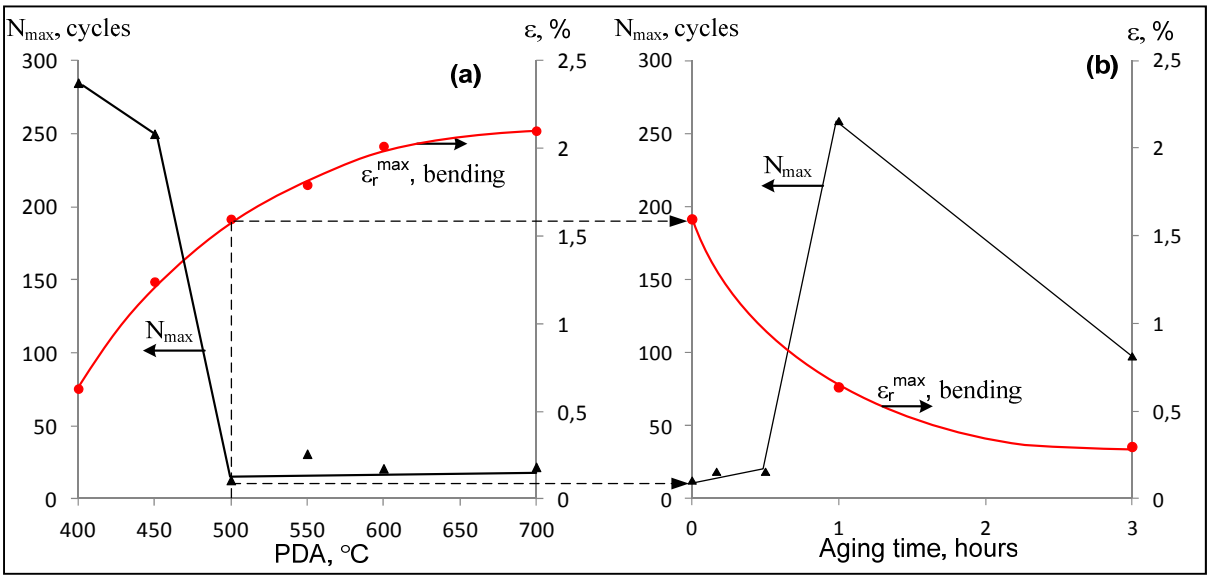

Figure 3.12 Maximum completely recoverable strain of shape memory effect (ε_r^{max}) and number of cycles to failure N_{max} after e=0.37+PDA (a) and e=0.37+500°C (1h)+300°C (t=var) (b)

3.7 Conclusions

1. For Ti-19.7Nb-5.8Ta (at.%) alloy, annealing at 500-600°C after moderate cold rolling (e=0.37) results in the formation of a nanosubgrained structure in β-phase as a result of polygonization of a dislocation substructure. After annealing at 650-750°C, recrystallization and grain growth occur. A distinct lamellar contrast in TEM images after annealing at 500°C can be attributed to α”-martensite crystals formed during cooling and thin foil preparation at -38 °C.

2. Low-temperature aging (300^{o}C) of the β -phase nanosubgrained structure is accompanied by the ω-phase precipitation phenomena. Up to 1h-aging, ω-particles preserve their globular shape, random distribution and very fine size. During further aging, elongated rows of coarsened ω-particles form.

3. Depending on the annealing temperature, the studied alloy manifests either mainly superelastic or mainly shape memory behavior at RT: PDA under 500^{o}C results in mainly superelastic behavior, whereas PDA at 500^{o}C and higher, results in mainly shape memory behavior; the maximum completely recoverable SM strain is observed after CR (0.37)+PDA (600-700^{o}C), and its value is close to 2%.

4. As compared to unaged alloy, an "optimum" ω-phase precipitation hardening caused by 300^{o}C, 1h aging of the nanosubgrained substructure resulted from CR(e=0.37)+PDA(500^{o}C, 1h) leads to a more than 20-time longer cyclic life.

5. Both the well-developed dislocation substructure obtained after CR(e=0.37)+PDA(400/450^{o}C, 1h), and the precipitation-hardened nanosubgrained microstructure obtained after CR(e=0.37)+PDA(500^{o}C, 1h)+aging (300^{o}C, 1h), result in similar fatigue lives, but the aged alloy appears to be much more ductile than the simply annealed.

3.8 Acknowledgments

The present work was carried out with financial support of the Natural Science and Engineering Research Council of Canada and of the Ministry of Education and Science of the Russian Federation.

3.9 References

[1] US patent 3579831, Stevens, Irving J.; Alexander, Jerry, "Bone Implant", issued 1971-05-25.

[2] G.C. Leventhal, Titanium, a metal for surgery, J. Bone Joint Surg., 33, 1951, 473-474.

[3] C. Baker, The Shape-Memory Effect in a Titanium-35 wt.% Niobium Alloy, Metal Sci. J., 5, 1971, 92-100.

[4] K. Takamura, K. Hayashi, N. Ishinishi, T. Yamasda, Y. Sugioka, Evaluation of carcinogenicity and chronic toxicity associated with orthopedic implants in mice, J. Biomed. Mater. Res., 28(5), 1980, 583-589.

[5] M. Long, H.J. Rack, Titanium alloys in total joint remplacement – a material science perspective, Biomat., 19, 1998, 1621-1639.

[6] M.I. Petrzhik, S.G. Fedotov, U.K. Kovneristiy, N.F. Zhebyneva, Влияние термоциклирования на структуру закаленных сплавов системы Ti-Ta-Nb (Influence of thermocycling on the structure of quenched Ti-Ta-Nb alloys), Metal Science and Heat Treatement of Metals, 3, 1992, 2-4, (in Russian).

[7] S. Miyazaki, H.Y. Kim, H. Hosoda, Development and characterization of Ni-free Ti-base shape memory and superelastic alloys, Mater. Sci. and Eng. A, 438–440, 2006, 18–24.

[8] H.Y. Kim, Y. Ikehara, J.I. Kim, H. Hosoda, S. Miyazaki, Martensitic transformation, shape memory effect and superelasticity of Ti-Nb binary alloys, Acta Mater., 54(9), 2006, 2419-2429.

[9] V. Brailovski, S. Prokoshkin, M. Gauthier, K. Inaekyan, S. Dubinskiy, M. Petrzhik and M. Filonov, Bulk and porous metastable beta Ti-Nb-Zr(Ta) alloys for biomedical applications, Mater. Sci. Eng. C, 31, 2011, 643-657.

[10] M. Geetha, A.K. Singh, A.K. Gogia, R. Asokamani, Effect of thermomechanical processing on evolution of various phases in Ti-Nb-Zr alloys, J. of Alloys and Comp., 384, 2004, 131-144.

[11] Shape memory alloys: fundamentals, modeling and applications, V. Brailovski, S. Prokoshkin, P. Terriault, F. Trochu, ed., ÉTS, Montréal, 2003, 844 p.

[12] V. Brailovski, S. Prokoshkin, K. Inaekyan, S. Dubinskiy, M. Gauthier, Mechanical properties of thermomechanically-processed metastable beta Ti-Nb-Zr alloys for biomedical applications, Materials Science Forum, 706-709, 2012, 455-460.

[13] E.W. Collings, The physical metallurgy of titanium alloys, ASM, 1984, 223 p.

[14] Shape memory materials, K. Otsuka and C.M. Wayman, ed., Cambridge University Press, 1998, 284 p.

[15] S.M. Dubinskiy, S.D. Prokoshkin, V. Brailovski, A.V. Korotitskiy, K.E. Inaekyan, M.R. Filonov, M.I. Petrzhik, Structure formation during thermomechanical processing of Ti-Nb-Zr(Ta) alloys and manifestation of the shape-memory effect, Physics of Metals and Metallography, 112, 2011, 529-542.

[16] U. Krupp, Fatigue crack propagation in metals and alloys. Microstructural aspects and modeling concepts, Wiley-VCH Verlag GmbH&Co. KGaA, 2007, 287 p.

[17] A. Kreitcberg, V. Brailovski, S. Prokoshkin, Y. Facchinello, K. Inaekyan, S. Dubinskiy, Microstructure and functional fatigue of nanostructured Ti-50.26at%Ni alloy after thermomechanical treatment with warm rolling and intermediate annealing, Materials Science and Engineering A, 562, 2013, 118-127.

CHAPTER 4

ARTICLE #3: *IN SITU* X-RAY DIFFRACTION STRAIN-CONTROLLED STUDY OF Ti-Nb-Zr AND Ti-Nb-Ta SHAPE MEMORY ALLOYS: CRYSTAL LATTICE AND TRANSFORMATION FEATURES

4.1 Summary

The objective of this article is to investigate the crystal lattice and transformation features in the biomedical Ti-Nb-Zr and Ti-Nb-Ta SMA in the temperature range of martensitic transformations with or without external load. A custom tensile stage fitted within the *TTK450* thermochamber of a *PANalytical X'Pert Pro* diffractometer is used in the -150...+100^{o}C temperature range. The working principle of tensile stage is described in detail in the Annex.

It is observed that upon heating, the martensitic α"-phase lattice parameters undergo a constant evolution towards the corresponding parent β-phase lattice parameters, which results in reversible shifts of anisotropic α"-martensite X-ray lines. The crystallographic resource of recovery strain in Ti-Nb-Zr is almost double that in Ti-Nb-Ta with the same concentration of alloying elements: 4.5 versus 2.5% in the framework of the single-crystal calculations. Loading at any temperature forms an additional quantity of α"- and ω-phases at negative temperatures (ω-phase, in Ti-Nb-Zr only), and subsequent α"-phase reorientation during loading or/and heating. Moreover, loading during heating results in a two-step transformation sequence: ω→β + β→α" (or (β+ω)→α") is followed by α"→β transformation. It is practically proven that the recovery stress generation phenomenon in the Ti-Nb-based SMA are the direct result of the reverse α"→β transformation. The completely reversible β-phase X-ray line widening under external loading and temperature scanning is the result of the thermoelastic martensitic formation and disappearance. This article was submitted to the journal Materials Characterization in August 2013.

IN SITU X-RAY DIFFRACTION STRAIN-CONTROLLED STUDY OF Ti-Nb-Zr AND Ti-Nb-Ta SHAPE MEMORY ALLOYS: CRYSTAL LATTICE AND TRANSFORMATION FEATURES

S. Dubinskiy[a,b], S. Prokoshkin[b], V. Brailovski[a], K. Inaekyan[a], A. Korotitskiy[b]

[a]École de technologie supérieure, 1100, Notre-Dame Street West, Montreal (Quebec), H3C 1K3, Canada

[b]National University of Science and Technology "MISIS", 4, Leninskiy prosp., Moscow 119049, Russian Federation

4.2 Abstract

Phase and structure transformations in biomedical Ti-21.8Nb-6.0Zr (TNZ) and Ti-19.7Nb-5.8Ta (TNT) shape memory alloys (at%) under and without load in the -150 to 100°C temperature range are studied *in situ* using an original tensile module for a low-temperature chamber of an X-ray diffractometer. Alpha"- and beta-phase lattice parameters, the crystallographic resource of recovery strain, phase and structure transformation sequences, and microstress appearance and disappearance are examined, compared and discussed. For both alloys, the crystallographic resource of recovery strain decreases with temperature increase to become 4.5% for TNZ and 2.5%, for TNT alloy (at RT). Loading at low temperatures leads to additional α"-phase formation and reorientation. Heating under load, as compared to strain-free heating, affects the reverse transformation sequence of both alloys in different ways. For TNZ alloy, strain-free heating results in simultaneous ω→β and α"→β transformations, whereas during heating under stress, they are sequential: β+ω→α" precedes α"→β. For TNT alloy, strain-free heating results in reverse α"→β transformation, whereas during heating under stress, α"→β transformation is preceded by α"-phase reorientation.

Keywords: titanium alloys, biomedical shape memory alloys, *in situ* X-ray diffraction, lattice parameters, transformation lattice strain, recovery strain

4.3 Introduction

Since the beginning of this century, metastable near-β Ti-Nb-based shape memory alloys (SMA) have attracted significant attention from biomedical engineers as promising substitutes for pure titanium, and for α+β (Ti-Al-V), β (Ti-13Nb-13Zr), and shape memory Ti-Ni alloys [1-11]. These alloys combine the exceptionally low Young's modulus and superelasticity of Ti-Ni with the high biocompatibility of pure titanium. In other words, metastable near-β Ti-Nb-based SMAs mimic the mechanical behavior of living bone while promoting osteogenesis and minimizing the risks of implant loosening.

The superelasticity and shape memory properties of metastable Ti-Nb-based alloys are based on a reversible thermoelastic martensitic transformation of their parent BCC β-phase into martenstic orthorhombic α"-phase [12, 13]. Initially, the superelasticity of these alloys represented virtually the sole property to be practically exploited. However, it was recently demonstrated however that these alloys could generate recovery strains as high as 6…8% (Ti-Nb-Zr SMA [14, 15]), which could justify their application as "shape memory" alloys. The reversible phase and structure transformation features of these alloys under conditions of stress-free and constrained shape recovery are thus of significant practical interest.

Since athermal transformations can be induced by both temperature and external load variations, phase analysis under variable stress-temperature conditions is necessary for their proper understanding. This type of *in situ* analysis has been used in neutron diffraction studies of Ti-Ni SMA transformation features at temperatures above RT [16-21]. Meanwhile, *in situ* X-ray diffraction studies of multiphase Ti-based SMA have been carried out either under external load or temperature variations [1, 22-26], but never under variations of both state parameters.

Furthermore, it was shown for Ti-Nb-Ta [1] and Ti-Nb [23, 26] alloys that the lattice parameters (LP) of both α"- and β- phases vary with temperature variation, and that upon heating, the LPs of the martensitic α"-phase strive towards the corresponding LPs of the

parent β-phase. This phenomenon, which was also observed in Ti-Ni SMA [19, 27], indicates that the crystallographic resource of recovery strain in all SMAs is strongly temperature-dependent, and therefore merits a dedicated study.

Finally in [28, 29], softening and then recovery stress generation and relaxation processes were observed during the heating of constrained samples of Ti-Nb-Zr and Ti-Nb-Ta SMAs from -150°C (Figure 4.1). A clear understanding of the stress generation mechanisms was complicated by the alloy's specific phenomena, including athermal ω-phase formation and reverse ω→β and α"→β transformations [13, 25]. It is thus of interest to study the phase transformation sequences in Ti-Nb-Zr and Ti-Nb-Ta alloys during cooling-heating with and without loading.

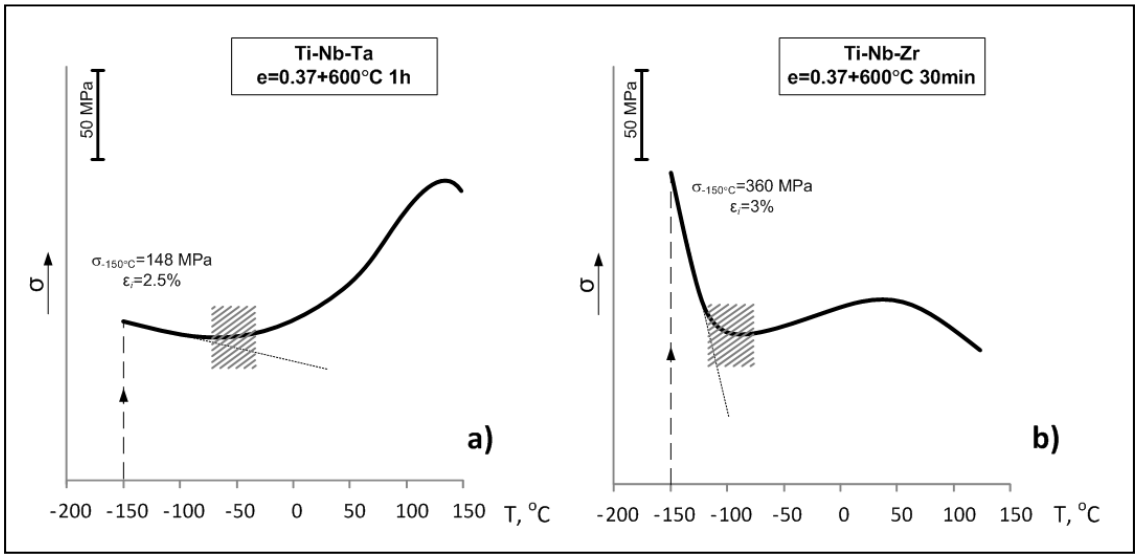

Figure 4.1 Stress-temperature curves obtained during constant-strain heating of the thermomechanically-treated Ti-Nb-Ta (a) and Ti-Nb-Zr (b) samples (adapted from [28, 29]). Shadowed areas indicate the onset temperatures of the reverse α"→β phase transformation under stress

For the above-mentioned reasons, the goal of this work is a comparative study of phase and structure transformations in Ti-Nb-Zr and Ti-Nb-Ta SMA in the -150…+100°C temperature range during cooling-heating, with and without external mechanical loading.

4.4 Experimental

Ti-Nb-Zr (TNZ) and Ti-Nb-Ta (TNT) SMAs were studied (see Table 4.1 for their composition). The TNZ alloy is a 50 mm-diameter, 660 mm-long cylindrical ingot produced by Induction Skull Melting followed by Hot Isostatic Pressing (HIP, 900^{o}C, 100 MPa, 2h) at the *Flowserve Corp.*, USA. The TNT alloy 80 mm-diameter 7 kg ingot was produced by Vacuum Arc Melting at the *TSNIICHERMET*, Russia, then hot forged (900^{o}C) and machined to a 51 mm-diameter, 600 mm-long cylindrical bar.

Table 4.1 Chemical compositions of studied alloys

Alloy	Main elements, at.%[a]				Impurities, at.%			
	Ti	Nb	Zr	Ta	O	C	N	H
TNZ	72.2	21.8	6.0		0.49	0.05	0.03	0.59
TNT	74.5	19.7		5.8	0.16	0.05	0.03	0.35

[a]without impurities content

A series of 1.2×0.8×100 mm TNZ specimens were Electro Discharge Machining (EDM)-cut from the HIP-processed ingot, then cold-rolled in several passes to an accumulated true strain of e=0.37 and annealed at 600^{o}C for 0.5h. A series of 8×2×50 mm TNT bars were diamond-saw cut from the hot-forged ingot, then cold-rolled in several passes to an accumulated true strain of e=0.3, EDM-cut into 1×1×50 mm specimens, and finally annealed at 500^{o}C for 1h. Note that for both alloys, the regimes of their thermomechanical processing were selected in conformity with [29] and [30]. These processing conditions create specific nanosubgrained structures in TNZ and TNT alloys that are well suited for biomedical applications from the mechanical properties' point of view [30].

Finally, the TNZ and TNT specimens were cut in 30 mm length and mechanically polished to 0.1 – 0.15 mm thickness. All samples were etched in 2HF : 1HNO_3 : 17H_2O, 1HF : 15HNO_3 : 5H_2O, and 1HF : 4HNO_3 : 5H_2O solutions to remove a damaged surface layer.

In this work, *in situ* X-ray phase analysis was performed using an original tensile module fit in a *TTK450* low-temperature chamber of a *PANalytical X'Pert Pro* diffractometer. The tensile module is shown in Figure 4.2a. The independent Ti-Ni actuator (1), subjected to thermal cycling under constant load (two-way shape memory effect training) before testing, was connected through the rotating levers (2) to the specimen (3). The main frame (4) of the tensile stage was directly mounted on the control plate of the thermal chamber. When the actuator (1) was heated by Joule heating, it shortened and stretched the specimen (3). Specimen temperature is measured by the K-type thermocouple (5), welded to one of the guiding shafts (6) close to the specimen. The standard thermocouple of a *TTK450* temperature control module is attached to the side of the main frame (4). Since there was a significant difference between the measurements provided by these two thermocouples, the temperature of the control plate was adjusted manually to get the specimen to the target temperature for each testing step. The working principle of the module is described in detail in [31].

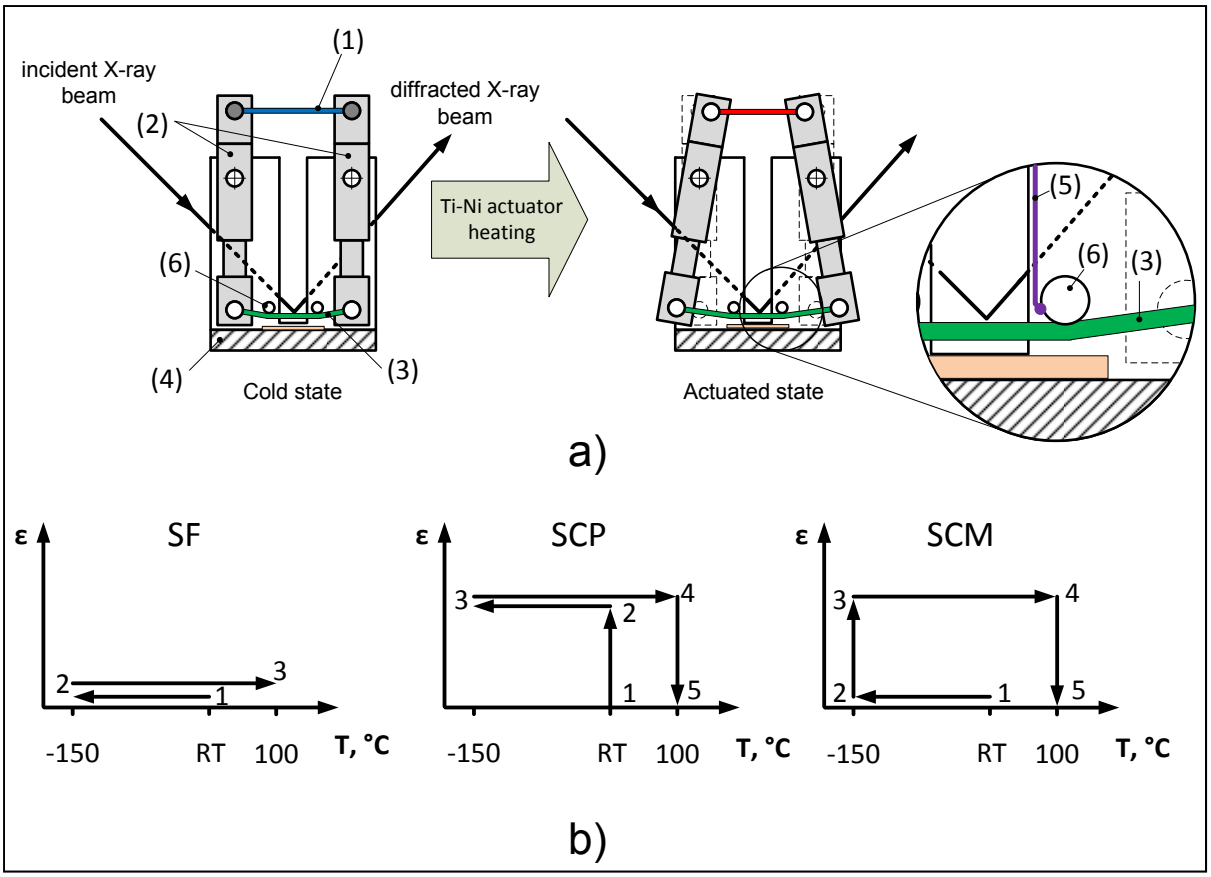

Figure 4.2 Tensile module for the *PANalytical X'Pert Pro* diffractometer: a) schematics of the working principle; b) schedules of the in situ X-ray diffraction temperature scanning experiments: SF – strain-free; SCP – strain-controlled with loading at RT; and SCM – strain-controlled with loading at -150°C [31]

In situ X-ray diffraction analysis was performed in the -150 … +100°C temperature range under $Cu_{K\alpha}$ monochromatized radiation. Three *in situ* X-ray temperature scanning experiments were carried out (Figure 4.2b):

- The strain-free (SF) temperature scanning experiment followed a 1→2→3 path (Figure 4.2b). Point 1 corresponds to X-ray analysis at RT, point 2, at -150°C, and point 3, at 100°C, with intermediate X-ray recording upon heating. In this experiment, β↔α" transformation was temperature-induced.

- The strain-controlled temperature scanning experiment (SCP), with loading of the parent β-phase (RT), followed a 1→2→3→4→5 path (Figure 4.2b). Points 1 and 2 correspond to X-ray analysis before and after loading at RT, point 3 corresponds to analysis of the strained specimen cooled to -150°C, and points 4 and 5, to analysis at 100°C before and after unloading. Upon heating, a series of intermediate X-ray diffractograms are obtained. In this experiment, α"-martensite forms and it is reversely transformed to the parent β-phase under the combined influence of temperature and stress.

- The strain-controlled temperature scanning experiment (SCM), with loading of the mixed parent (β) + thermally-induced martensite (α") phase (-150°C), followed a 1→2→3→4→5 path (Figure 4.2b). Point 1 corresponds to strain-free X-ray analysis at RT, points 2 and 3 correspond to analysis at -150°C, before and after loading, and points 4 and 5 correspond to analysis at 100°C before and after unloading. Upon heating, a series of intermediate X-ray diffractograms are obtained. In this experiment, α"-martensite forms initially during stress-free cooling and then additionally under stress.

The tensile module loading ability was verified by calculating the tensile strain applied to the sample during the *in situ* scanning experiments. Indeed, at each recording temperature, X-ray diffractometry allows direct strain measurement in the direction perpendicular to the specimen surface (transverse strain $\varepsilon_{\perp}$). At each recording temperature, a longitudinal tensile strain induced in the sample during SCM or SCP experiments (ε) can therefore be calculated from the difference between the transverse strain $\varepsilon_{\perp}$ and the thermal expansion strains $\varepsilon_{\perp}^{\Delta T}$:

$$\varepsilon = \frac{\varepsilon_{\perp} - \varepsilon_{\perp}^{\Delta T}}{\mu}, \text{ where } \varepsilon_{\perp} = \left(\frac{\Delta d_{hkl}}{d_{hkl}} \right) \times 100\%, \qquad (4.1)$$

where $\varepsilon_{\perp}$ is the directly measured transverse strain, $\varepsilon_{\perp}^{\Delta T}$ is the thermal expansion strain (directly measured during the SF experiment), d_{hkl} is the *hkl*-plane strain-free interplanar distance, Δd_{hkl} is the strain-induced interplanar distance variation, and μ=0.3 [13] is the Poisson's ratio.

It can be seen that during SCM and SCP experiments in the -150…+100^{o}C temperature range, the longitudinal strain ranged from 0.8 to 1.35% for TNT alloy (Figure 4.3a) and from 0.8 to 1.6% for TNZ alloy (Figure 4.3b). These strains correspond to non-linear parts of the tensile stress-strain curves plotted for both alloys at different temperatures, all within the temperature range of interest (Figure 4.3c,d). This means that in all cases, the applied strain applied led to stress-induced phase transformations. It can also be observed that the overall strain fluctuations during SCM and SCP experiments were ±20% (TNT) and ±15% (TNZ). These relatively high fluctuations were mainly due to recovery stress generation phenomena occurring in the tested specimens combined with the limited stiffness of the testing module mainframe. The authors believe however that these fluctuations do not affect the validity of the results obtained, given the mainly qualitative and comparative nature of this study.

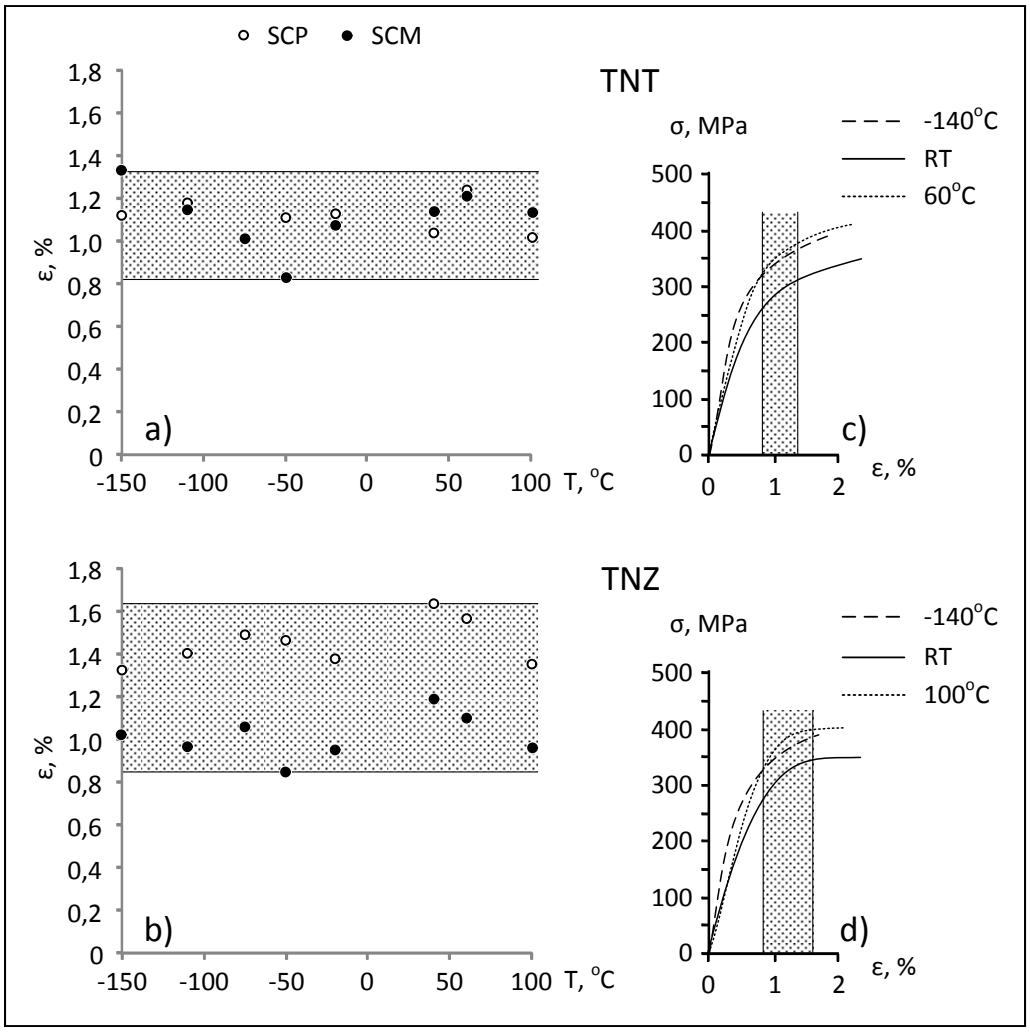

Figure 4.3 Tensile strains measured on heating during SCP and SCM experiments for TNT (a) and TNZ (b) alloys, and tensile loading curves at various recording temperatures for TNT (c) and TNZ (d) alloys. Stress-strain curves (c,d) are obtained in tensile tests similar to [28]

Identification and indexing of the β-, α-, α”- and ω-phases’ X-ray lines was performed using a reference diffractogram built in accordance with the available data [1, 13, 20]. The β-phase true lattice parameter a_β values extrapolated to a $\theta=90^o$ angle were calculated for each recording temperature from the angular coordinates of 110, 200, 211, 220 and 310 β-phase lines using the Nelson-Riley extrapolation function [32]. The calculated a_β values for TNT and TNZ alloys are presented as a function of the X-ray diffractogram recording temperature in Figure 4.4.

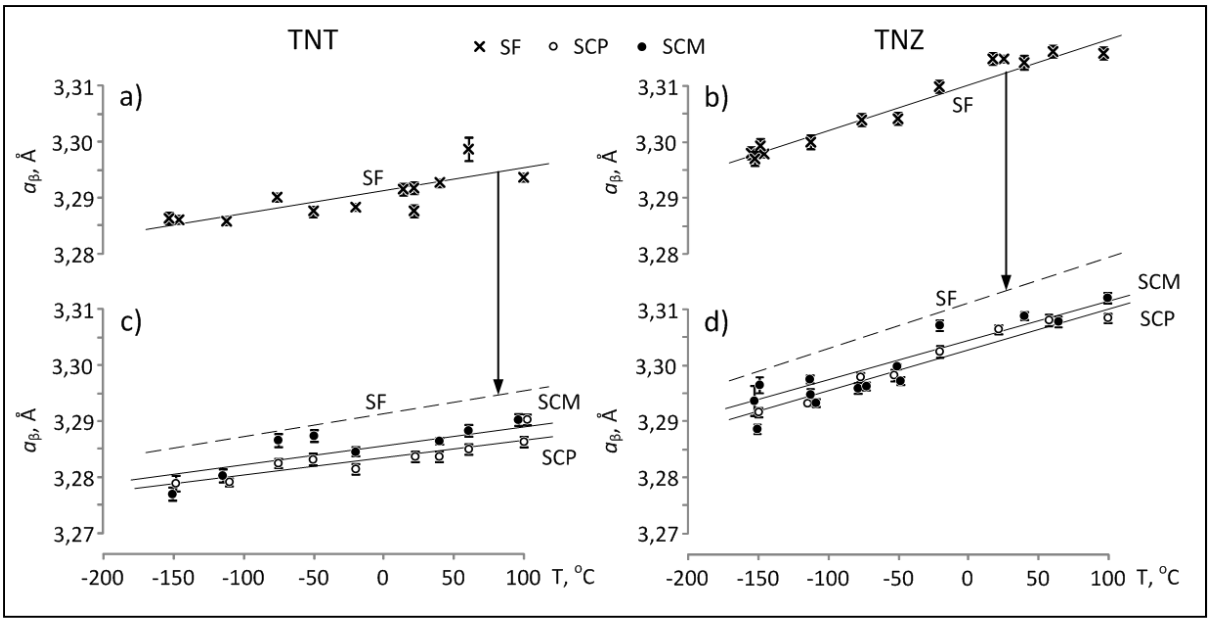

Figure 4.4 Beta-phase lattice parameter temperature dependence for SF (a,b), SCM and SCP (c,d) experiments for TNT (a,c) and TNZ (b,d) alloys. – – – are the least-squares regressions taken from a) to c) and from b) to d) to facilitate comparison

The α”-martensite peak angular coordinates were corrected based on the β-phase peak angular coordinates, i.e., each *a, b,* and *c* martensite lattice parameter was corrected in accordance with the slope of the $a_\beta(\theta)$ extrapolation line. The α”-martensite lattice parameters (LPs) were calculated based on the corrected angular coordinates of the most unambiguously-determined α”-martensite peaks (at least four peaks) using the least-squares method [33]. The Fisher criterion was used for evaluation of the statistical significance of the calculated martensite LPs with a P=0.95 confidence probability.

From the available data on Ti-Nb-based SMA, there is no uniqueness in indexing some martensite peaks. Thus, $130_{\alpha”}$ and $211_{\alpha”}$ lines can be close to each other or coincide [34]. Our calculations show that their angular positions change with temperature, and in opposite directions. Therefore, martensite peak indexing was cross-verified through the peak position recalculation from the initially calculated LPs, considering the X-ray line coordinate temperature drifts. As a result for TNT, the martensite peak between 65 and 66° (2θ) was indexed as $130_{\alpha”}$ based on the direction of its angular shift with temperature. For TNZ, the

martensite peak between 64 and 65^{o} (2θ) was indexed as $211_{\alpha"}$, as the application of other indexes ($130_{\alpha"}$, for example) led to a significant discordance of the peak positions with a real X-ray diffractogram.

The maximum martensitic transformation lattice strain (ε_{max}), i.e., a crystallographic resource of recovery strain was calculated from the martensite α"- and parent β-phase LPs following the methodology of [33, 35, 36].

4.5 Results

4.5.1 Structure transformations and crystal lattice changes

Ti-Nb-Ta

Since the results obtained with the strain-controlled SCM and SCP experiments are similar, we limit our presentation to the SCM and SF experiments (see selected diffractograms in Figure 4.5). In Figure 4.6, β- and α"-phase X-ray line angular coordinates variations are plotted as functions of the diffractograms' recording temperature.

At RT, β-phase is the main phase constituent in all three experiments. A significant amount of α"-martensite and a small quantity of α-phase are observed as well. The presence of ω-phase is also supposed, however, its quantity is not enough for reliable detection.

Generally speaking, temperature changes are accompanied by reversible X-ray line angular shifts, temperature and stress-induced formation of α"-phase upon cooling, and reorientation and reverse transformation of α"-phase to β-phase upon heating.

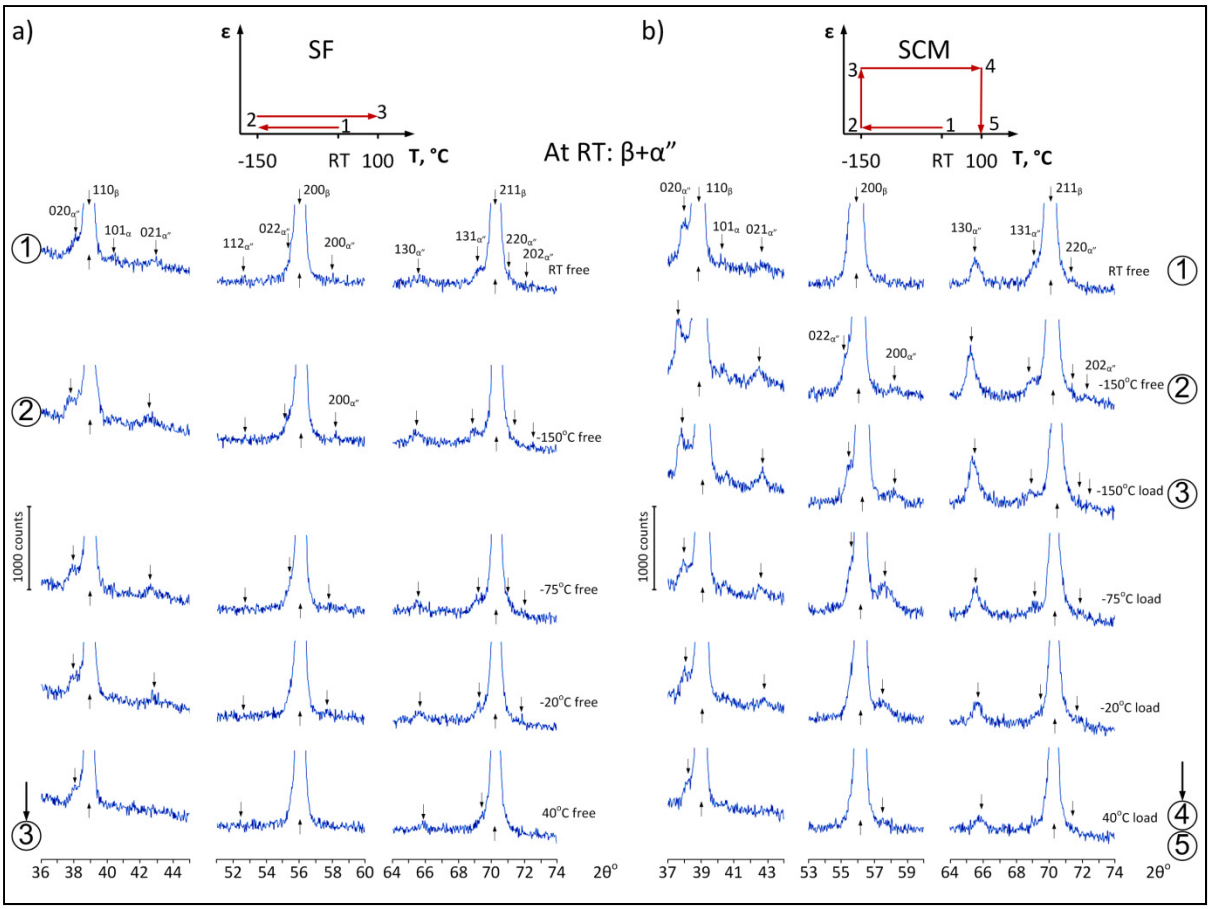

Figure 4.5 Selected X-ray diffractograms of TNT from SF (a) and SCM (b) experiments. The experimental positions 1-3 from the SF and 1-4 from the SCM experiments in Figure 4.2b are indicated

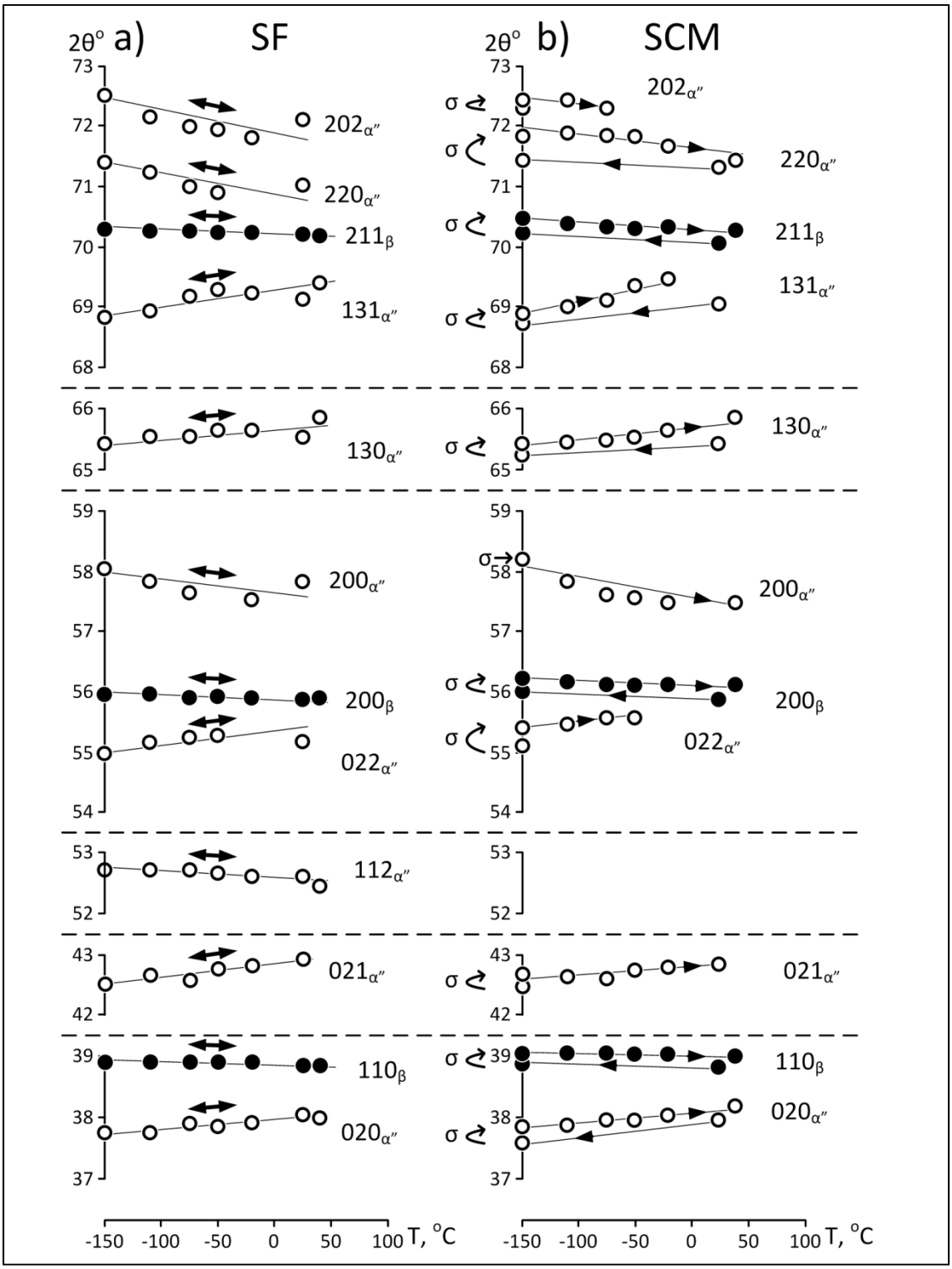

Figure 4.6 TNT alloy: X-ray line angular coordinates versus diffractogram recording temperature from SF (a) and SCM (b) experiments: ● – β-phase, ○ – α”-phase

X-ray line angular positions and phase constituents

Under strain-free cooling of TNT samples from RT to -150°C in SF and SCM experiments, all β-phase lines shift to higher θ angles due to thermal contraction, whereas α”-phase lines shift in different directions (Figure 4.6): $020_{\alpha”}$, $021_{\alpha”}$, $022_{\alpha”}$, $130_{\alpha”}$ and $131_{\alpha”}$ shift to lower θ angles, while $112_{\alpha”}$, $200_{\alpha”}$, $220_{\alpha”}$ and $202_{\alpha”}$ shift to higher θ angles (see also Figure 4.5). Strain-free heating in the -20…+100°C temperature range is accompanied by incomplete reverse β→α” transformation and X-ray line shifts of both β- and α”-phases back to their RT positions (Figure 4.5a, Figure 4.6a).

Application of an external tensile stress at -150°C leads to shifting of all the β- and α”-phase lines towards higher θ angles and to a minor increase and partial reorientation of α”-phase (see the enhancement of the $200_{\alpha”}$ line in Figure 4.5b). Subsequent heating under load from -150 to +100°C is accompanied by martensite reorientation in the -150…-75°C temperature range ($200_{\alpha”}$ growth at the expense of weakening $020_{\alpha”}$, $021_{\alpha”}$, $022_{\alpha”}$ and $130_{\alpha”}$), reverse α”→β transformation in the -50…100°C temperature range and X-ray lines shifts of both β and α”-phases back to their RT positions (Figure 4.6b).

Lattice parameters (LPs)

The LPs of parent β- and martensite α”-phases of TNT alloy are presented in Figure 4.7 as functions of the recording temperature. The β- and α”-phases unit cell volumes are calculated as $\omega_\beta = a_\beta \times b_\beta \times c_\beta$ (where a_β, b_β and $c_\beta = b_\beta$ are the LPs of FCT β-phase) and $\omega_{\alpha”} = a_{\alpha”} \times b_{\alpha”} \times c_{\alpha”}$ (where $a_{\alpha”}$, $b_{\alpha”}$ and $c_{\alpha”} = b_{\alpha”}$ are the LPs of orthorhombic α”-phase).

All the α”-phase LPs were calculated after the α”-phase peak positions were corrected with reference to the β-phase peak positions, considering their strain-induced shifts, so that they could be compared directly *inter se*. The maximum transformation lattice strain ε_{max} as a function of the testing temperature was calculated from the α”- and β-phase LPs (Figure 4.7).

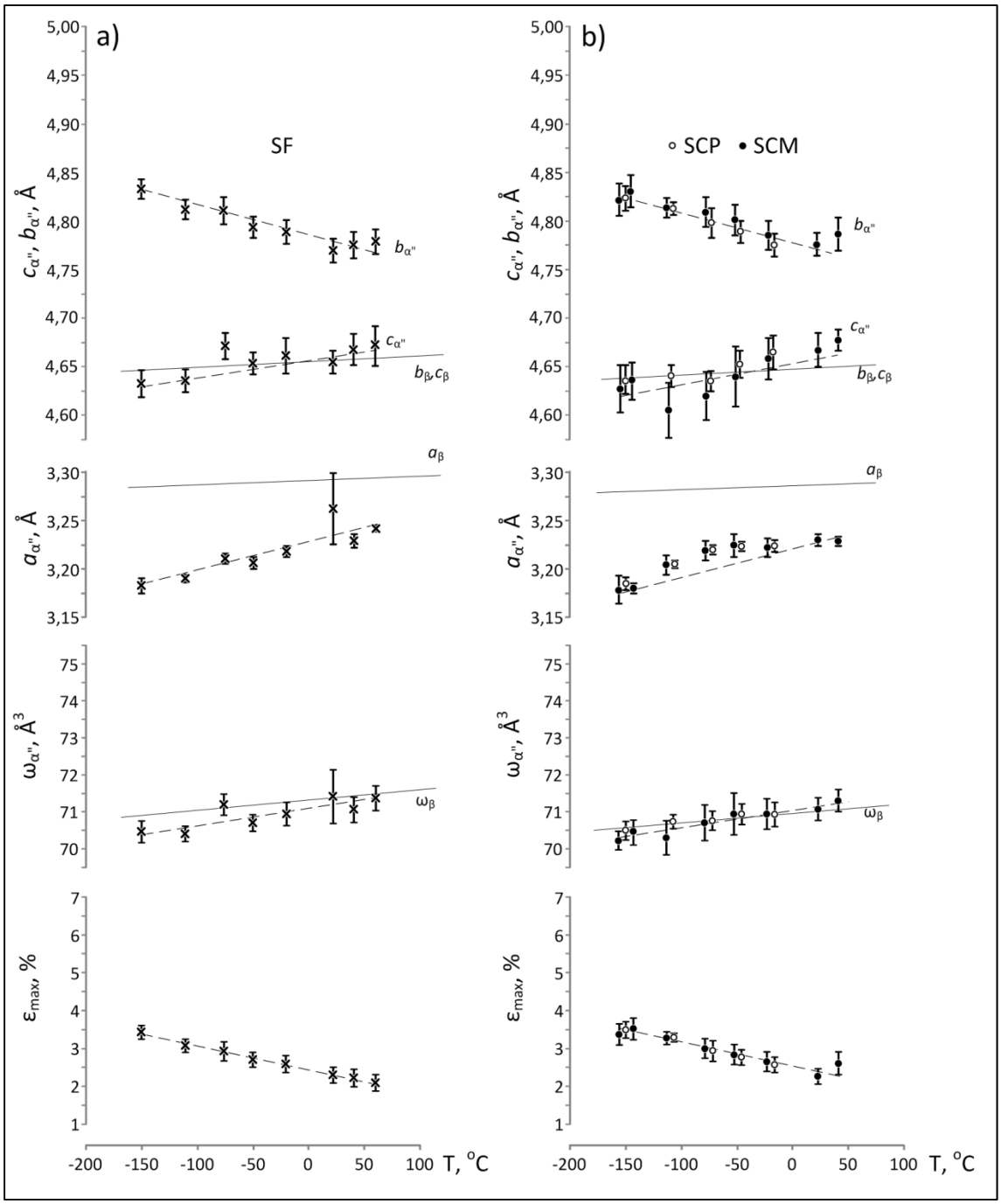

Figure 4.7 TNT alloy: temperature dependence of the α”-phase LPs and ε_{max} in SF (a) and in SCM, SCP (b) experiments. The solid lines for a_β, b_β, c_β and ω_β are brought here from Figure 4.3

Ti-Nb-Zr

Since the results obtained during heating with the strain-controlled SCM and SCP experiments are similar, we limit our presentation to the SCM and SF experiments (see selected diffractograms in Figure 4.8). In Figure 4.9, the β- and α”-phases’ X-ray line angular coordinates variations are plotted as functions of the diffractograms’ recording temperature.

The phase composition of TNZ SMA in a stress-free condition at RT presents as follows: β-phase is a main constituent; very weak traces of α”-phase can only be detected in some diffractograms (Figure 4.8). No distinct lines of α- and ω-phases are visible, except (possibly) for a very weak 111_{ω} line. This presentation means that the β→α” transformation temperature range of TNZ is lower than that of TNT SMA.

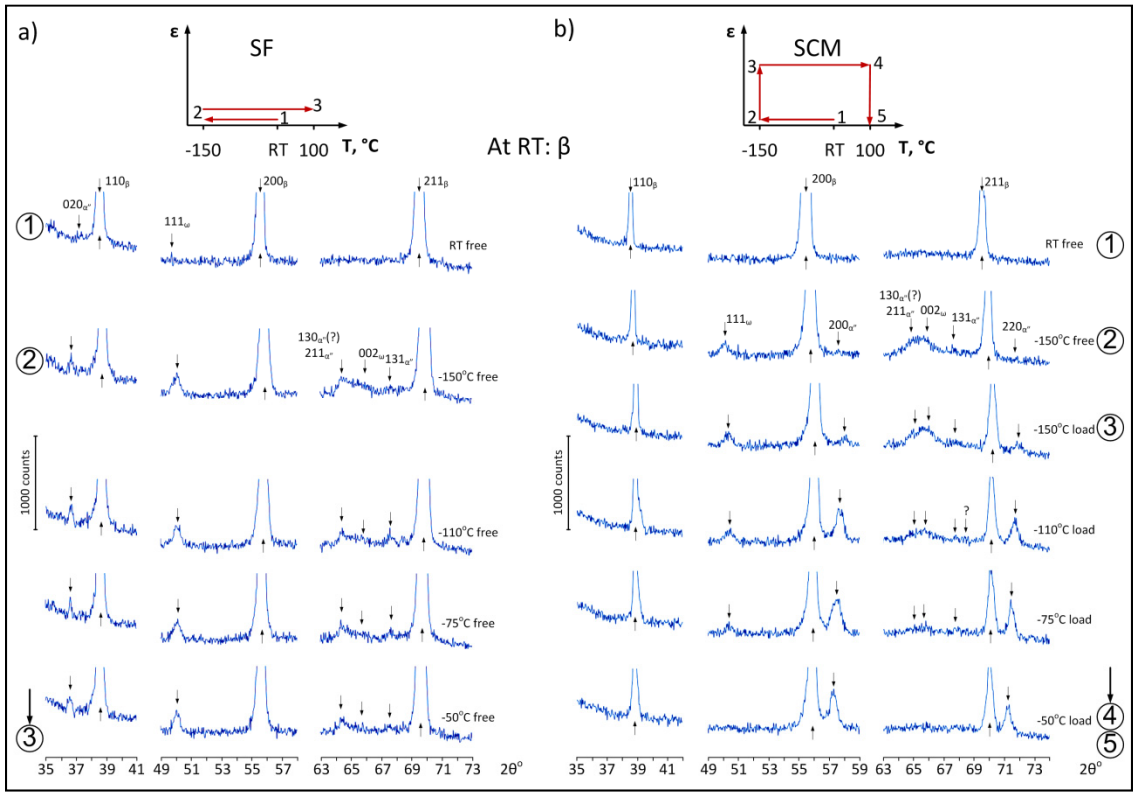

Figure 4.8 Selected X-ray diffractograms of TNZ alloy from (a) SF and (b) SCM experiments. The numbers of the experimental positions 1-3 from the SF and 1-4 from the SCM experiments in Figure 4.2b are indicated

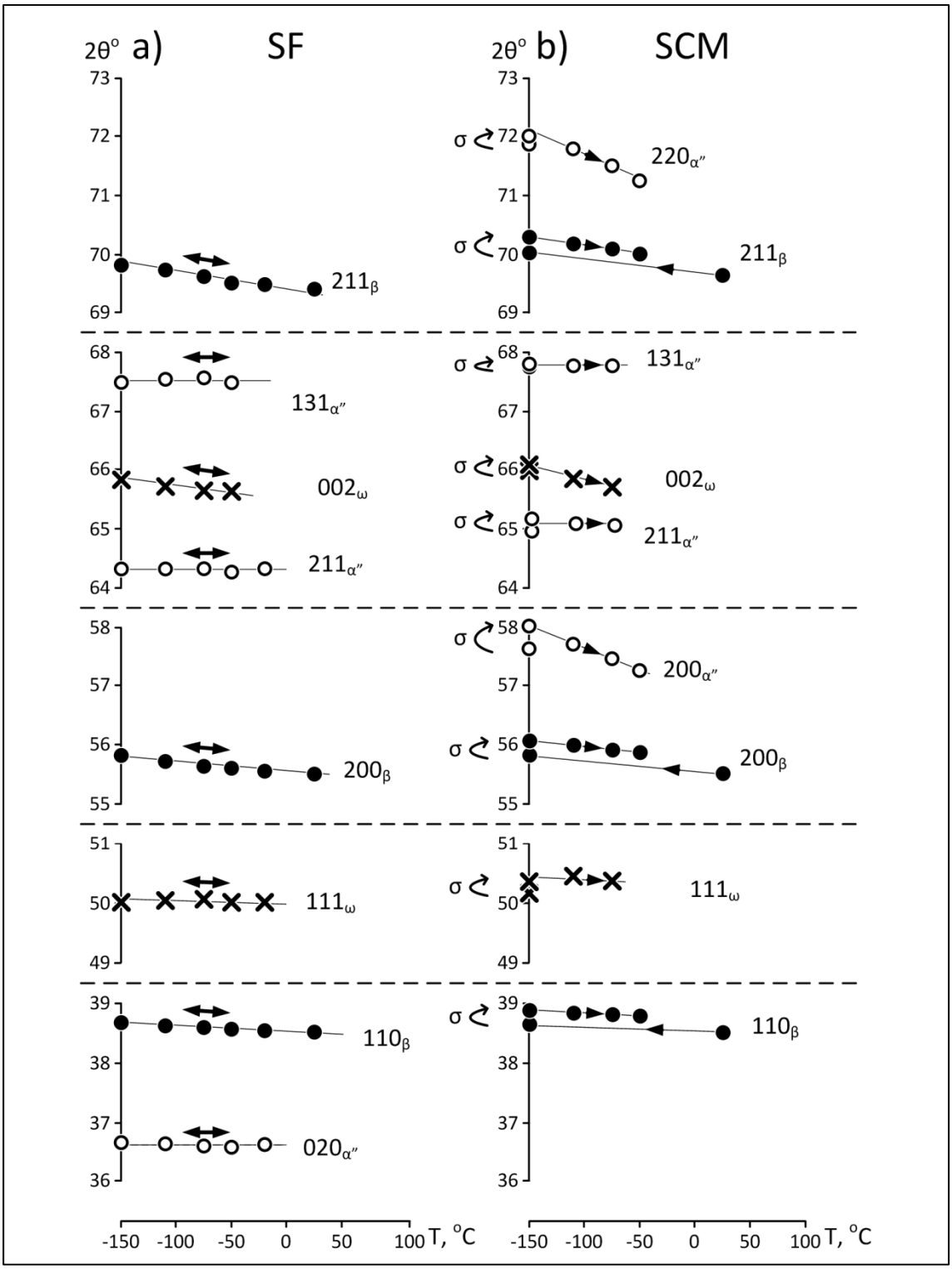

Figure 4.9 TNZ alloy: X-ray line angular coordinates versus diffractogram recording temperature from SF (a) and SCM (b) experiments: ● – β-phase, ○ – α”-phase, × – ω-phase

X-ray line angular positions and phase constituents

During strain-free cooling from RT to -150°C in SF and SCM experiments, α”- and ω-phase lines appear and become stronger, the β-phase and 111_{ω} lines shift to higher θ angles, and the $020_{\alpha''}$ line shifts to lower θ angles (Figure 4.8, Figure 4.9), similar to TNT (Figure 4.5, Figure 4.6). Figure 4.9a shows that under strain-free heating, 020, 211 and 131 α”-phase lines keep their angular positions, whereas β- and ω-phases lines shift to lower θ angles.

Under the influence of an external load applied at -150°C (SCM), an additional quantity of α”-phase appears (see the enhancement of lines $200_{\alpha''}$, $211_{\alpha''}$ and $220_{\alpha''}$ in Figure 4.8b), while the ω-phase 111_{ω} and 002_{ω} line intensity does not change observably, and the X-ray lines of all phases shift to higher θ angles (Figure 4.9b). Under subsequent heating from -150°C, β-phase, ω-phase and $200_{\alpha''}$ and $220_{\alpha''}$ lines shift to lower θ angles, whereas $131_{\alpha''}$ and $211_{\alpha''}$ lines maintain their positions.

Lattice parameters (LPs)

For the TNZ alloy, the α”-martensite and β-phase LPs and their variations in the SF and SCM experiments are shown in Figure 4.10. Their values differ significantly from those of the TNT alloy. The $a_{\alpha''}$ parameters of both alloys are approximately the same, while $b_{\alpha''}$, $c_{\alpha''}$ and $\omega_{\alpha''} = a_{\alpha''} \times b_{\alpha''} \times c_{\alpha''}$, as well as a_{β} and ω_{β} are significantly higher in TNZ alloy. The general impression is that in the -150…-50°C temperature range, the TNZ α”-phase LPs do not vary. Calculations of the α”- and β-phase LPs under loading (SCM and SCP experiments) do not change the situation: the large scatter of α”-phase LPs and their broad confidence range do not allow for clarification of the statistical calculation results (Figure 4.10a). (Note that for better visibility, the experimental points for the SCM and SCP experiments are somewhat shifted along the T scale in Figure 4.10a.)

In light of the conditions mentioned above, it was deemed appropriate to calculate the α”-phase LPs directly from the positions of the corresponding X-ray line peak coordinates,

which are determined with high precision. Thus, the LPs of orthorhombic α”-martensite are calculated as follows: b – from $020_{\alpha''}$, c – from $002_{\alpha''}$, and a – from $200_{\alpha''}$ peak positions. After such refining, a general regularity of martensite LP changes with temperature in TNZ alloy becomes clearer (Figure 4.10b): $a_{\alpha''}$ increases with temperature growth at a rate higher than for a_{β}, i.e., $a_{\alpha''}$ tends to a_{β} with temperature growth; while $b_{\alpha''}$ and $c_{\alpha''}$ ($c_{\alpha''}$ being calculated from the peak position of the $002_{\alpha''}$ line, located at the foot of the 110_{β} peak and therefore reliably determined only in rare cases) are constant within the error limits, and since b_{β}, c_{β} increase with heating, b_{β}, c_{β} come closer to $b_{\alpha''}$, $c_{\alpha''}$.

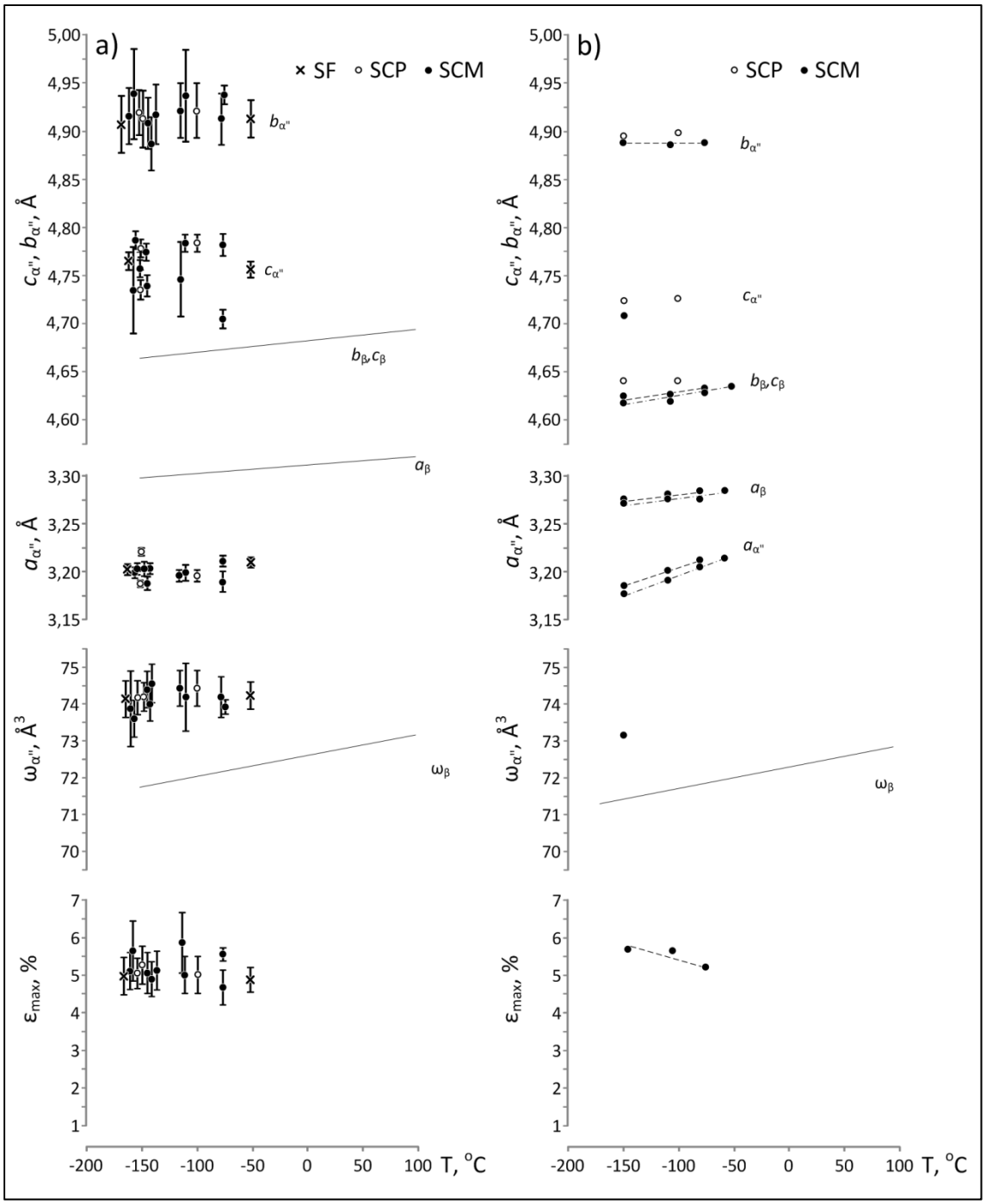

Figure 4.10 TNZ alloy: temperature dependence of the α”-phase LPs and ε_{max} from SF, SCM and SCP experiments: a) calculated using the least squares method and b) calculated directly from the $020_{\alpha''}$, $002_{\alpha''}$ and $200_{\alpha''}$ line $2\theta_{hkl}$ coordinates

4.5.2 Phase transformation features

To estimate phase transformation and reorientation features, α”- and ω-phase X-ray line integral intensities were measured, where it was possible with sufficient precision. Their temperature dependences for the SF and SCM experiments are shown in Figure 4.11 (TNT) and in Figure 4.12 (TNZ).

Under strain-free cooling of TNT from RT to -150°C in SF and SCM experiments, the of α”-phase content somewhat increases. Loading at -150°C results in a further increase of the α”-phase content and in its subsequent reorientation during heating. In the SCP experiment (not shown), application of external stress at RT leads to insignificant changes in α”-phase quantity, followed by its slight increase during cooling. The α”-phase content evolutions during heating in the SCP and SCM experiments are similar.

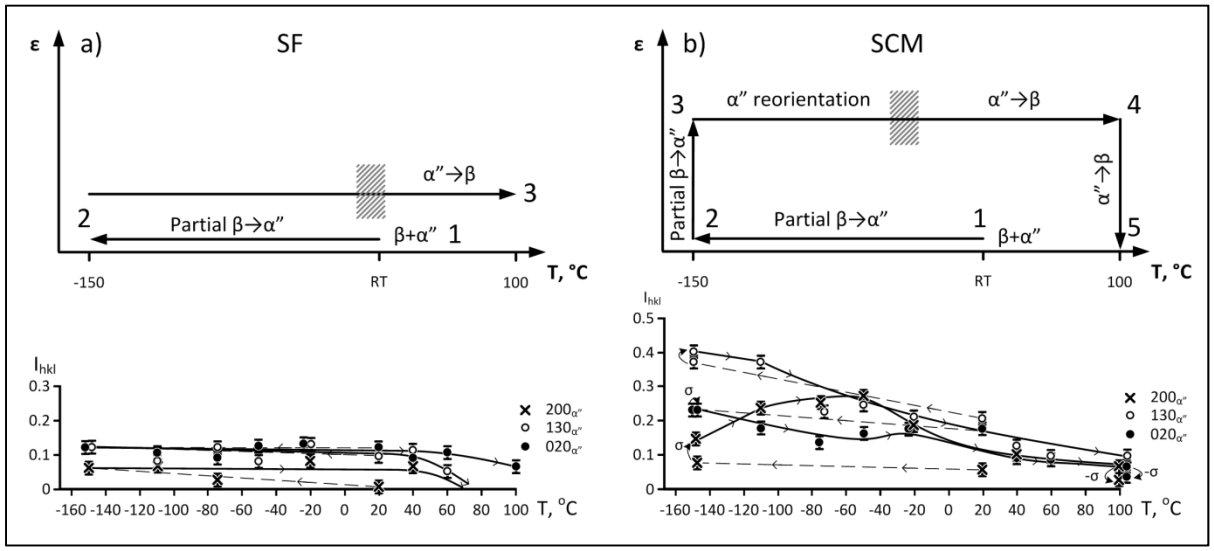

Figure 4.11 TNT: Selected X-ray diffraction lines integral intensities versus recording temperature from SF (a) and SCM (b) experiments. The shadowed areas indicate the starting temperatures of the reverse α”→β transformation

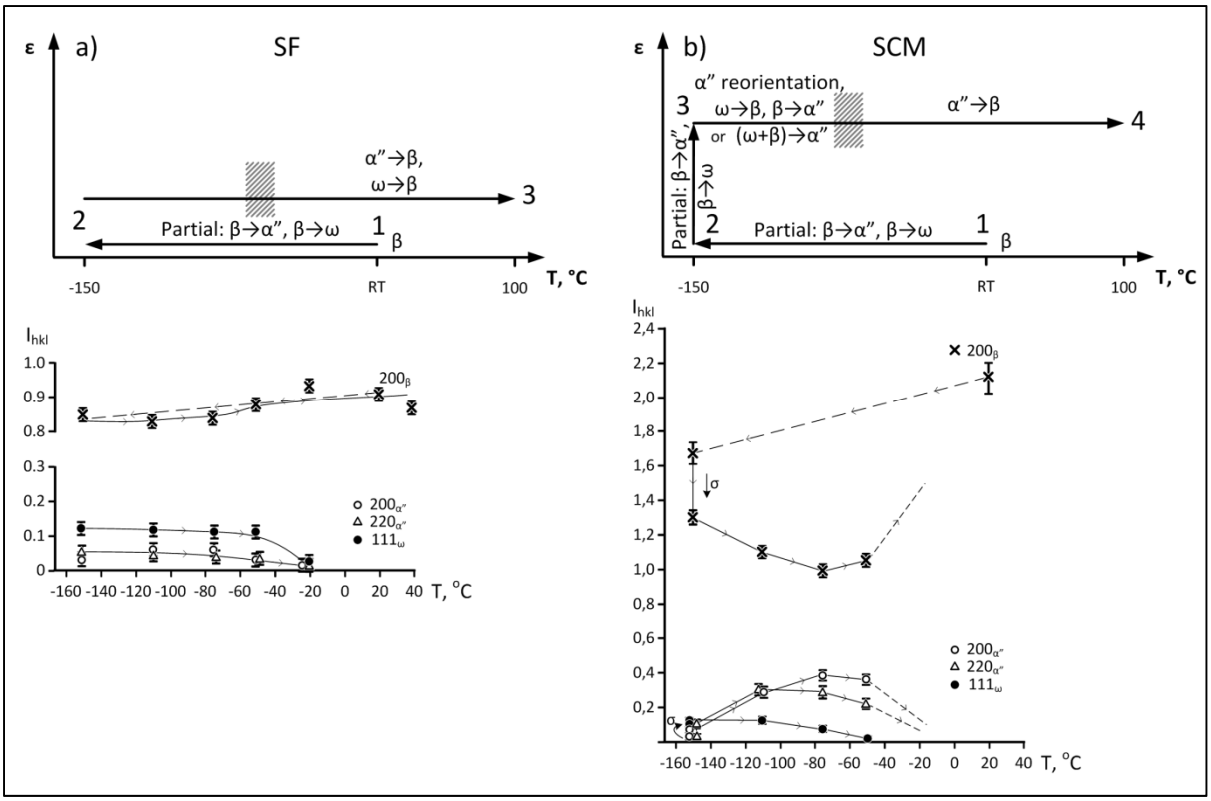

Figure 4.12 TNZ: X-ray diffraction line integral intensities versus recording temperature from SF (a) and SCM (b) experiments. The shadowed areas indicate starting temperatures of the reverse α”→β and ω→β transformations

In all three TNZ alloy experiments, cooling results in the appearance of α”- and ω-phase lines. Upon heating in the SF experiment, α”- and ω-phase contents do not change significantly for temperatures up to -75°C, and then they rapidly and simultaneously decrease to sink into the background at -20°C; i.e., they show an independent and simultaneous weakening with temperature increase.

During heating under load in the SCM experiment, the ω-phase quantity decreases monotonically, the quantity of β-phase first decreases (up to -75°C) and then increases, while the quantity of α”-phase shows a mirror behavior; it augments up to -75°C and then diminishes. Note that at -50°C, no ω-phase lines can be observed, while the $200_{\alpha”}$ and $220_{\alpha”}$ lines are still clearly visible.

4.5.3 Reversible inhomogeneous distortions

Figure 4.13 illustrates the temperature and stress effects on the β-phase X-ray line width (B_{hkl}^{β}) in TNZ and TNT alloys during SF, SCP and SCM experiments. Since this parameter reflects the presence of inhomogeneous microstresses of various origins distributed in an alloy, it can also reflect the presence of martensitic transformations in the studied materials. As B_{hkl}^{β} variations in experiments with the TNZ alloy are much more pronounced than they are with the TNT alloy, we will limit our explanations to this material.

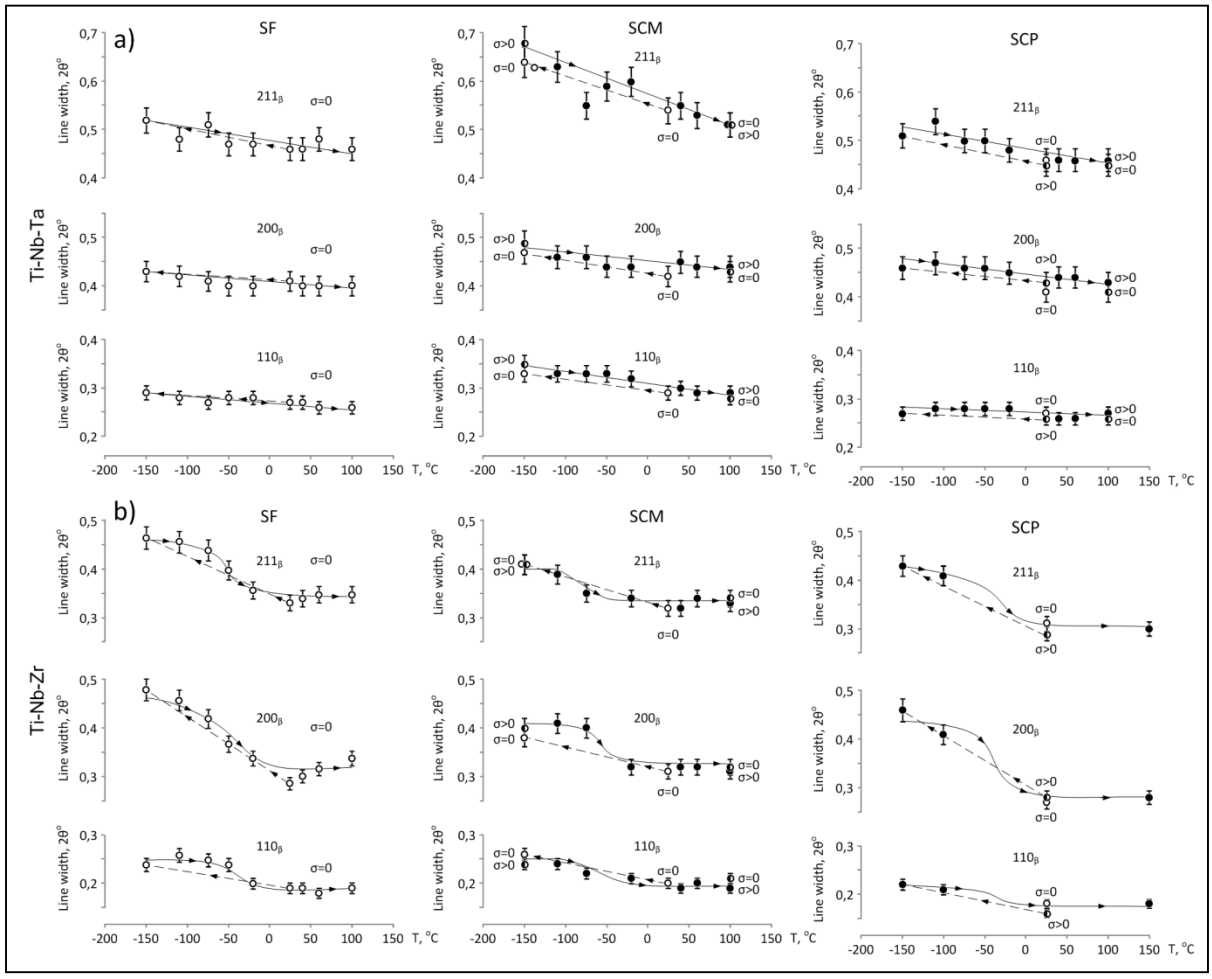

Figure 4.13 Beta-phase X-ray line width versus recording temperature in SF, SCP and SCM experiments for a) TNT and b) TNZ alloys

Under strain-free cooling of TNZ alloy to -150°C (Figure 4.13b), a distinct widening of the β-phase X-ray lines accompanies direct β→α" transformation. Under heating up to -100°C, the B_{hkl}^{β} values remain almost unchanged, but in the -75…-20°C temperature range, they decrease down to the initial (before cooling) values due to reverse β→α" transformation. From that point (-20°C), they stay constant up to 100°C.

In the SCM experiment, strain-free cooling causes the same X-ray line widening as in the SF experiment (Figure 4.13b). Loading at -150°C does not significantly affect the B_{hkl}^{β} values of the already significantly-widened β-phase lines, thus masking additional martensite formation and reorientation under stress. Upon subsequent heating under load, B_{hkl}^{β} values decrease down to their initial values similarly to their behavior in the SF experiment. Finally during the SCP experiment, B_{hkl}^{β} values evolve in a similar manner to their behavior in the SF and SCM experiments (Figure 4.13b).

The β-phase {211} X-ray line profile changes during the SCP and SCM experiments are shown in more detail in Figure 4.14. Obvious 211_{α_1} - 211_{α_2} doublet splitting is observed at RT in both experiments (Figure 4.14a,b). Free cooling to -150°C (SCM) leads to the disappearance of the visible doublet splitting due to strong overlapping of the 211_{α_1} and 211_{α_2} singlets, which widen under the effect of martensitic transformation (Figure 4.14a). Loading at -150°C does not significantly affect the 211_{β} peak's shape, whereas heating to -20°C (end of the reverse martensitic transformation) results in the 211_{α_1} - 211_{α_2} doublet splitting reappearance. It should be noted that the non-perfect initial α_1-α_2 doublet splitting is due to the existence of a non-recrystallized, nanosubgrained β-phase structure that causes a pronounced widening of the α_1 and α_2 singlets.

Loading at RT (SCP) does not affect 211_{α_1} - 211_{α_2} doublet splitting (Figure 4.14b). Martensite formation during cooling results in the disappearance of doublet splitting, followed by its recovery after completion of the reverse transformation during heating back to +100°C under load (Figure 4.14b).

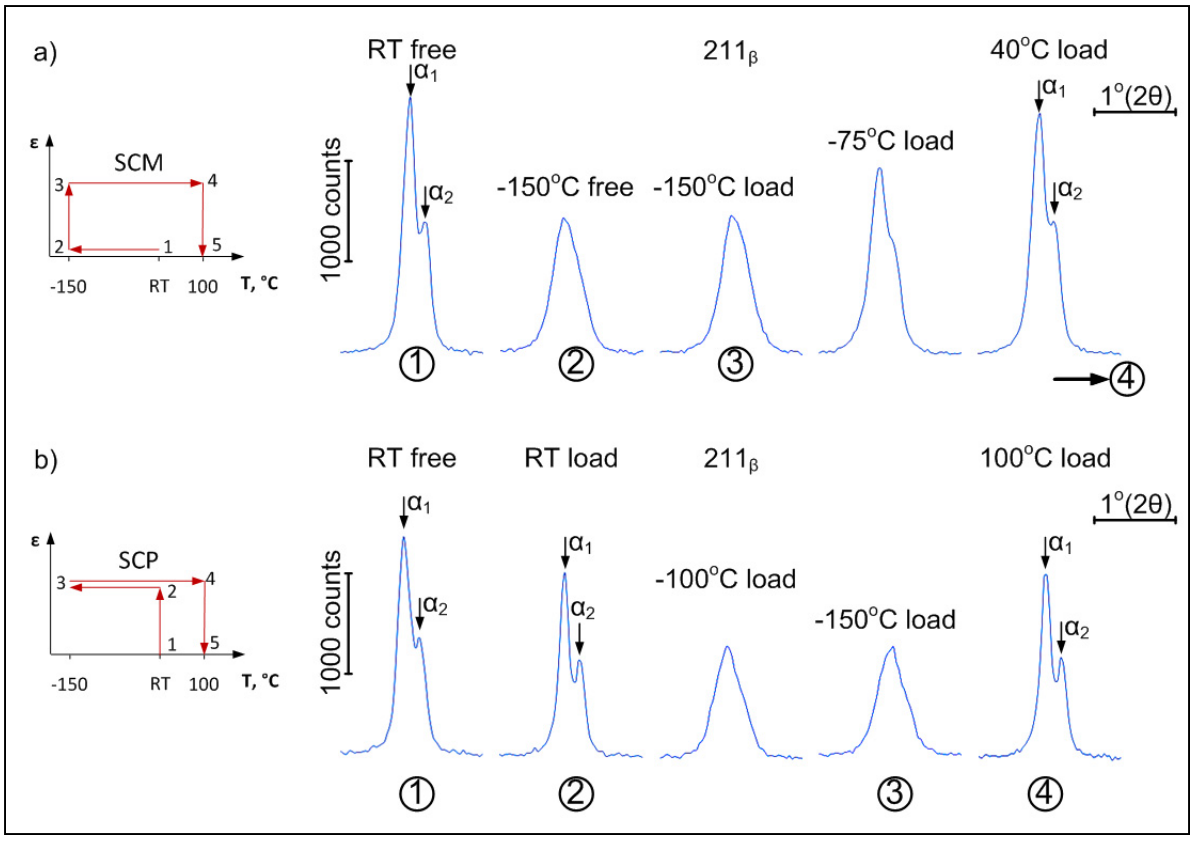

Figure 4.14 Sequential changes of the 211_{β} peak profile with temperature and stress in TNZ alloy during SCM (a) and SCP (b) experiments

4.6 Discussion

4.6.1 Structure transformations and crystal lattice changes

The abovementioned reversible anisotropic X-ray line shifts on heating are consequences of the orthorhombic α”-martensite LPs changes towards the “genetically” linked parent β-phase LPs. Indeed, putting aside the temperature-related variations of the β-phase LPs, it can be observed that the $a_{\alpha''}$ and $b_{\alpha''}$ (α”-phase) tend to a_{β} and b_{β} (parent β-phase), whereas the $c_{\alpha''}$ and c_{β} are very close to each other (Figure 4.7a).

From the comparison of Figure 4.7a and Figure 4.7b, it can be seen that (within the limits of this study) loading does not affect the α”-phase LPs’s *inter se* proportions, or the proportions

between the LPs of α”- and β-phases. When temperature increases from -150°C to RT, the LPs of both phases vary so that the maximum transformation lattice strain ε_{max} (ε_2, tension) decreases from 3.5 to 2.5%. The ε_{max} value at RT correlates well with the ε_{max} calculated for the close composition TNT alloy [1, 36, 37]. For an isotropic TNT polycrystal, the theoretical ε_{max} is reduced to 3.2% at -150°C and to 2.3% at RT, in accordance with [38].

Maximum recoverable strain for TNZ alloy is significantly higher than for TNT alloy, despite the identical atomic concentration of the third element in both materials. Even though it appeared impossible to assess the temperature dependence of ε_{max} in statistical experiments for TNZ alloy (Figure 4.10a), this task became feasible from the $020_{\alpha''}$ and 110_{β} peak positions’ measurements (Figure 4.10b). The following trend was observed: under heating in the -150…-75°C temperature range, ε_{max} decrease from 5.73 to 5.26% (from 5.2 to 4.7% for an isotropic TNZ polycrystal).

Now compare LPs and their temperature dependences for TNZ (Figure 4.7) and TNT (Figure 4.10) alloys. On one side, $a_{\alpha''}$ parameters of both alloys are approximately identical. On the other side, $b_{\alpha''}$, $c_{\alpha''}$ and $\omega_{\alpha''} = a_{\alpha''} \times b_{\alpha''} \times c_{\alpha''}$, as well as a_{β} and ω_{β} for TNZ are larger than for TNT. Furthermore, considering the slopes of the b_{β}, c_{β} temperature dependencies on heating, $b_{\alpha''}$ and $c_{\alpha''}$ for both alloys tend to converge to b_{β}, c_{β}, but this trend is less pronounced for TNZ than for TNT.

4.6.2 Phase transformation features

Since during strain-free (SF) heating, the α”- and ω-phase X-ray lines weaken independently and simultaneously (Figure 4.12), it is reasonable to assume that reverse ω→β and α”→β transformations also take place independently.

On the contrary, during heating under stress (SCM), ω→β + β→α”, or β+ω→α”, transformations occur in the lower part of the heating range [23, 25, 39], whereas in the upper part of this range, the reverse α”→β transformation takes place. Such a two-part

partition of the heating range correlates well with the Clausius-Clapeyron relationship which establishes a stress-temperature dependence of the critical transformation temperatures. In accordance with this relationship, the A_s-A_f range for the martensite formed and reoriented under stress is higher than the temperature range of martensite reorientation under stress [40, 41] (Figure 4.15). The β→α" transformation behavior during heating under stress resembles isothermal martensitic transformation kinetics which can be observed in high-carbon steel [42] and even in Ti-Ni SMA [43]. A distinct increase in the α"-phase content during heating below -75°C may be a consequence of lower transformation yield stress in the range of incomplete β→α" martensitic transformation below the M_s temperature (compare σ at T_{i1} and T_{i2}, Figure 4.15).

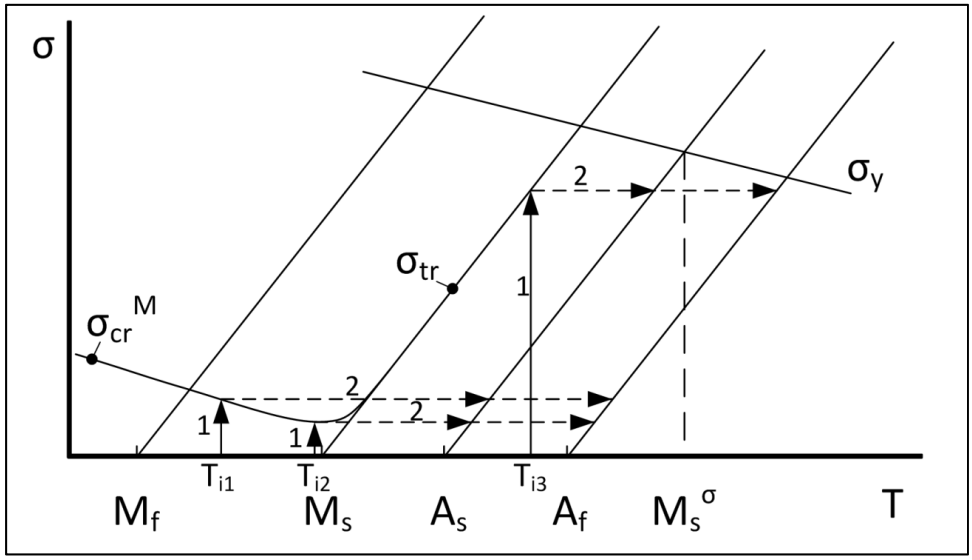

Figure 4.15 Schematic representation of the critical temperatures of thermoelastic martensitic transformations under stress. σ_{tr} – transformation yield stress, σ_{cr}^{M} – critical stress for martensite reorientation, σ_y – dislocation yield stress. 1 – loading, 2 – heating under load

If the I_{hkl} changes in Figure 4.12b are compared to the corresponding stress (σ) variations under constrained (ε=1%) heating from -150°C (adapted from [11]), one can observe that the recovery stress generation takes place mainly above -50°C (Figure 4.16). Consequently, the recovery stress generation in TNZ alloy is the result of constrained α"→β transformation,

and is not caused by ω→β transformation. This is not surprising, as β↔ω transformation mechanisms involve the reversible shuffling of atomic planes', which does not distort the β unit cell [13], and therefore does not result in recovery stress generation.

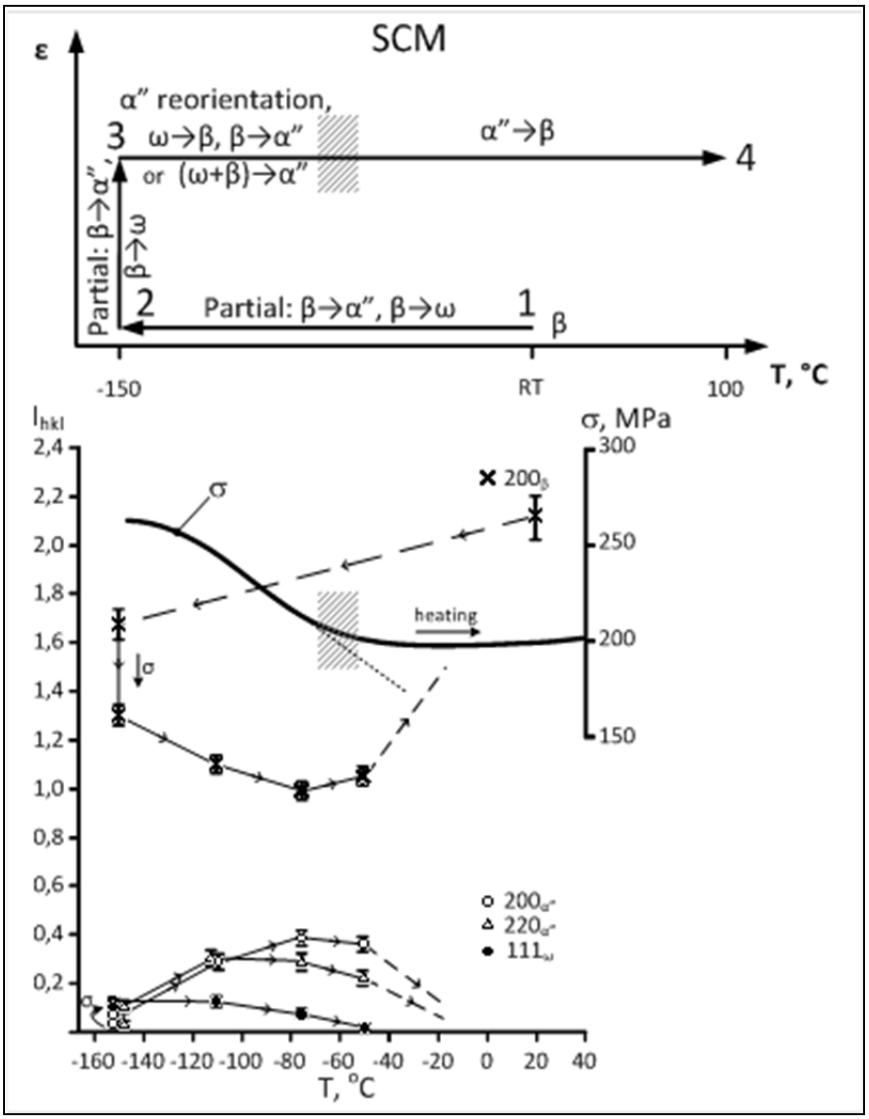

Figure 4.16 Integral intensity of the selected X-ray diffraction lines versus testing temperature from SCM experiment. For comparison, stress as a function of temperature from constant-strain temperature scanning experiment under ε_i=1 % induced strain [11] is shown. Shadowed areas indicate the onset temperatures of the reverse α"→β transformations under stress

4.6.3 Reversible inhomogeneous distortions

An interesting problem that can be solved using the results of this *in situ* experiment, is the determination of a cause of the reversible inhomogeneous crystal lattice distortions during SMA loading and unloading described in [25]. It has been supposed that the observed reversible β-phase X-ray lines widening during isothermal loading-unloading of Ti-Nb and Ti-Nb-Mo SMAs [24, 25] was a result of deformation-induced inhomogeneous microstress distribution in differently-oriented grains of the polycrystalline material [25]. Note that the reversible X-ray line widening can be observed in [24] for both β-phase and α”-phase X-ray lines.

Our previous *in-situ* X-ray diffraction study [38] indicated that thermoelastic B19'- and R-martensite formation in Ti-Ni SMA during stress-free cooling was accompanied by pronounced B2-austenite, R-phase and B19’-martensite X-ray line widening. This widening completely disappeared after completion of the reverse transformation to B2-austenite upon heating, with the restoration of the initial B2 X-ray line width. Such recoverable X-ray line width change was explained by the accumulation of lattice distortions due to the preservation of coherent bonds between initial- and final-phase lattices and their disappearance as a result of the reverse transformation of thermoelastic martensite. This suggests that thermoelastic α”-martensite formation and reverse transformation during loading-unloading cycle are likely causes for the reversible widening of β-phase X-ray lines observed in this study.

Indeed, from the SF experiment (Figure 4.13) where no stress is applied, the reversible X-ray line width variations can only be caused by β↔α” thermoelastic martensitic transformation. Moreover, loading in a β+α” state and unloading in a β state do not result in B_{hkl}^{β} changes; the latter only occur in the β↔α” transformation range regardless of the stress application conditions. These results are coherent with those for B2↔R↔B19’ thermoelastic transformation in Ti-Ni SMA [38].

Under conditions of SF, SCM and SCP experiments, reversible changes in B_{hkl}^{β} are similar for both alloys, despite the different α”-phase contents and, therefore, different initial B_{hkl}^{β} (Figure 4.13). Considering the prefect correlation of the 211_{β} doublet splitting (Figure 4.14) and the X-ray lines' width changes with temperature (Figure 4.14), it can definitely be concluded that inhomogeneous lattice microstresses related to the direct β→α” (thermally or stress-induced) and reverse α”→β transformations represent the only reasons for the reversible X-ray line width variations. The coherency of β and α” lattices is a primary cause of this phenomenon.

4.7 Conclusions

1. During the cooling and heating of TNT and TNZ alloys, reversible anisotropic α''-phase X-ray line shifts are observed. On heating, α''-phase LPs strive towards corresponding (“genetically” linked) parent β-phase LPs. These variations can be observed regardless of the absence or the presence of external stresses, being less pronounced for TNZ than for TNT alloys.

2. In the -150^{o}C…RT heating range, crystallographic resource of recovery strain decreases from 5.7 to 4.5% (TNZ) and from 3.5 to 2.5% (TNT) following the single-crystal calculation approach.

3. Under strain-free cooling, an additional quantity of α”-phase forms in TNT, while both “athermal” α”- and ω-phases form in TNZ. Cooling under stress of both alloys is accompanied by an increase in the quantity and reorientation of α”-phase. Application of an external load at -150^{o}C results in a certain growth of α”-phase content, while the quantity of ω-phase (TNZ) does not seem to be affected.

4. Strain-free heating of TNT alloy results in reverse α”→β transformation, whereas during heating under stress, α”→β transformation is preceded by α”-phase reorientation. Strain-free heating of TNZ alloy results in simultaneous α”→β and

ω→β transformations, whereas heating under stress results in sequential two-step transformation: ω→β + β→α” (or β+ω→α”), followed by α”→β.

5. The appearance and disappearance of inhomogeneous microstresses, either under load at constant temperature or during strain-free or constant-strain cooling-heating cycles are exclusively related to the formation and disappearance of thermoelastic α’’-martensite in the parent β-phase.

4.8 Acknowledgements

This work was carried out with financial support from the Ministry of Economic Development of Quebec, the National Science and Engineering Research Council of Canada and the Ministry of Education and Science of the Russian Federation. The authors wish to thank Dr. M. Petrzhik from NUST “MISIS” for useful discussions.

4.9 References

[1] Petrzhik MI, Fedotov SG. Thermal stability and dynamics of martensite structure in Ti-(Ta, Nb) alloys. Proceedings of the XVI Conference on Applied Crystallography; 1994 August 22-6; Cieszyn, Poland. Singapore: World Scientific Publishing Company; 1995.

[2] Niinomi M, Hanawa T, Narushima T. Japanese research and development on metallic biomedical, dental and healthcare materials. JOM 2005;57:18-24

[3] Kim JI, Kim HY, Inamura T, Hosoda H, Miyazaki S. Shape memory characteristics of Ti-22Nb-(2-8)Zr (at.%) biomedical alloys. Mater Sci Eng A2005;403:334-9

[4] Ping DH, Ciu CY, Yin FX, Yamabe-Matarai Y. TEM inxestigations on martensite in Ti-Nb-based shape memory alloys. Scr Mater 2006;54:1305-10.

[5] Kim HY, Kim JI, Inamura T, Hosoda H, Miyazaki S. Effect of thermo-mechanical treatment on mechanical properties and shape memory behavior of Ti-(26-28) at.%Nb alloys. Mater Sci Eng A 2006;438-440:839-43.

[6] Kim HY, Hashimoto S, Kim JI, Inamura T, Hosoda H, Miyazaki S. Effect of Ta addition on shape memory behavior of Ti-22 at.%Nb alloy. Mater Sci Eng A 2006;417:120-8.

[7] Miyazaki S, Kim HY, Hosoda H. Development and characterization of Ni-free Ti-base shape memory and superelastic alloys. Mater Sci Eng A 2006;438-440:18-24.

[8] Park JB, Lakes RS. Biomaterials: an Introduction. 3rd ed. New York: Springer; 2007.

[9] Niinomi M, Akanori T, Nakai M. In situ X-ray analysis of mechanism of non-linear superelastic behavior of Ti-Nb-Ta-Zr system beta-type alloy for biomedical applications. Mater Sci Eng C 2008;28:406-13.

[10] Yoneyama T, Miyazaki S, editors. Shape Memory Alloys for Biomedical Applications. Cambridge: Woodhead Publishing; 2009.

[11] Brailovski V, Prokoshkin S, Gauthier M, Inaekyan K, Dubinskiy S, Petrzhik M, Filonov M. Bulk and porous metastable beta Ti-Nb-Zr(Ta) alloys for biomedical applications. Mater Sci Eng C 2011;31:643-57.

[12] Bagariatskii YuA, Nosova GI, Tagunova TV. Factors in the formation of metastable phases in titanium-based alloys. Sov Phys Dokl 1959;3:1014-18.

[13] Collings EW. The Physical Metallurgy of Titanium Alloys. ASM: Metals Park; 1984.

[14] Geetha M, Singh AK, Gogia AK, Asokamani R. Effect of thermomechanical processing on evolution of various phases in Ti-Nb-Zr alloys. J Alloys Compd 2004;384:131-44.

[15] Miyazaki S. Mechanical behavior, shape memory effect, pseudoelasticity in Ti-based alloys. Plenary Lecture. 9th European Symposium on Martensitic Transformations, ESOMAT 2012, 2012 September 09-16; Saint-Petersburg, Russia.

[16] Lukas P, Sittner P, Neov D, Novak V, Ludovyy D, Tovar M. R-phase phenomena in neutron diffraction investigations of thermomechanically loaded NiTi polycrystals. Mater Sci Forum 2002;404-407:835-40.

[17] Prokoshkin SD, Korotitskiy AV, Tamonov AV, Khmelevskaya IY, Kartseva EA. Studies of the martensite crystal lattice in binary Ti-Ni alloy using in situ time-of-flight neutronography under temperature and stress changes. Phys Met Metallogr 2004;98(1):37-43.

[18] Sittner P, Lukas P, Novak V, Daymond R, Swallowe GM. In situ neutron diffraction studies of martensitic transformations in NiTi polycrystals under tension and compression stress. Mater Sci Eng A 2004;378:97-104.

[19] Prokoshkin S, Korotitskiy A, Tamonov A, Khmelevskaya I, Brailovski V, Turenne S. A comparative X-ray and time-of-flight neutron diffraction studies of martensite crystal lattice in stressed and unstressed binary Ti-Ni alloys. Mater Sci Eng A 2006;438-440:549-52.

[20] Sittner P, Sedlak P, Landa M, Novak V, Lukas P. In situ experimental evidence on R-phase related deformation processes in activated NiTi wires. Mater Sci Eng A 2006;438-440:579-84.

[21] Sittner P. Revealing deformation mechanisms in SMAs by in-situ X-ray and diffraction methods. Plenary lecture. 9th European Symposium on Martensitic Transformations, ESOMAT 2012, 2012 September 09-16; Saint-Petersburg, Russia.

[22] Khromova LP, Dyakonova NB, Rodionov YuL, Yudin GV, Korms I. Martensitic Transformation, Thermal Expansion and Mechanical Properties of Titanium–Niobium Alloys. J Phys IV 2003;112:1051–4.

[23] D'yakonova NB, Lyasotskii IV, Rodionov YuL. Orthorhombic martensite and the ω phase in quenched and deformed titanium alloys with 20-24 at % Nb. Russ Metall (Metally) 2007;1:51-8.

[24] Tahara M, Kim HY, Hosoda H, Miyazaki S. Cyclic deformation behavior of a Ti–26 at.% Nb alloy. Acta Mater 2011;59:1464-73.

[25] Al-Zain Y, Kim HY, Koyano T, Hosoda H, Nam TH, Miyazaki S. Anomalous temperature dependence of the superelastic behavior of Ti-Nb-Mo alloys. Acta Mater 2011;59:1464-73.

[26] Lopes ESN, Cremasco A, Afonso CRM, Caram R. Effects of double aging heat treatment on the microstructure, Vickers hardness and elastic modulus of Ti-Nb alloys. Mater Charact 2011;6:673-80.

[27] Prokoshkin SD, Korotitskiy AV, Gundyrev VM, Zeldovich VI. Low-temperature X-ray diffraction study of martensite lattice parameters in binary Ti-Ni alloys. Mater Sci Eng A 2008;481-482:489-93.

[28] Brailovski V, Prokoshkin S, Inaekyan K, Dubinskiy S, Gauthier M. Mechanical properties of thermomechanically processed metastable beta Ti-Nb-Zr alloys for biomedical applications. Mater Sci Forum 2012;706-709:455-60.

[29] Dubinskiy S, Brailovski V, Prokoshkin S, Pushin V, Inaekyan K, Sheremetyev V, et al. Structure and properties of Ti-19.7Nb-5.8Ta shape memory alloy subjected to

thermomechanical processing including aging. J Mater Eng Perform 2013; published online 16.04.2013, DOI: 10.1007/s11665-013-0555-6.

[30] Prokoshkin S, Brailovski V, Korotitskiy A, Inaekyan K, Dubinskiy S, Filonov M, Petrzhik M. Formation of nanostructures in thermomechanically treated Ti-Ni and Ti-Nb-(Zr,Ta) SMAs and their roles in martensite crystal lattice changes and mechanical behavior. J Alloys Compd 2012, doi: 10.1016/j.jallcom.2011.12.153.

[31] Dubinskiy S, Brailovski V, Prokoshkin S, Inaekyan K, In-situ X-ray study of phase transformations in Ti-Nb-based SMA under variable stress-temperature conditions: Preliminary results. Mater Sci Forum 2013;738-739:87-91.

[32] Nelson JB, Riley DP. An experimental investigation of extrapolation methods in the derivation of accurate unit-cell dimensions of crystals. Proc Phys Soc 1945;57:160-77.

[33] Prokoshkin SD, Korotitskiy AV, Brailovski V, Turenne S, Khmelevskaya IYu, Trubitsyna IB. On the lattice parameters of phases in binary Ti-Ni shape memory alloys. Acta Mater 2004;52(15):4479-92.

[34] Sun F, Hao YL, Novak S, Gloriant T, Laheurte P, Prima F. A thermo-mechanical treatment to improve the superelastic performances of biomedical Ti-26Nb and Ti-20Nb-6Zr (at.%) alloys. J Mech Behav Biomed Mater 2011;4:1864-72.

[35] Prokoshkin SD, Brailovski V, Turenne S, Khmelevskaya IY, Korotitskiy AV, Trubitsyna IB. On the lattice parameters of the B19'-martensite in binary Ti-Ni shape memory alloys. Phys Met Metallogr 2003;96(1):55-64.

[36] Zhukova YuS, Petrzhik MI, Prokoshkin SD. Evaluation of the crystallographic resource of strain at reversible martensitic transformation β – α" in titanium alloys with shape memory effect. Russ Metall (Metally) 2010;11:1056-62.

[37] Kim HY, Sasaki T, Okutsu K, Miyazaki S. Texture and shape memory behavior of Ti-22Nb-6Ta alloy. Acta Mater 2006;54:423-33.

[38] Prokoshkin SD, Korotitskiy AV, Brailovski V, Inaekyan KE, Dubinskiy SM. Crystal lattice of martensite and the reserve of recoverable strain of thermally and thermomechanically treated Ti-Ni shape memory alloys. Phys Met Metallogr 2011;112(2):170-87.

[39] Inamura T, Hosoda H, Kim HY, Miyazaki S. Antiphase boundary-like stacking fault in α”-martensite of disordered crystal structure in β-titanium shape memory alloy. Philos Mag 2010;90(25):3475-98.

[40] Otsuka K, Wayman CM, editors. Shape Memory Materials. Cambridge: Cambridge University Press; 1999.

[41] Brailovski V, Prokoshkin S, Terriault P, Trochu F, editors. Shape Memory Alloys: Fundamentals, Modeling and Applications. Montreal: ETS Publishing; 2003.

[42] Prokoshkin SD, Karabasova LV, Kaputkin DE. [Dilatometric effects at martensitic transformations in high-carbon steels]. Phys Met Metallogr 1989;67(3):622-4. Russian.

[43] Prokoshkin SD, Khmelevskaya IY, Dobatkin SV, Trubitsyna IB, Tatyanin EV, Stolyarov VV, Prokofiev EA. Alloy composition, deformation temperature, pressure and post-deformation annealing effects in severely deformed Ti-Ni based shape memory alloys. Acta Mater 2005;53:2703-14.

CONCLUSIONS

The objectives of this project were: (1) to study the interrelations between the composition, microstructure and functional properties of superelastic Ti-Nb-Zr and Ti-Nb-Ta alloys and (2) to maximize their functional properties under cyclic loading.

1. As far as the first objective is concerned, it was shown that moderate cold deformation ($e \approx 0.3$) of Ti-Nb-Zr and Ti-Nb-Ta alloys forms well-developed dislocation substructure in β-phase. On the other hand, severe cold deformation ($e \approx 2$) results in the formation of a mixed well-developed dislocation substructure and nanocrystalline structure in β-phase. Furthermore, post-deformation annealing at temperatures under 450^{o}C (1h) does not significantly affect the β-phase structure in the two alloys. Annealing at temperatures above 450^{o}C after $e \approx 0.3$ leads to a successive formation in β-phase of a nanosubgrained substructure (500^{o}C) and a submicron-sized structure (600^{o}C). Recrystallization starts in the 600 – 700^{o}C temperature range.

2. A miniature custom tensile stage is developed and used for a strain-controlled *in situ* X-ray diffraction study in the -150...+100^{o}C temperature range using the *TTK450* thermal chamber of a *PANalytical X'Pert Pro* diffractometer. Lattice parameters of β- and α"-phases are then calculated with and without load under temperature scanning conditions, and the results of this study showed the following:

    a) For both alloys, upon heating up to M_s, the lattice parameters of α"-phase evolve in the direction of the corresponding "genetically-linked" lattice parameters of the parent β-phase, and the higher the testing temperature, the lower the crystallographic resource of recoverable strain;

    b) The crystallographic resource of recoverable strain of Ti-Nb-Zr alloy is twice as large as that of Ti-Nb-Ta alloy at the same temperature;

c) Loading in the martensitic state results in additional α”-phase formation and in α”-phase reorientation;

d) Upon heating of Ti-Nb-Zr alloy, transformation sequences differ depending on the test conditions: (β+ω)→α” transformation precedes α”→β transformation, whereas without load, both ω→β and α”→β transformations occur in parallel and independently;

e) The observed reversible β-phase X-ray line widening is exclusively caused by α”↔β stress and temperature-induced thermoelastic martensitic transformation.

In respect to the second objective of this project, it was shown that the biomechanical compatibility of an alloy (low Young's modulus and superelasticity with small residual strain after multi-cycle loading) could be improved if an "optimum" thermomechanical processing is applied. For Ti-Nb-Zr alloy, the optimum processing implies cold deformation (e=0.37) followed by post-deformation annealing at 600^{o}C, 30 min. For Ti-Nb-Ta alloy, the optimum processing implies cold deformation (e=0.37) followed by post-deformation annealing at 500^{o}C, 1h. These processing conditions result in the formation, in both alloys, of nanosubgrained structures with ~100 nm subgrain size. For Ti-Nb-Ta alloy, further improvement can be obtained by means of additional low-temperature ageing (300^{o}C, 1h). This last heat treatment results in the precipitation of well-dispersed nanosized (~10 nm) ω-phase coherent particles, leading to significant material hardening, and, therefore, to higher multi-cycle mechanical resistance.

RECOMMENDATIONS

From the authors' standpoint, the current project can be continued in the following major directions:

- Development of Ti-Nb-based SMA with higher resource of recoverable strain (≈7.5%) for biomedical and general technical purposes not only as materials with a superelasticity effect but also as materials with a shape memory effect;

- Development of quaternary Ti-Nb-Zr-Ta SMA for biomedical application, which will take advantage of both Ti-Nb-Zr and Ti-Nb-Ta SMA;

- Development of Ti-Nb-based superelastic porous material, which better mimics living bone than the bulk material;

- More in-depth low-temperature *in situ* X-ray analysis of crystal structure of phases, structure and phase transformations under variable strain-temperature conditions in nickel-free Ti-based SMA.

However, there are some points to clarify before going on to the next step of research. A higher initial cold deformation technique (for example: equal-channel angular pressing) can be tried to obtained nanocrystalline material, which will probably additionally increase the functional properties. ASTM-like classical fatigue testing is required for more reliable fatigue resistance evaluation. Dilatometric analysis should be performed for precise martensitic temperature range evaluation and additional study of phase transformation features. *In situ* X-ray diffraction analysis should be optimized: for example, maximum applicable tensile strain should be increased to at least 2%, and additional scanning points should be added upon temperature scanning and loading steps.

ANNEX I

ARTICLE: *IN-SITU* X-RAY STUDY OF PHASE TRANSFORMATIONS IN Ti-Nb-BASED SMA UNDER VARIABLE STRESS-TEMPERATURE CONDITIONS: PRELIMINARY RESULTS

Summary

The Annex contains a paper which describes the design, working principle and validation of a custom-made tensile stage for the *TTK450* thermal chamber of a *PANalytical X'Pert PRO* diffractometer. This stage is powered by a Ti-Ni SMA actuator, which makes it possible to fit it within a small volume of thermochamber and successfully use it in the -150...+100^{o}C temperature range. The maximum applied strain is about 1%, which corresponds to the beginning of the superelastic part on the stress-strain curves of the studied Ti-Nb-based SMA. Consequently, *in situ* study of the stress-induced martensitic transformation in these alloys becomes feasible.

The following three-mode methodology of the *in situ* X-ray transformation analysis during temperature scanning in the -150 to +100^{o}C temperature range is validated: a) strain-free, b) constant-strain after loading in the austenitic state (RT), and c) constant-strain after loading in the martensitic state (-150^{o}C). Preliminary results obtained for the biomedical Ti-Nb-Zr SMA are presented and analysed. These results received public approval at the European Symposium on Martensitic Transformations, ESOMAT 2012 and were published in Materials Science Forum in 2013, Vol. 738-739, pp. 87-91.

IN-SITU X-RAY STUDY OF PHASE TRANSFORMATIONS IN Ti-Nb-BASED SMA UNDER VARIABLE STRESS-TEMPERATURE CONDITIONS: PRELIMINARY RESULTS

Dubinskiy Sergey [1,2], Brailovski Vladimir[1], Prokoshkin Sergey[2], Inaekyan Karine[1]

[1]Ecole de technologie supérieure, 1100, Notre-Dame Str. West, Montreal (Quebec), H3C 1K3, Canada

[2]National University of Science and Technology "MISIS", 4, Leninskiy prosp., Moscow 119049, Russian Federation

Abstract

The technique and preliminary results of *in situ* X-ray diffraction analysis of the martensitic transformation in the newly developed Ti-Nb-Zr SMA for biomedical application are presented. To perform the *in situ* analysis, an original tensile stage, powered by a Ti-Ni SMA actuator and fit within the "TTK450" thermal chamber of a "PANalytical X'Pert Pro" diffractometer is designed, manufactured and validated. The tensile stage working principle and analysis methodology are described in detail. Preliminary results obtained during in-situ X-ray analysis of the phase transformations in Ti-Nb-Zr SMA are also presented.

Keywords: titanium alloys, shape memory alloys, X-ray diffraction analysis, in-situ tensile stage.

Introduction

High elastic modulus and linear stress-strain behaviour with limited reversible strain of conventional metallic implant materials' compromise their biomechanical compatibility. Ti-Ni shape memory alloys (SMA) are better suited for this role because of their superelasticity which closely mimicks bone behaviour [1,2], but their application in medicine is hindered by the presence of toxic nickel [3]. A new generation of multicomponent Ni-free Ti-Nb-based metastable β-titanium alloys containing only non-toxic elements (Ta, Zr, Mo, O) [4,5] is emerging, offering the most promising candidates for the role of metallic implant materials.

Shape memory and superelasticity observed in these alloys are due to thermoelastic β↔α" martensitic transformation. Since Ti-Nb-based SMA are multiphase alloys, they generally contain, in addition to body centered cubic β "austenite" and orthorhombic α"-martensite, hexagonal α, α'-martensite and ω-phase. That significantly complicates their microstructural analysis and therefore the understanding of the features of low-temperature phase transformations in these materials.

This paper is focused on *in situ* X-ray diffraction study of phase transformations in Ti-Nb-Zr SMA under variable stress-strain-temperature conditions. This work addresses the design, manufacture and validation of an original tensile stage lodged within the "TTK450" thermal chamber of a "PANalytical X'Pert PRO" diffractometer and powered by Ti-Ni SMA actuator. Preliminary results obtained during *in situ* X-ray diffraction analysis of the structure and phase changes under stress in Ti-Nb-Zr SMA are also presented.

Experimental

Ti-Nb-Zr alloy samples are used in this work. A Ti-21.8Nb-6Zr (at.%) cylindrical ingot (50 mm diameter, 660 mm long) was produced by induction skull melting ("Flowserve Corp.", USA) and subjected to hot isostatic pressing (900^{o}C, 100 MPa, 2 h). For X-ray analysis, 1.2×0.8×100 mm plates were EDM-cut from the ingot, cold-rolled (logarithmic thickness reduction e=0.37) and annealed (600^{o}C, 0.5 h). These processing conditions are based on the results obtained in [6].

After thermomechanical processing, the plates were cut into 30 mm-long samples and mechanically grinded, polished and chemically etched to 0.1 mm thickness.

The tensile stage mechanism shown in Figure A.1 is especially designed for use with SMA actuators. As a consequence, it can be integrated in a "TTK450" thermal chamber. The SMA actuator makes it possible to use the stage in the -196...+150^{o}C temperature range. The maximum force which can be applied to the sample is 250 N, maximum elongation is 2 mm,

the minimum sample working length is 16.5 mm. and the recommended exposed sample area for analysis is 3.5mm x 1.5mm.

Figure A.1 illustrates the tensile stage mechanism. The main frame (1) provides rigidity to the stage and holds the pivot axes (2) of the rotating levers (3) transmitting the tensile force from the SMA actuator (4) to the specimen (5). The actuator-to-specimen levers length ratio can be adjusted from 1:1.5 to 1:2.

To avoid X-ray defocusing during scanning, the guiding shafts (6) maintain the specimen (5) in a constant vertical position. To electrically isolate the SMA actuator (4), polymer sleeves are used as insulators between the actuator tilting grip system (7) and the levers (3). The identical tilting grip system (7) is used for specimen (5) fixation. The glass plate (8) is used to avoid X-ray diffraction from the main frame (1). All the parts except the insulator sleeves are made of stainless steel.

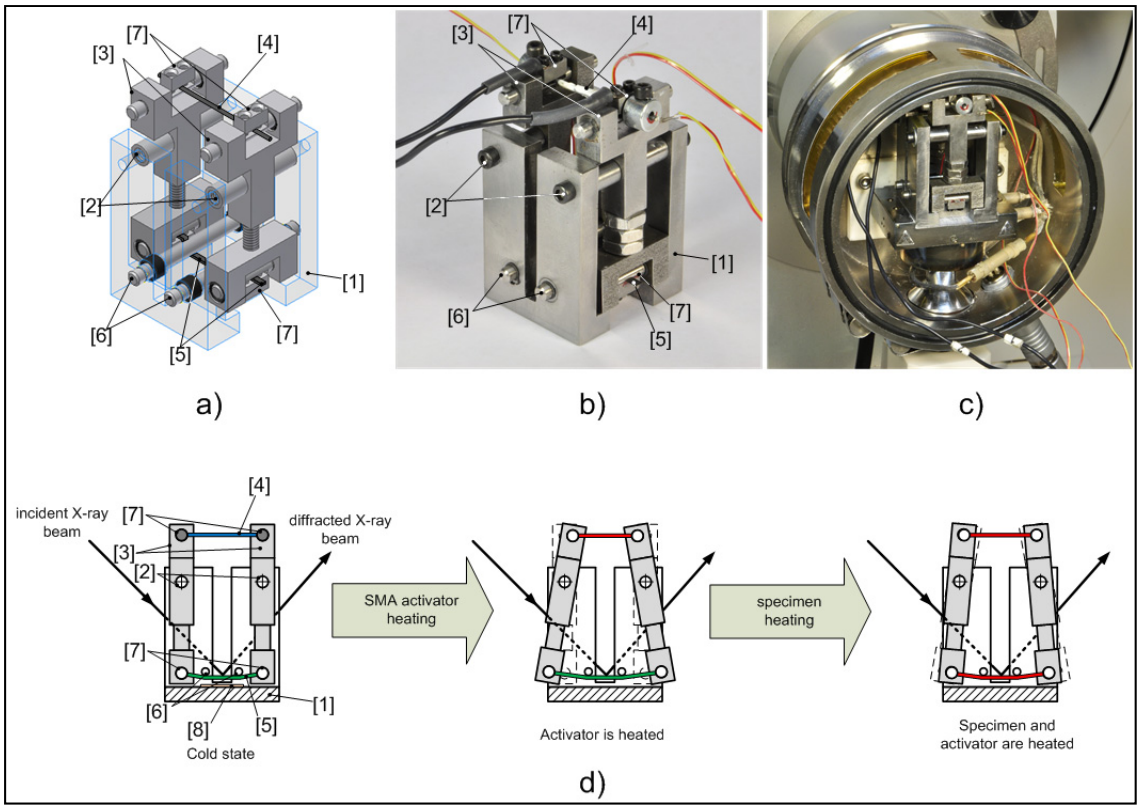

Figure A.1 Tensile stage mechanism: a) 3D prototype computer model; b) photo of the tensile stage mechanism; c) tensile stage inside a TTK450 thermal chamber; d) operation principle

The main frame (1) is directly mounted on the thermo-control plate of the thermal chamber, and a thin layer of silicone grease is applied to both connected surfaces to improve heat transfer from the control plate of the thermal chamber to the specimen; boron nitride powder is used as a thermoconductive lubricant for all the rubbing elements.

The operation principle is illustrated in Figure A.1d. Initially the actuator (4) and the specimen (5) are connected in their "cold" state. When the actuator is heated, while the specimen is not, the first shortens and stretches the second, and the whole system reaches its second equilibrium position. When the specimen is heated in its turn, it also starts to generate recovery stresses, opposing the actuator, and the third equilibrium position is reached.

The SMA actuator represents a 1mm diameter Ti-Ni SMA wire (“SAES GETTERS”) with an active length of 16.3 mm. Before installation, the Ti-Ni wire was subjected to thermomechanical cycling under constant stress to induce and stabilize a two-way shape memory effect in the material. This wire actuator generates either recovery stresses up to σ_r^{max} = 530 MPa or recovery strains up to ε_r^{max}= 3%. These recovery stress-strain characteristics of the Ti-Ni active element (4) correspond to the ~415N – 0.5 mm force-stroke characteristics of the SMA actuator. Considering a 1 : 2 actuator-specimen levers length ratio, 208N – 1 mm force - stroke loading can be applied to the sample.

The actuator is heated by direct Joule heating and its temperature is measured by a K-type thermocouple (“TT-K-36-SLE(ROHS), Omega”), insulated and fixed to the actuator. For thermocouple reading, a USB data acquisition module (“NI USB-6211”, “Nat’l Instr.”) is used. Lab-View software with a PID controller (“LabView 9.0”, “Nat’l Instr.”) and a programmable power supply (“SPS100-33-KOU2”, “American Reliance”) allow for control of the SMA actuator temperature.

The 150^oC…$+100^oC$ temperature range used in our *in situ* X-ray structure analysis encompasses the major structural changes related to the β↔α” martensitic transformations observed in the studied Ti-21.8Nb-6Zr (at.%) alloy [6].The TTK thermal chamber with the miniature tensile stage developed for this study is installed in the “PANalytical X’Pert Pro” diffractometer with $Cu_{K\alpha}$ monochromatized radiation. Three X-ray analysis sequences are schematically represented in Figure A.2. The first (reference) sequence (strain-free, SF) of temperature scanning (Figure A.2a), implies cooling of the non-stressed sample down to -150^oC (1-2) followed by heating it up to 100^oC (2-3). The second and the third sequences both imply temperature scanning under a constant strain. When the specimen is loaded in its austenitic state (room temperature), this sequence is called the “constant-strain-from-austenite, CS(A)” temperature scanning (Figure A.2b). When the specimen is loaded in its martensitic state, this sequence is called the “constant-strain-from-martensite, CS(M)” temperature scanning (Figure A.2c). The CS(A) and CS(M) X-ray study sequences allow

analysis of both the temperature- and the strain-induced direct and reverse martensitic transformations and reversible martensite reorientation.

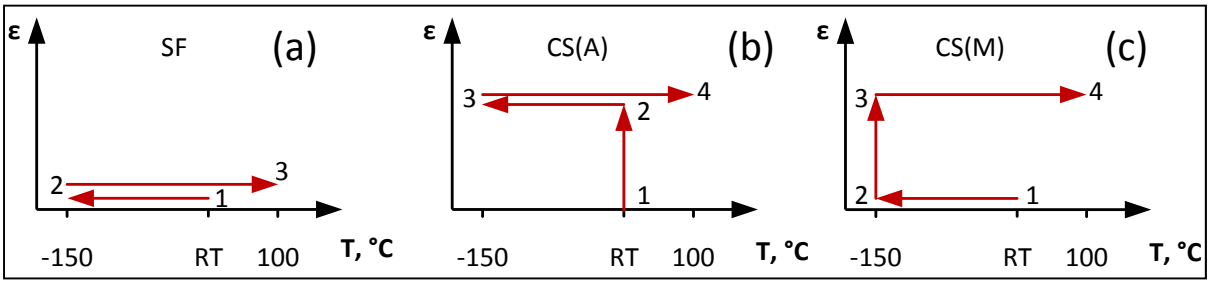

Figure A.2 *In situ* X-ray study sequences: a) strain-free (SF) temperature scanning; constant-strain temperature scanning with loading in b) austenitic CS(A) and c) martensitic CS(M) states.

Results and Discussion

This work is limited to the presentation of some preliminary results obtained using SF and CS(M) schedules. Figure A.3a shows X-ray diffractograms corresponding to RT, 110°C and +100°C temperatures (SF) in a consecutive order. It can be observed that β-austenite lines {110}, {200} {211}, {220} and {310} are present at all the X-ray scanning temperatures, whereas α"-martensite lines (020), (111), (012), (102), (200), (130) and (131) appear when the specimen is cooled down and disappear when it is heated again, being accompanied with the X-ray lines of "athermal" ω phase appearance and disappearance. From these diffractograms, it is also possible to measure thermal expansion/contraction strains $(\Delta d/d)_{hkl}$.

In the insert to Figure A.3a, a relative variation of the interplanar distance corresponding to the 110_β peak $(\Delta d/d)_{110}$ is plotted as a function of the temperature: strain-free cooling from RT to -150°C (path 1→2, one scan at RT) and strain-free heating from -150 to +100°C (path 2→3, 8 scans). For the SF sequence, $(\Delta d/d)_{110}$ values are equal to the thermal contraction/expansion strain, $(\varepsilon_{\Delta T})_{110}$; and they are calculated from the angular shifts of the 110_β peak position.

On heating (path 2→3), a net deviation from the linear behaviour can be observed, starting at about -75°C, thus pointing to the onset of α"→β and ω→β phase transformations.

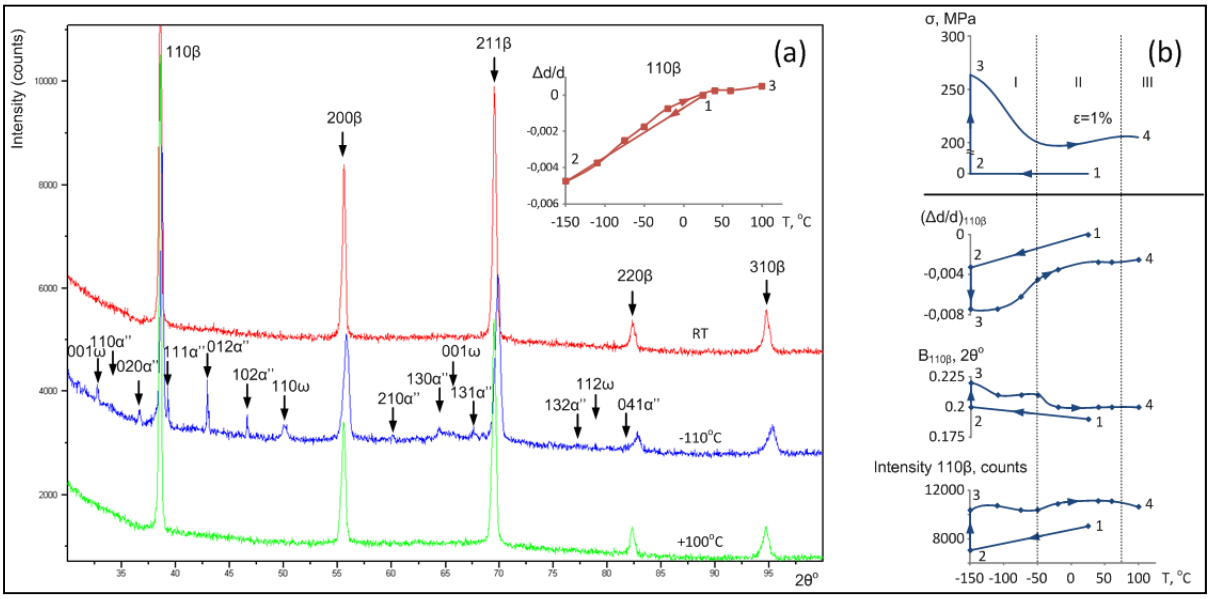

Figure A.3 Ti-21.8Nb-6Zr (at.%) alloy: a) SF sequence: X-ray diffraction profiles for selected temperatures and relative variation of the 110_β interplanar distance as a function of temperature (insert); b) CS(M) sequence: 110_β X-ray line parameters' variation as functions of the temperature

In Figure A.3b, the 110_β line parameters measured during the CS(M) sequence are plotted as functions of the temperature. These parameters comprise: the relative variation of the interplanar distance $(\Delta d/d)_{110}$ obtained from the angular shift of the peak position, the peak mid-height width (B_{110}) and the intensity (peak height) (I_{110}). For the sake of comparison, a stress-temperature diagram obtained during previous constant-strain temperature scanning experiments is also plotted in Figure A.3b [6]. This last test was realized under 1% constant strain using exactly the same CS(M) sequence.

In Figure A.3b, SC(M) sequence, path 1-2 of all the plots corresponds to cooling from RT to -150°C, path 2-3 to stretching at -150°C, and path 3-4 to heating under a constant strain. Three temperature ranges can be distinguished in the heating path 3-4: the first range, -150°C…-50°C, corresponding to stress relaxation caused by thermal expansion, the second

interval, -50°C …+75°C, where the recovery stresses generated in course of α"→β transformation overcome the stress relaxation caused by thermal expansion, and the third range, >75°C, where the stress relaxation due to thermal expansion exceeds the stress generated due to constrained reverse martensitic transformation.

Considering that the X-ray strain analysis is based on the measurement of variations of interplanar distances in the direction perpendicular to the specimen surface (transverse direction), and that these variations contain two components: the first related to thermal contraction/expansion and the second related to the applied external loads, the total transverse strain measured by X-ray diffraction can be written as $\Sigma\varepsilon_{\perp} = \varepsilon_{\Delta T} + \varepsilon_{\perp}$, where $\varepsilon_{\Delta T}$ is the thermal expansion strain known from the previous SF mode measurements, and $\varepsilon_{\perp}$ is the transverse strain caused by external load, all three corresponding to a given X-ray scanning temperature. From the transverse strain caused by external load, it is possible to evaluate a longitudinal tensile strain ε applied to the sample. Figure A.4 illustrates the conversion from the measured transverse strain (Figure A.4a) to the longitudinal tensile strain applied to the specimen (Figure A.4c). This conversion is made by subtracting the thermal expansion strain (Figure A.4b) and dividing the result obtained by the Poisson's ratio. It can be seen from Figure A.4c that the real strain applied to the specimen when heated from -150 to +100°C is not constant. It varies between 0.82 to 1.2%, with an average value of 1%. These variations are caused by a non-uniform temperature distribution in the tensile stage and its limited rigidity.

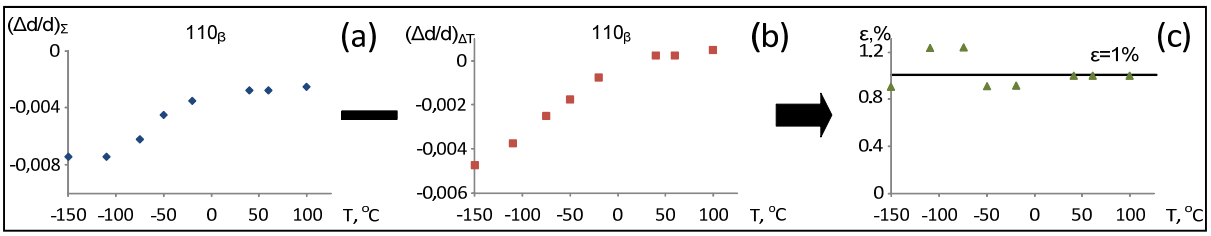

Figure A.4 a) Total transverse strain (CS(M) sequence), b) thermal expansion strain, (SF sequence), and c) longitudinal tensile strain applied to the specimen (all the measurements are made on heating)

Summary

An original tensile stage fitted within the TTK450 thermal chamber of a “PANalytical X’Pert PRO” diffractometer and powered by a Ti-Ni SMA actuator is designed, manufactured and successfully validated. Three sequences of *in situ* X-ray martensitic transformation analysis are realized: strain-free temperature scanning, constant-strain temperature scanning with loading in the austenitic state and constant-strain temperature scanning with loading in the martensitic state. Preliminary results obtained for biomedical Ti-Nb-Zr SMA by means of in-situ X-ray analysis under variable force-temperature conditions are presented and analysed.

Acknowledgements

The authors are grateful to the Natural Science Engineering Research Council of Canada and the Ministry of Education and Science of the Russian Federation for the financial support.

References

[1] J. Ryhänen, Biocompatibility Evaluation of Nickel-Titanium Shape Memory Alloy, Academic Dissertation, University of Oulu, 1999.

[2] T. Yoneyama, S. Miyazaki, Shape Memory Alloys for Biomedical Applications, Woodhead Publishing Ltd, England (2010).

[3] K. Takamura, K. Hayashi, N. Ishinishi, T. Yamada, Y. Sugioka, Evaluation of carcinogenicity and chronic toxicity associated with orthopedic implants in mice, J. Biomed. Mater.Res. 28 (1980) 583-589.

[4] S. Miyazaki, H.Y. Kim, H. Hosoda, Development and characterization of Ni-Free Ti-based shape memory and superelastic alloys, Mater. Sci. Eng. A. 438-440 (2006) 18-24.

[5] E.W. Collings, Titanium alloys, A.S.f. Metals, 1984.

[6] V. Brailovski, S. Prokoshkin, K. Inaekyan, S. Dubinskiy, M. Gauthier, Mechanical properties of thermomechanically processed metastable beta Ti-Nb-Zr alloys for biomedical applications, Mater. Sci. Forum 706-709 (2012) 455-460.

LIST OF BIBLIOGRAPHICAL REFERENCES

[1] Davis, J.R., Handbook of materials for medical devices. 2004: ASM International. 350.

[2] Temenoff, J.S. and Mikos A.G., Biomaterials: The intersection of biology and materials science. 2008, New Jersey: Pearson Prentice Hall. 502.

[3] Donachie, M., Biomaterials, Metals Handbook Desk Edition. 2nd ed. 1998. ASM International. P. 702-709.

[4] Niinomi, M., Recent titanium R&D for biomedical applications in Japan. JOM, 1999. 51(6): p. 32-34.

[5] Ranter, B.D. et al., Biomaterials Science: An Introduction to Materials in Medicine 2en ed. 2004, San Diego: Elsevier Academic Press. 863.

[6] Spine, Z., http://www.endius.com/z/ctl/op/global/action/l/id/9193/template/pc/navid/9640. Trabecular Metal Technology 23/2/2009.

[7] Hastings, G.W., Ducheyne, P., Natural and living biomaterials. 1984, Boca Raton, Florida: CRC Press, Inc. 167.

[8] Cowin, C.S., Bone mechanics. 2nd ed. 2001, Boca Raton, Florida: CRC Press. 980.

[9] Favus, M.J. (T.A.S.F.B.A.M.), Primer on the metabolic bone diseases and disorders of mineral metabolism. 1999, Philadelphia: Lippincott Williams & Wilkins. 263.

[10] Sevilla, P., Aparicio, C., Planell, J.A., Gil, F.J., Comparison of the mechanical properties between tantalum and nickel-titanium foams implant materials for bone ingrowth applications. Journal of Alloys and Compounds, 2007. 439: p. 67-73.

[11] Fung, Y.C., Biomechanics. Mechanical properties of living tissue. 2nd ed. 1993: Springer-Verlag. 592.

[12] Park, J. B., Lakes, R.S., Biomaterials: an introduction. 3rd ed. 2007, N.Y.: Springer. 564.

[13] Agrawal, C.M., Reconstructing the human body using biomaterials. JOM, 1998. 50(Compendex): p. 31-35.

[14] Levine B.R., Sporer S., Poggie R.A., Della Valle C.J., Jacobs J.J., Experimental and clinical performance of porous tantalum in orthopedic surgery. Biomaterials, 2006. 27: p. 4671-4681.

[15] ASM, Carpenter CP Titanium Grade 4: Unalloyed titanium (Ti128). 2002, Alloy Digest Material Data Sheet.

[16] Long, M., Rack, H. J., Titanium alloys in total joint replacement - a materials science perspective. Biomaterials, 1998. 19(18): p. 1621-1639.

[17] Davis, J.R., Metals Handbook: desk edition. 2nd ed. 1998, ASM International. 1525.

[18] Murray, J.L., Ti (Titanium) Binary Alloy Phase Diagrams. 1987, ASM Handbooks Online.

[19] Brailovski, V., Prokoshkin, S., Terriault, P., Trochu, F., ed., Shape memory alloys: fundamentals, modeling and application. 1st ed. 2003, Montreal: École de Technologie Supérieure. 844.

[20] Melton, K.N. and Mercier, O., The effect of opposing stress on shape memory and martensitic reversion. Scripta Metallurgica, 1978, 12(1): p. 5-9.

[21] Brailovski, V. et al., Functional properties of nanocrystalline, submicrocrystalline and polygonized Ti-Ni alloys processed by cold rolling and post-deformation annealing. Journal of Alloys and Compounds, 2011. 509(5): p. 2066-2075.

[22] Moore, T.L.A., Gibson, L.J., Microdamage accumulation in bovine trabecular bone in uniaxial compression. Transactions of the ASME. Journal of Biomechanical Engineering, 2002. 124: p. 63-71.

[23] Lawes, F., Wallbaum, H.J. Naturwissenschaften, 1939. 27(3): p. 674-681.

[24] Otsuka, K., Ren, X., Physical metallurgy of Ti-Ni-based shape memory alloys. Progress in Materials Science, 2005. 50(5): p. 511-678.

[25] Philip, T.V. and Beck, P.A., CsCl-type ordered structures in binary alloys of transition elements. Journal of Metals, 1957. 9(10, Sec 2): p. 1269-1271.

[26] Tadaki, T., Wayman, C.M., Electron microscopy studies of martensitic transformations in Ti50Ni50-xCux alloys. II. Morphology and crystal structure of martensites. Metallography, 1982. 15: p. 247-58.

[27] Prokoshkin, S.D., Korotitskiy, A.V., Brailovski, V., Turenne, S., Khmelevskaya, I.Yu., Trubitsyna, I.B., On the lattice parameters of phases in binary Ti-Ni shape memory alloys. Acta Materialia, 2004. 52: p. 4479-4492.

[28] Kim, J.I. et al., Shape memory characteristics of Ti-22Nb-(2-8)Zr(at.%) biomedical alloys. Materials Science and Engineering A, 2005. 403: p. 334-339.

[29] Kim, H.Y., Hashimoto, S., Kim, J.I., Inamura, T., Hosoda, H., Miyazaki, S., Effect of Ta addition on shape memory behavior of Ti-22Nb alloy. Materials Science and Engineering 2006. A 417: p. 120-128.

[30] Nag, S., Banerjee, R., H.L., Fraser, Intra-granular alpha precipitation in Ti-Nb-Zr-Ta biomedical alloys. Journal of Materials Science, 2009. 44: p. 808-815.

[31] Banerjee, R. et al., Strengthening mechanisms in Ti-Nb-Zr-Ta and Ti-Mo-Zr-Fe orthopaedic alloys. Biomaterials, 2004. 25: p. 3413-19.

[32] Li, S.J. et al., Ultrafine-grained β-type titanium alloy with nonlinear elasticity and high ductility. Applied Physics Letters, 2008. 92.

[33] Ping, D.H., Mitarai, Y., Yin, F.X., Microstructure and shape memory behavior of a Ti-30Nb-3Pd alloy. Scripta Materialia, 2005. 52: p. 1287-1291.

[34] Kim, H.Y., Kim, J.I., Inamura, T., Hosoda, H., Miyazaki, S., Effect of thermo-mechanical treatment on mechanical properties and shape memory behavior of Ti-(26-28)at.% Nb alloys. Materials Science and Engineering, 2006. A 438-440: p. 839-843.

[35] Miyazaki, S., Kim, H.Y., Hosoda, H., Development and characterization of Ni-free Ti-base shape memory and superelastic alloys. Materials Science and Engineering, 2006. A 438-440: p. 18-24.

[36] Gasik, M.M., Yu, H., Phase equilibria and thermal behaviour of biomedical Ti-Nb-Zr alloy. In 17th Plansee Seminar, International Conference on High Performance P/M Materials. 2009. The Institute of Materials, Minerals and Mining, Reutte, Austria.

[37] Kobayashi, S. et al., Phase decomposition in a Ti-13Nb-13Zr alloy during aging at 600C. Materials Transactions, 2002. 43: p. 2956-63.

[38] Geetha, M. et al., Effect of thermomechanical processing on evolution of various phases in Ti-Nb-Zr alloys. Journal of Alloys and Compounds, 2004. 384: p. 131-44.

[39] Kim, H.Y., Ikehara, Y., Kim, J.I., Hosoda, H., Miyazaki, S., Martensitic transformation, shape memory effect and superelasticity of Ti-Nb binary alloys. Acta Materialia, 2006. 54: p. 2419-2429.

[40] Baker, C., The shape-memory effect in a Titanium-35 wt.% Niobium. alloy. Metal Science Journal, 1971. 5: p. 92-100.

[41] Da Silva, E.P., Calorimetric analysis of the two-way memory effect in a NiTi alloy – experiments and calculations. Scripta Materialia, 1999. 40(10): p. 1123-1129.

[42] Khalil Allafi, J., Ren, X., Eggeler, G., The mechanism of multistage martensitic transformations in aged Ni-rich NiTi shape memory alloys. Acta Materialia, 2002. 50: p. 793-803.

[43] Morinaga, M., Murata, Y., Yukawa, H., Molecular orbital approach to alloy design. In Applied Computational Materials Modeling: Theory, Simulation and Experiment, G. Bozzolo, Noebe, R.D., Abel, P.B. (eds). 2007, Springer, p. 255-306.

[44] Abdel-Hady, M., Hinoshita, K., Morinaga, M., General approach to phase stability and elastic properties of β-type Ti-alloys using electronic parameters. Scripta Materialia, 2006. 55: p. 477-480.

[45] Abdel-Hady, M. et al., Phase stability change with Zr content in β-type Ti-Nb alloys. Scripta Materialia, 2007. 57: p. 1000-3.

[46] Petrzhik, M.I., Fedotov, S.G., Thermal stability and dynamics of martensite structure in Ti-(Ta, Nb) alloys. Proc. XVI Conf. on Applied Crystallography, Cieszyn.1995, World of Science Publishing, p.273-276.

[47] Kim, H.Y.,Sasaki, T.,Okutsu, K. et al., Texture and shape memory behavior of Ti-22Nb-6Ta alloy. Acta Materialia, 2006. 54: p. 423-433.

[48] Kim, H.Y., Hashimoto, S., Kim, J.I. et al., Effect of Ta addition on shape memory behavior of Ti–22Nb alloy. Materials Science and Engineering A. 2006. 417: p. 120-128.

[49] Khalil-Allafi, J., Dlouhy, A., Eggeler, G., Ni_4Ti_3-precipitation during aging of NiTi shape memory alloys and its influence on martensitic phase transformations. Acta Materialia, 2002. 50: p. 4255-4274.

[50] Lotkov, A.I. et al., Influence of low-temperature annealing on a starting temperature of martensitic transformation in titanium nickelide. Fizika Metallov i Metallovedenie, 1982. 54(6): p. 1202-1204 (in Russian).

[51] Lotkov, A.I., Grishkov, V.N., Influence of austenite structure state on martensitic transformations in $Ti_{49}Ni_{51}$. Low-temperature aging. Fizika Metallov i Metallovedenie, 1990. 7: p. 88-94 (in Russian).

[52] Nishida, M., Honma, T., Effect of heat treatment on the all-round shape memory effect in Ti-51at.%Ni. Scripta Metallurgica, 1984. 18: p. 1299-1302.

[53] Oleynikova, S.V., Prokoshkin, S.D., Kaputkina, L.M., Khmelevskaya, I.Y., Influence of aging on mechanical behaviour of Ti-50.7at.%Ni alloy. Technology of Light Alloys, 1990. 4: p. 28-34 (in Russian).

[54] Wu, S.K., Lin, H. C., The effect of precipitation hardening on the Ms temperature in a Ti49.2Ni50.8 alloy. Scripta Metallurgica et Materialia, 1991. 25: p. 1529-32.

[55] Oleynikova, S.V., Khmelevskaya, I.Y., Prokoshkin, S.D., Kaputkina, L.M., Effect of aging on martensitic transformation in Ti-50.7at.%Ni alloy. In ICOMAT-92. 1992. Monterey Institute of Advanced Studies, Carmel, USA.

[56] Khmelevskaya, I.Y., Prokoshkin, S.D., Shipsha, V.G., Bazhenov, I. P., Ryklina, E.P., Thermomechanical strengthening of titanium nickelide and structure changes upon generation and forced isothermal relaxation of reactive stress. Physics of Metals and Metallography, 2002. 93(2): p. 189-195.

[57] Hao, Y.L. et al., Elastic deformation behaviour of Ti-24Nb-4Zr-7.9Sn for biomedical applications. Acta Biomaterialia, 2007. 3: p. 277-86.

[58] Lagunova, M.I., Dilatometric and structure changes during realization of recoverable and non-recoverable shape memory effects in thermally and thermomechanically treated Ti-Ni based alloys. 1997, Moscow. 136 (in Russian).

[59] Perkins, J., Martensitic transformation cycling and the phenomenon of two-way shape memory training. In Mat. Res. Soc. Symp. Proc. 1984. p. 669-674.

[60] Perkins, J., Sponholz, R.O., Stress-induced martensitic transformation cycling and two-way shape memory training in Cu-Zn-Al alloys. Met. Trans., 1984. 15A(2): p. 313-321.

[61] Zhang, Q.A. et al., Effects of training temperature on the two way memory effect in a Cu-Zn-Al alloy. Scripta Metallurgica et Materialia, 1994. 31: p. 511-514.

[62] Contardo, L., Guenin, G., Effect of deformation on phase transformations and modulus of elongation in Titanium Nickelide-based alloy. Acta Met. et Mater., 1990. 38(7): p. 1267-1272.

[63] Miyazaki, S., Igo, Y., Otsuka, K., Effect of thermal cycling on the transformation temperatures of Ti-Ni alloys. Acta Metallurgica, 1986. 34: p. 2045-51.

[64] Hao, Y., Yonglin, K., Zhengzhi, Z. et al., Microstructural characteristics and texture of hot strip low carbon steel produced by flexible thin slab rolling with warm rolling technology. Mater. Charact., 2006. 56: p. 158-164.

[65] Homma, D., Uemura, S., Nakazawa, F., Functional anisotropic shape memory alloy fiber and differential servo actuator. SMST-2007 - Proceedings of the International Conference on Shape Memory and Superelastic Technologies, 2008. p. 463-472.

[66] Shu, Y.C., Bhattacharya, K., The influence of texture on the shape-memory effect in polycrystals. Acta Mater., 1998. 46: p. 5457-5473.

[67] Bernshtein, M.L., Hot strain diagrams, structure and properties of steels. 1989, Moscow: Metallurgiya Publ. 544 (in Russian).

[68] Bondareva, S.A., Creation of substructure by thermomechanical treatment for regulation of transformation parameters and properties of shape memory alloys. 1992, Moscow Steel and Alloys Institute: Moscow. 142 (in Russian).

[69] Prokoshkin, S.D., Kaputkina, L.M., Bondareva, S.A., Structure of hot-deformed austenite and properties of Ti-Ni-Fe alloy after HTMT. Fizika Metallov i Metallovedenie, 1991. 3: p. 144-149 (in Russian).

[70] Luo, H., Shan, F., Huo, Y., Wang, Y., Effect of precipitates on phase transformation behaviour of Ti-49at.%Ni film. Thin Solid Films, 1999. 339: p. 305-308.

[71] Zeldovich, V.I., Sobyanina, G.A., Pushin, V.G., Bimodal size distribution of Ti_3Ni_4 particles and martensitic transformations in slowly cooled nickel-rich Ti-Ni alloys. Scripta Materialia, 1997. 37(1): p. 79-84.

[72] Lin, H.C. et al., Effects of cold rolling on the martensitic transformation of an equiatomic TiNi alloy. Acta Metallurgica et Materialia, 1991. 39(9): p. 2069-2080.

[73] Filip, P., Mazanec, K., Influence of work hardening and heat treatment on deformation behaviour of TiNi shape memory alloys. Scripta Metallurgica et Materialia, 1995. 32: p. 1375-80.

[74] Brailovski, V., Prokoshkin, S.D., Khmelevskaya, I. Yu., Inaekyan, K. E., Demers, V., Dobatkin, S.V., Tatyanin, E.V., Structure and properties of the Ti-50.0 at% Ni alloy after strain hardening and nanocrystallizing thermomechanical processing. Materials Transactions, 2006. 47(3): p. 795-804.

[75] Prokoshkin, S.D., Brailovski, V., Inaekyan, K.E. et al., Structure and properties of severely cold-rolled and annealed Ti-Ni shape memory alloys. Mater. Sci. Eng. A, 2008. 481-482: p. 114-118.

[76] Lobodyuk, V.A., Size effect upon martensitic transformations. The Physics of Metals and Metallography, 2005. 99(2): p. 143-153.

[77] Demers, V., Brailovski, V., Prokoshkin, S. et al., Functional properties of nanostructured Ti-50.0 at % Ni alloys. J. ASTM International, 3 (2006), online.